Mechanical behaviour of compacted earth with respect to relative humidity and clay content : experimental study and constitutive modelling

Longfei Xu

N°d'ordre NNT : 2018LYSET005

THESE de DOCTORAT DE L'UNIVERSITE DE LYON
opérée au sein de
École Nationale des Travaux Publics de l'Etat
LGCB-LTDS UMR 5513

Ecole Doctorale N° 162
MEGA (Mécanique, Energétique, Génie Civil, Acoustique)

Spécialité : Génie Civil

Soutenue publiquement le 04/07/2018, par :

Longfei XU

Mechanical behaviour of compacted earth with respect to relative humidity and clay content: experimental study and constitutive modelling

Devant le jury composé de :

Philippe COSENZA	Professeur (Université de Poitiers)	Président
Jean Michel PEREIRA	Professeur (ENPC)	Rapporteur
Philippe COSENZA	Professeur (Université de Poitiers)	Rapporteur
Mathilde MORVAN	Maître de Conférences (UCA)	Examinatrice
Annan ZHOU	Senior Lectuer (RMIT)	Examinateur
Henry Kwai Kwan WONG	Directeur de Recherche CNRS (ENTPE)	Directeur
Antonin FABBRI	Chargé de Recherche (ENTPE)	Co-directeur
Rafael ANGULO-JARAMILLO	Chargé de Recherche CNRS (ENTPE)	Invité

Acknowledgements

This thesis is the result of four years of work whereby I have been accompanied and supported by many people. I take this opportunity to extend my sincere gratitude and appreciation to all those who made this PhD thesis possible.

Foremost, I would like to express my sincere gratitude to my thesis supervisor, Prof. Kwai Kwan WONG, for accepting me into his research group. I acknowledge his guidance and encouragement through this four years study, and his constant confidence in my abilities. He is always willing to share his experience and expertise throughout my PhD study. He taught me how to be a researcher and I will always be grateful for this. His advice on both research as well as on my career have been invaluable.

I would also wish to express my deep gratitude to my co-supervisor Dr. Antonin FABBRI for extended discussions and valuable suggestions which have contributed greatly to the thesis. His immense knowledge and his logical way of thinking have been of great value for me.

Special thanks to Dr. Florian Champiré for his contribution to the experimental apparatus and his unconditional help during the experiments. I admire his affirmative professional attitude, and his efficient mindful approach to simplify complexities. I enjoyed our collaboration and the good time we had together.

I appreciate Prof. Philippe COSENZA and Prof. Jean-Michel PEREIRA for the time they allocated to read my manuscript and for their precious reviews and comments. Further thanks are due to other thesis defense committee members: Dr. Mathilde MORVAN and Dr. Annan ZHOU. Also thanks to Prof. Rafael ANGULO-JARAMILLO for his presence in my thesis defence.

I am also grateful to a number of colleagues and friends for their assistance during my research in LGCB of ENTPE. I appreciate Dr. Denis BRANQUE, Dr. Fionn McGregor, Dr. Ali MESBAH and Dr. Hoang Ngoc LAN, for their precious advice and assistance on the experiments. I also warmly thank the technical staff from ENTPE, Mr. Stephane COINTET, Mr. Joachim BLANC GONNET, Mr. Frédéric SALLET and Mme. Nadia Bekkouche, for their help in my thesis.

In addition, I would like to thank to Mme. Marie-Claire HERVE TOUZE for her warm reception and patient help in my living on behalf of ENTPE. I would like to express my

appreciation to Mr. Luc Delattre, Mme. Francette PIGNARD, and Mme. Sonia CENILLE for their assistance in administrative affair.

Then, I would like to say thank you to my Chinese friends here at Lyon who have made my life very enjoyable.

Finally, I dedicate this part to thank all my family for all their love and encouragement. A tough journey becomes easier when we travel together. At last, but not certainly least, I would like to give my most heartfelt thanks to my beloved wife Minghui ZHU and also my son Boang XU, for being my endless source of peace. To end, I am grateful again to my wife, for her unconditional support, her continual love and her encouragement that helped me along the difficult times. Her love is the greatest power in the world and has driven me to succeed in every goal I have dreamed of.

The present work has been supported by the French Research National Agency (ANR) through the‘‘Villes et Bâtiments Durables” program (Project Primaterre no. ANR-12-VBDU-0001). My living in FRANCE is supported by the China Scholarship Council (CSC) with a PhD Scholarship (FileNo.201406300070).

Abstract

Compacted earth is regarded as a granular mixture in which clay plays a role of binder but also exhibits an important interaction with water. During its service period, compacted earth can be subject to large changes in relative humidity. Those perpetual changes of environmental conditions induce continuous changes of water content of the earth that impact significantly its mechanical performances. The present work aims at studying the mechanical behavior of compacted earth with respect to relative humidity and clay content. It involves an extensive experimental study and a constitutive modelling.

For clarity, the presentation of experimental results will be divided into two parts. In the first part, four kinds of local earth are identified with variety of clay content. A comparison of compaction method was then conducted between a double static compaction and dynamic compaction. Similarly to Proctor test, a series of iso-energy cures can be sought out during static compaction. And all the optimum points approximately lie on a specific saturation degree line regardless of the compaction method and compaction energy. Three types of specific tests: suction test by filter paper method, shrinkage test and sorption-desorption test were carried out on those samples from aforementioned compaction, thereby providing a preliminary insight on the effect of clay content and moisture content: the results reveal that matric suction increases with increasing clay content and decreasing moisture content. For a given earth, when the logarithm of suction values are plotted against moisture content, the results lie approximately on a unique line for all compaction methods. Comparing between different soils, a higher clay content results in a higher hygroscopic ability to absorb and store moisture from the surrounding air.

In the second part, the impact of clay content and moisture contents on the shear behavior of compacted earth was investigated taking into account loading-unloading cycles. Fine sand of different proportions was added into a natural soil thereby obtaining three different soils with clay contents respectively of 35%, 26% and 17%. A series of triaxial tests were conducted on samples previously equilibrated at three different values of relative humidity (23%, 75% and 97%). The confinement conditions are 0, 100, and 600kPa respectively. The evolution of failure strength f_c, Young's modulus E and residual strain ε_{res} with clay content and RH was investigated, the last two parameters being measured during loading-unloading cycles. The first important observation is that the relative humidity at which samples were fabricated and conditioned has a strong impact on the mechanical characteristics of earthen material: an

increase of RH leads to a reduction of both the failure strength f_c and Young's modulus E, while the plastic strain is increased; the tendencies depend on the clay content of the samples. Secondly, with increasing stress level, a progressive degradation of Young's modulus as well as an increase of residual strain ε_{res} (after a loading-unloading cycle) appear. Thirdly, within the range of clay contents investigated, both the failure strength f_c and residual strain ε_{res} increase with increasing clay content at constant RH and confining pressure, the rate of this increase being a function of RH. Young's modulus E is relatively insensitive to changes in clay content, its variation being less than 20% for all cases. Finally, based on a particular definition of Bishop's effective stress involving a specific functional form $\chi(s)$, failure states of all samples were observed to lie approximately on a unique failure line crossing the origin in the (p'-q) plane regardless of matric suction and confining pressure.

Finally, based on the above experimental results, a new constitutive model was proposed aiming to simulate mechanical behaviour of compacted earth. This model accounts for stiffness degradation using the approach of continuum damage mechanics. The poroplastic behaviour is modelled based on the Bounding Surface Plasticity (BSP) theory and the concept of effective stress, while isotropic damage is modelled using a scalar variable. Plastic flow and damage evolution occur simulataneously in a coupled process, taking into account the impact of suction. The model was successfully validated against results of triaxial compression tests performed at different relative humidities and confining pressures. Despite the relatively small number of material parameters, this model can reproduce the essential features of earthen materials behaviour observed experimentally: suction-induced hardening and stiffening, post-peak softening, as well as the progressive transition from contractant to dilatant volumetric behaviour. Use of the BSP theory allows to reproduce a smooth stress-strain relation as experimentally observed, instead of an abrupt change upon plastic yielding predicted by classic elastoplastic models. Furthermore, the present model also furnishes a quantitative description on the degradation of elastic properties hitherto not accounted for, thanks to the additional scalar damage variable.

Keywords: Compacted earth, clay content, relative humidity, loading-unloading, failure criterion, bounding surface plasticity; damage; degradation

Table of contents

List of Figures

List of Tables

List of Symbols

Roman symbols

A_{CB}	index of clay activity
$c^{\mathcal{M}}$	molar concentration of the electrolyte
D	damage variable
e	void ratio
e_0	initial void ratio
E	young's modulus
f_c	failure strength
F	bounding surface
f	loading furface
f_D	damage criterion
H	plastic modulus
H_b	plastic modulus on bounding surface
H_δ	additive plastic modulus
h	Constant to calibrate the hardening modulus
I_P	plastic index
k_1	Constant to control suction effects on the hardening parameter
k_2	Constant to control suction effects on volumetric compressibility
k_3	Constant to describes the damage evolution
l	suction-hardening function
M_w	molar mass of water
$\mathrm{m_{dry}}$	dry sample mass
$\mathrm{m_{wet}}$	wet sample mass
$m_d^{105°C}$	dry mass in an oven at 105 °C
$m_d^{23°C}$	dry mass through a flow of dry air at 23 °C
$\mathrm{m_R}$	retained friction mass
$\mathrm{m_P}$	passed fraction mass
$\boldsymbol{m}$	unit vector of plastic potential
m	Constant to define plastic potential
M	Critical state line in q-p' plane

$\mathbf{n}$	unit vector for the LS
$\overline{\mathbf{n}}$	unit vector for the BS
n	Constant specify the shape of bouning surface
p_π	preconsolidation pressure
p	mean stress
p'	mean effective stress on loading surface
$\bar{p}'$	mean effective stress on bounding surface
$\bar{q}$	deviatoric stress on bounding surface
q	deviatoric stress on loading surface
R	universal gas constant
r	Space ratio
s	total suction
s_m	matric suction
s_o	osmotic suction
S_r	degree of saturation
s_e	air-entry suction
u_a	pore air pressure
u_w	pore water pressure
V_V	volume of pore
V_w	volume of pore water
V_s	volume of solid
V_B	blue value of the soil
W_L	liquid limit
W_P	plastic limit
w_{int}	initial water contents
w_{DVS}	water contents in DVS
$w_{DVS}^{Corrected}$	water contents in DVS after correction
Y_D	damage force

Greek symbols

α	Constant to define effective stress parameter
β	scale factor between the BS and the LS

$\mathbb{C}^e$	elastic compliance matrix
$\mathbb{C}^{epD}$	elastoplastic compliance matrix accounting for damage
ε_i	principle strain (i=1,2,3)
ε_i^+	tensile part of the principal strain
$\boldsymbol{\varepsilon}$	Total strain
$\boldsymbol{\varepsilon^e}$	elastic strain
$\boldsymbol{\varepsilon^p}$	plastic strain
ε_v	volumetric strain
ε_q	deviatoric strain
ε_v^e	elastic volumetric strain
ε_q^e	elastic deviatoric strain
ε_v^p	plastic volumetric strain
ε_q^p	plastic deviatoric strain
ε_{res}	residual strain
$\Delta\varepsilon_{xx}^{cycle}$	differences of the axial strain between the maximal and minimal
η	stress ratio
θ	contact angle between the water and the boundary
κ	Slope of unloading line in the e -lnp' space
λ	plastic multiplier
λ_0	Volumetric compressibility constant
ν	Poisson's ratio
ϑ	moisture ratio
ρ_w	bulk density of water
ρ_d	dry density
ρ_s	soil grain density
σ_s	tensile force per unit length of interface
σ_i	principle stress (i=1,2,3)
σ_0	reference stress for dimensionless
$\boldsymbol{\sigma'}$	current stress point
$\overline{\boldsymbol{\sigma}}'$	image stress point on BS
$\Delta\sigma_{xx}^{cycle}$	differences of the axial stress between the maximal and minimal
φ_{wet}	particles percentage by wet sieving method

φ_{sed}	percentage of fine particles
χ	effective stress parameter
Ψ	total water potential
Ψ_g	gravitational potential
Ψ_p	gas pressure potential
Ψ_m	matric potential
Ψ_o	osmotic potential

Operators

δ_{ij}	Kronecker delta type function
$\widetilde{\nabla}$	pseudo-gradient operator
$\|.\|$	classic Euclidean norm of a vector
$\frac{\partial(.)}{\partial x}$	partial derivative with respect to a variable *x*
$d(.)$	increment symbol

Chapter 1
Introduction

1.1 Earth building materials

An earth building contains a significant part of unfired soil in their structure and/or building fabric. Earthen buildings can be constructed using several technics, e.g. rammed earth or compressed earth block (Hall et al. 2012). Earth constructions have a long history in the process of human civilization. According to the archaeological excavations, the first use of earth as building material dates back to the Neolithic period in approximately 10 000 BC from the eastern Mediterranean and Mesopotamia (Schroeder 2012). Earth material then became more and more popular in buildings considering its excellent performance in terms of structural stability, durability and environmental comfort. It is also quite adaptable, being used for footings, floors, walls and roofs utilising many techniques. Nowadays, one third of the world population lives in earthen houses and this number reaches more than one half in developing countries (Minke 2009). A great number of earth constructions, from rural habitats to impressive military citadels, can be found all over the world (shown in Figure 1.1), e.g. in Europe (France, Spain, Portugal and Italy etc.), the Africa region (Morocco, Algeria), South America (Mexico, Peru, Brazil) and the Asia area (China and Iran).

(a) Wattle and daub constructions, Lyon, France

(b) Rammed earth house Rhone-Alpes, France

(c) Roofs with plaster decorated acroterions, Libya

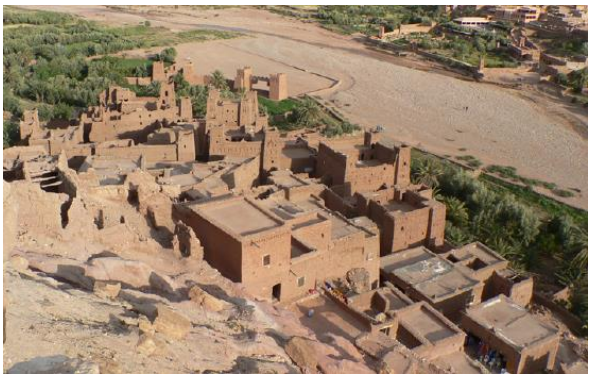

(d) Ksar of Ait-Ben-Haddou, Morocco

(e) Fujian Tulou, China

(f) Bam, Iran

(g) Pyramid of the Sun, Mexico

Figure 1.1 Earthen constructions around the world

There are a great varieties of earth building constructions: the earth has been providing various soil compositions at different places and the construction techniques have been evolving for hundreds of years. Each technique differs from the composition of the soil used, the compaction method, the initial moisture in the material and the drying process (Soudani 2017). In addition, earth buildings are related to human ecology and include contemporary as well as historical and vernacular examples drawn from many cultures and periods (Niroumand et al. 2013).

The techniques principally used are described in Figure 1.2, adapted from the classification proposed by Hamard (2018). Herein, a special cave-dwellings dug in original earth (mainly distributed in north-west of China and called “Yaodong” in chinese) is supplemented in this classification.

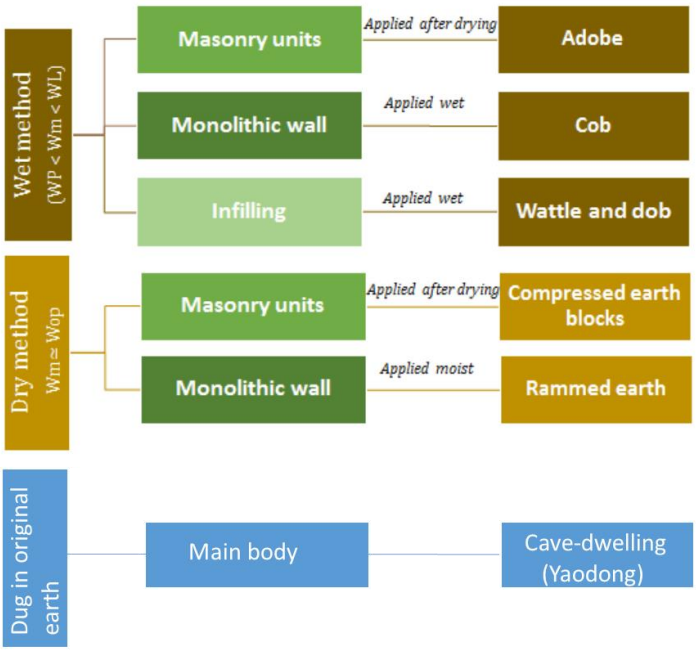

Figure 1.2 Classification for the earth construction techniques (Wm =manufacture water content, Wop = optimum Proctor water content; WP = water content at plastic limit; WL = water content at liquid limit)

1.1.1 Wattle and daub

Wattle and daub is perhaps the oldest earth-building technologies in the world. This technique consists of two parts, wattle and daub: a wattle is a woven structure of small plant elements held together in a stiff frame; common materials used to create wattle are reeds, bamboo, branches and twigs. Daub or mud adheres to the irregularities and overhangs of the organic matrix. The daub is then smeared on to the wattle by hand until the entire surface is covered. After drying, either the finish surface can be a smooth final coat of daub, or it can be whitewashed with lime. This technique is for the construction of non–loading bearing walls, either partition walls or external walls, with widths between 8 cm and 20 cm. It is the wattle who holds the bearing capacity rather than the earth, and the wattle (woven structure) is highly earthquake resistant because it is extremely flexible. This is the reason why wattle and daub is often used in seismic zones throughout the world such as South America and Indonesia(Niroumand et al. 2013). Figure 1.3 (a) presents the construction process using wattle and daub technique, Figure 1.3 (b) shows a house made of wattle and daub in Colmar France.

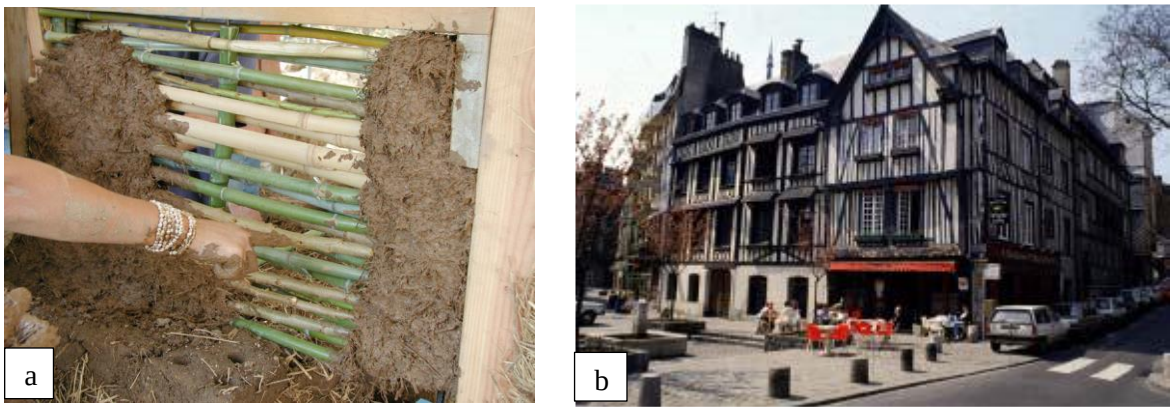

Figure 1.3 (a) construction process using wattle and daub technique (b) house made of wattle and daub in Colmar France

1.1.2 Adobe and compressed earth blocks (CEB)

Adobe is also an ancient construction technique involving pouring a wet mixture of clay soil into parallelepiped moulds with dimensions of conventional bricks; the wet soil can also be mixed with organic fibres. After this, the adobes are left in the sun to dry for several days and then used to build masonry structures likewise ordinary fired bricks. Stabilizing agents such as mud and mortar are used for manufacturing adobe bricks. Other additives like asphalt emulsion, lime and cement have also been used in mud bricks and walls. It is worth noting adobe bricks have offered simple structural solutions for structures such as vaults, arches and domes, which

are impossible to construct with rammed earth. Manufacture process for this type of technique is shown in Figure 1.4.

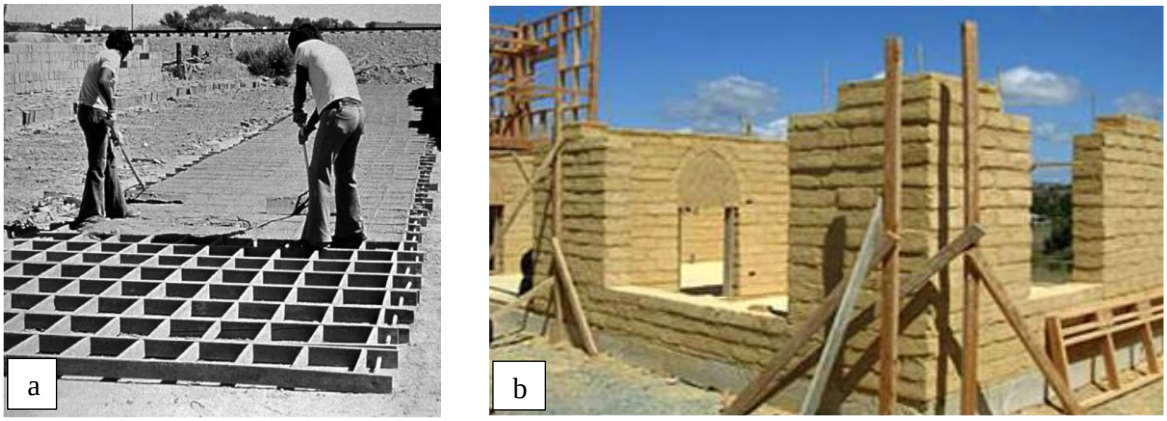

Figure 1.4 (a) adobe bricks manufacture process (b) house construction using adobe bricks

CEB (compressed earth blocks) technique is often considered to be an improved form in modern earth buildings compared to adobe in traditional earth construction. This method consists of using specific presses to compact moist soil to a relatively high density inside a mould. The pressure can be applied manually or mechanically (Figure 1.5(a)). Blocks are subsequently assembled as masonry structures without mortar but with a thin joint of mud slurry to compensate surface roughness and enhance airtightness. Figure 1.5(b) shows an example for apartments in France made of CEB blocks.

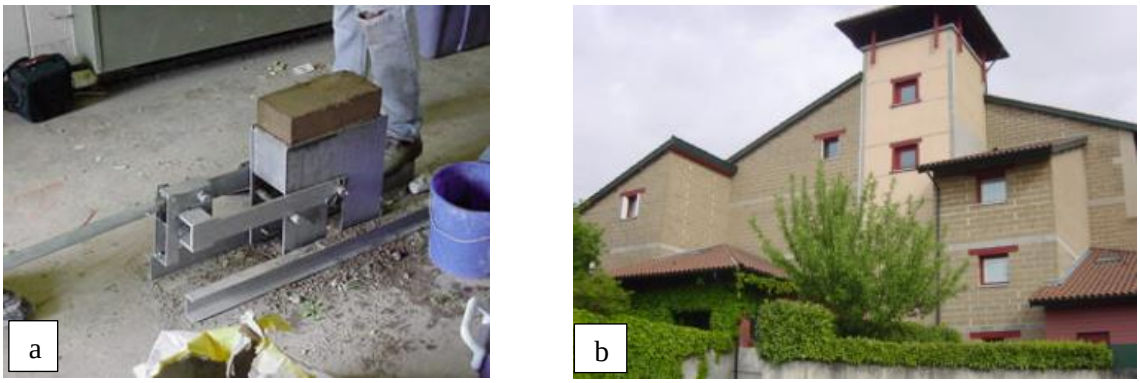

Figure 1.5(a) CEB manufacture process manually (b)house built with CEB in Rhone-Alpes France

1.1.3 Cob

Cob seems to be the simplest one of all earth-building technologies. This technique makes use of very few tools and no formwork or internal structure and consists of piling and molding mud to create walls. For this type of construction, the earth is moderately wetted and is often mixed with organic fibres (e.g. straw, reed or heath) which helps the mud hold its form as it is piled. Mud is shaped using trowel or hand and is placed directly in top of a structure. Since cob is

implemented at plastic state, its mechanical resistance is low and the material subsides under its own weight during construction process. The height of wall done in a same time was limited. As a result, cob walls were a superimposition of successive monolithic earth raised, called lifts (Fodde 2009; Forster et al. 2008). The height of a lift varied with soil type, plasticity and stress applied on the wall during construction. Lift heights ranged from 10 to 120 cm with an average of 59 cm. Wall thicknesses ranged from 10 to 150 cm with an average of 62 cm. A new lift was realized when the previous one was dry enough (about two weeks depending on the climate) to bear the weight of the new lift without deforming. Cob building is therefore time-consuming, but highly sculptural and offers the flexibility of producing walls of variable shapes (e.g. non-rectilinear walls). Because of its simple nature, cob construction has become very common in the whole world. A wall under construction is illustrated in Figure 1.6 (a), meanwhile a house using cob technique in Ille-et-Vilaine (France) is also shown in Figure 1.6 (b).

As the cob material dried, it shrunk and shrinkage cracks could expand inside the lift. If this expansion was too large, this could lead to structural damages. Shrinkage rates depended on clay content and manufacture water content of cob mixtures, high clay content and high manufacture water content leading to high shrinkage rate. Hence, the technique requires a careful selection of materials and construction detailing.

Figure 1.6 (a) a wall under construction with cob (b) a house using cob technique in Ille-et-Vilaine France

1.1.4 Rammed earth

Rammed earth is a building technique involving in compressing a moist earth mixture layers by layers within the formwork. It is an ancient method that has been revived recently as a sustainable building technique used in modern earth buildings.

Manufacture of rammed earth

Rammed earth is always used for constructing foundations, floors, and walls. The construction of an entire rammed earth wall begins with a temporary frame, denominated the "formwork". In traditional construction, the formwork is usually made of wood or plywood (in Figure 1.7(a)), and plays a role of mould, ensuring desired shape and dimensions of each section of wall. The formwork must be durable and well braced, and the two opposing faces must be clamped together to prevent bulging or deformation caused by the large compressing forces. Nowadays, metallic shutters are being used, which allows a higher compaction energy (illustrated in Figure 1.7(b)).

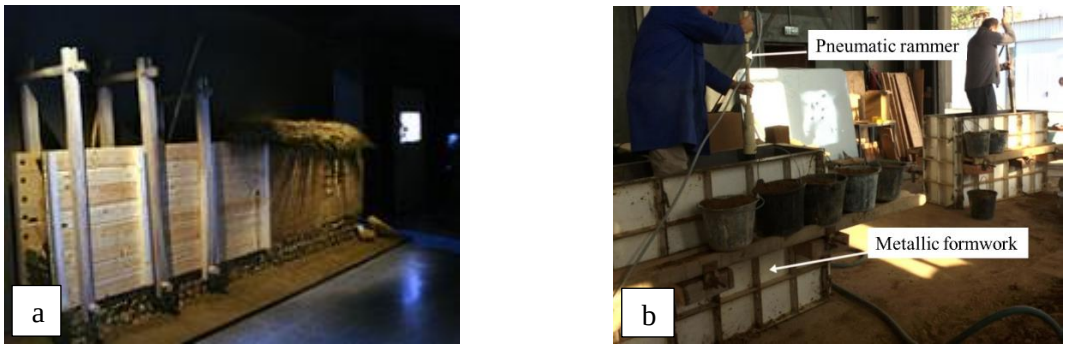

Figure 1.7 (a) Traditional wood formwork (b) metallic one used in the laboratory ENTPE Lyon

Moist earth is then poured into the formwork to a depth of 10 to 25 cm and compacted to approximately 50% of its original height. The material is compressed iteratively, in batches or courses, so as to gradually erect the wall up to the top of the formwork. Tamping was historically manual with a long ramming pole, and was very laborious, but modern construction can be made less so by employing pneumatically powered rammers.

When rammed earth wall is complete, it is sufficiently strong to immediately remove the formwork. This is necessary if a surface texture is to be applied, e.g., by wire brushing, carving, or mold impression, because the walls become too hard to work after approximately one hour. Construction is optimally done in warm weather so that the walls can dry and harden. The compression strength of the rammed earth increases as it cures; some time is necessary for it to dry and as long as two years can be necessary for complete curing.

Widespread use of rammed earth

A large number of beautiful and well-known construction wonders have been built through rammed earth. Examples of such great architectures include the Alhambra in Spain, the great Kasbahs of Morocco and the long stretches of the Great Wall of China. China has evidences of some of the most previous works built from rammed earth, where archaeologists discovered walls made of rammed earth back from the Longshan Culture of the Late Neolithic period

(between 2600 and 1900 B.C.E), the period between the Stone Age and the Bronze Age, a period when many cities in China were established. In the Fuijan province of central China, the round houses of the Hakka people have recently been given "World Heritage Site" status. These large rammed earth buildings, called Tulou (literally earth structures) are defensive homes to many families and can be up to 73.4 m across and four storeys high. The oldest of these buildings was built in 1308 and their construction continued well into the 20th century. This technology of building structures using rammed earth later spread throughout the Middle East. The Phoenician trading empire was the one that introduced the technology in Europe. The Romans spread the technology to southern France through the Rhone River valley, where they built the capital city, Gaul, which is called Lyon today (Capital of Rhone region).

In France, rammed earth structures are widespread especially in the Rhone-Alpes region where they represent around 40% of rural architectural heritage (Collectif FFB 2012). A lot of agricultural buildings and houses made of rammed earth date to more than 300 years and many are still inhabited, exhibiting excellent performance in terms of structural stability, durability and environmental comfort.

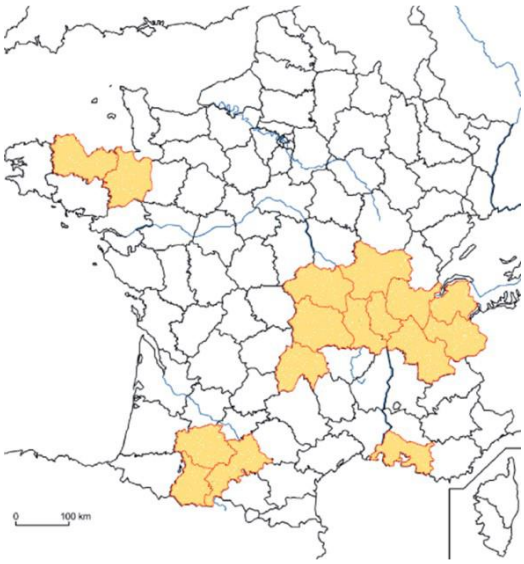

Figure 1.8 Regions of using rammed earth in France (Pignal 2005)

Currently, this construction method is becoming more popular because it meets the requirement of sustainable development. Rammed earth walls offer healthy indoor environments coupled with energy efficiency, long-life durability with low maintenance, as well as improved acoustics, improved seismic stability and fire barriers.

Modern rammed earth

Rammed earth can be divided into two categories: unstabilised rammed earth" and "stabilised rammed earth". The former is composed of clay, silt, and sand where clay acts as a binder between the grains (Q. B. Bui et al. 2011); while in "stabilised rammed earth", chemical binders, such as cement and lime, are added into the soil for increasing inter-granular bonds and enhancing macroscopic strength. Besides, stabilization also limits the sensitivity of earth to erosion. Hence, a large number of modern rammed earth houses were stabilized with lime or cement, particularly in Anglo-Saxon countries such as Australia, USA or India, where the proportions ranges from 6% to 15% (Maniatidis and Walker 2003). However, using stabiliser leads to the reduction of the permeability of soils and thus the natural ability of earth to allow moisture to pass. The stabilization of rammed earth greatly increases the cost of construction and the recycling of the material becomes very difficult. Many studies have shown that stabilized rammed earth increases the embodied energy (T. T. Bui et al. 2014; Venkatarama Reddy and Prasanna Kumar 2010).

Another modern practice consists in the prefabrication of rammed earth walls. The prefabricated earth walls are normally produced in large molds, then brought to the construction site to be put together. The pre-fabrication of these panels can be produced either on-site or in workshops. An example of a building constructed with pre-fabricated walls in Switzerland is presented in Figure 1.9.

Figure 1.9 Prefabricated rammed earth wall used to build Ricola's factory in Switzerland

1.1.5 Cave dwelling - Chinese Yaodong

Yaodong is a particular form of earth cave dwelling usually carved out of a hillside or excavated horizontally from a central "sunken courtyard" (Liu et al. 2005). This kind of earth structures make good use of structural strength of undisturbed soil. Yaodongs are commonly found in the north central provinces of China such as Shanxi, Shaanxi, Gansu and Henan, which are located on the Loess Plateau. It has been claimed that the use of Yaodongs can be dated back to the Qin

dynasty in the third century B.C. Over two millennia later, Yaodongs are still a popular choice of dwelling for those living on the Loess Plateau, as it is estimated about 40 million inhabitants of the Loess Plateau are still living in such structures.

Yaodong can be divided into different types, depending on the topography of the regions in which they were built. For instance, where hills are available, Yaodongs may be built into the slopes, and a hill may contain several stories of Yaodongs (illustrated in Figure 1.10 (a)). Where hills are not available, Yaodongs are simply built into the ground. Rectangular wells about 5 meters to 8 meters deep are first dug into the ground. After that, Yaodongs are built into the walls of these wells. The wells serve as a "sunken courtyard" for the inhabitants (Figure 1.10 (b)).

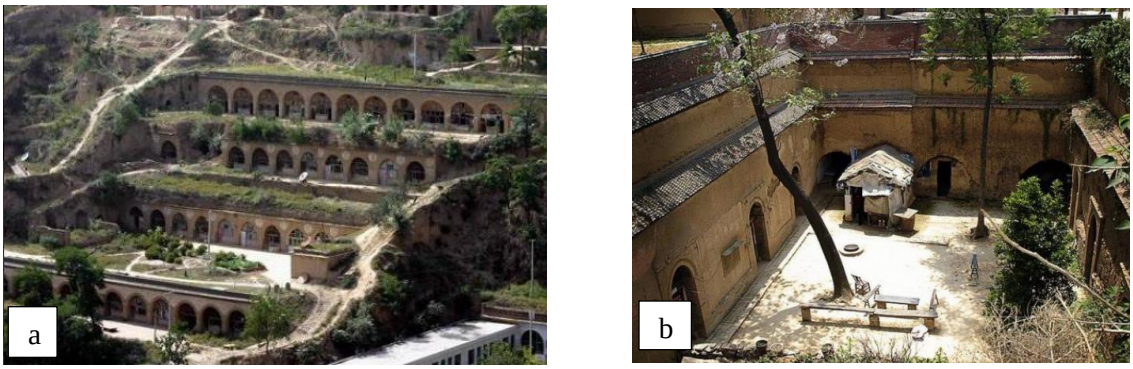

Figure 1.10 (a) Yaodong dig in the cliff on the edge of the loess slopes (b) Yaodongs built into "sunken courtyard"

The continuous use of Yaodongs on the Loess Plateau over the millennia can perhaps be attributed to its highly economical and efficient design. In terms of building material, only the local loess soil from the plateau is required for the building of the Yaodongs. Loess soil is the obvious choice of material as it is easily available in the area, as opposed to wood or stone. Additionally, loess soil is a good insulator of heat. The thick earthen walls are able to keep the interior of the Yaodongs cool during the summer and warm during the winter (Zhu et al. 2014). Nevertheless, despite the advantages of the Yaodong cave dwellings, they do have one significant disadvantage-they are highly susceptible to destruction from natural disasters

1.2 Advantages and limitations of earth materials

1.2.1 A sustainable construction material

The construction industry creates a litany of environmental impacts, partly due to its large consumption of energy (Hendrickson and Horvath 2000). According to the statistics, the building sector accounts for about 40% of the generation of greenhouse gases; moreover,

construction is also responsible for high levels of pollution and produces a large amount of waste. It is reported that around 44% of the wastes collected in France come from the building industry (ADEME 2015).

In the context of sustainable development, more acute problems are related to energy and wastes and all sectors are working to reduce the environmental impact of their activities, which triggered new interest in alternative building materials with environmentally friendly characteristics. Among these, earth is one of the most attractive options because it can help reducing the energy consumption of the building sector. These materials are extracted directly on the construction site (or near the site) like raw soil and then transformed into construction material with a very low manufacturing energy. Earth is also recyclable, inexhaustible and, when properly manufactured, offers high strength, excellent hygro-thermal properties and low embodied energy at very low costs. Because of these attributes, earthen materials can dramatically reduce exploitation of natural resources not only during construction, but also during service life, by cutting down on heating/air conditioning needs, and at the end of life, by limiting demolition waste. The advantages of earth as a building material are summarized below:

Reduction of embodied energy-construction stage

As a kind of local non-industrial materials, raw earth is extracted directly on the construction site or near the site. Afterwards, implementation is conducted using manual and/or mechanized means. The recourse to mechanized means and possible transportation of earth increases the embodied energy of buildings. However, the embodied energy of modern unstabilized earth construction remains very low in comparison to other materials conventionally used in construction. Table 1.1 presents a comparison of the energy consumed between a typical concrete house and a house made of a local material (house made of rammed earth and house made with stone masonry). It is observed the energy consumed in rammed earth is far smaller than that in concrete.

Table 1.1 Energy consumption for different construction types (J. C. Morel et al. 2001)

	Masonry	Rammed earth	Concrete
Energy (GJ)	97	70	239
Transport (t.km)	1390	1041	6707

Indoor comfort- maintenance stage

During the living period or maintenance stage of earth buildings, their high thermal mass contributes to the buffering of temperature and relative humidity variations. An important part of this thermal inertia derives from the phase change of water (Collet et al. 2006; Soudani et al. 2016, 2017). In consequence, they are able to accumulate solar energy during the day and restitute this energy during the night. These features provide to inhabitants of earthen buildings a good thermal comfort and more specifically during summer period. Figure 1.11 illustrates the comparison of temperature buffering between inside and outside of an earth house (Soudani 2017).

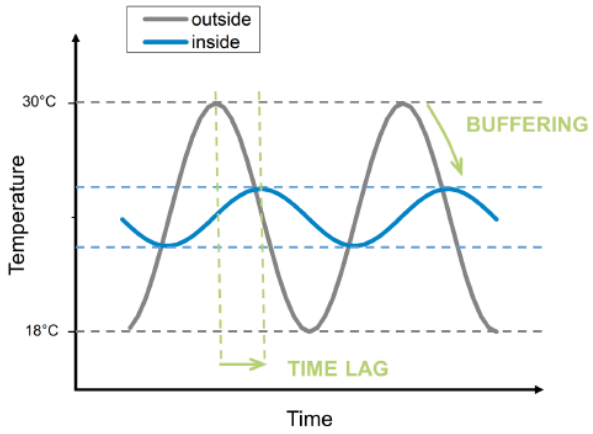

Figure 1.11 comparison of temperature buffering between inside and outside of an earth house (Soudani 2017).

Thanks to their high hygroscopic ability, earthen materials are believed to absorb pollutant, thus may improve indoor air quality which is beneficial for health and well-being of the occupants. In addition, several other beneficial properties of earthen buildings such as: good acoustic properties, fireproof properties, non-toxic and non-allergic properties have also been mentioned in literatures (Sameh 2014; Sharma et al. 2016). All these advantages owned by earth buildings contribute a better indoor comfort in comparison with the conventional construction type.

Recycle of earth materials-renovation and demolition stage

It is reported that demolition and destruction phase accounts for about 56% of all building wastes with a total of 31 million of tons for the year 1999 in France (Q.-B. Bui 2008). In this respect, unstabilised earth presents considerable advantages over conventional construction materials because demolition waste consists mainly of ordinary soil that can be easily recycled or safely released into the environment with no need of special treatment or specific storing techniques. This is not the case of stabilized earth construction. Indeed, even if stabilization could increase the durability of buildings, the stabilisation of thick earthen walls, even at low percentage, will prevent the reuse of the material at end of life.

1.2.2 Limitation and vulnerability of earth material

Earth construction exhibits many advantages in terms of environmental impact, indoor comfort and sustainable developpment. However, there are still some vulnerabilities remained in this field, which hindered its adoption within mainstream market:

Proper local earth selection

Suitable earth for construction should be a mixture of gravel, sand, silt and clay, in which clay plays a very important role of binder. Therefore, the soil particle size distribution is of vital importance to the material strength and durability. Many work have already been done to give the recommended maximum and minimum grain size distribution of earthen materials (Jiménez Delgado and Guerrero 2007; Maniatidis and Walker 2003; Peter Walker et al. 2005). Priority of soil used in earth construction should come from the site directly or near the site. If earthen material with the recommended proportions is not available locally, suitable constituents must be quarried further away and transported to site with consequent increases in energy consumption and financial costs.

The bonding coming from the clay fraction is the main source of strength in unstabilised earth. But as a hygroscopic material, the clay fraction interacts with the atmosphere by absorbing, storing and releasing moisture as the ambient humidity varies, hence an interactive effect with water will occur thereby inducing several unexpected influences on the earth building: e.g. grievous shrinkage after construction, large swelling behavior during maintenance stage and non-negligible residual deformation by cyclic loading. All these factors mentioned above indicate that a proper clay content should be carefully considered when selecting the local earth.

Sensitivity to water

Earth belongs to a porous material even though most of earth buildings (like rammed earth) have been compacted and the void ratio becomes smaller. Due to this intrinsic characteristic, water or vapor can easily penetrate into soils, thereby modifying the intensity of capillary forces hence also the strength of the material. As a consequence, the durability and strength of earth building under various climatic conditions is an important issue to be addressed. In dry climates, raw earth is very durable, as demonstrated by the large number of well-preserved earthen structures dating back to hundreds, or even thousands, of years ago. In wet climates, rainfall

causes surface erosion, especially in unstabilised earth structures, which can lead to substantial reduction of life span.

Despite protections (including roof and foundation) usually made to deviate stream waters from the foundations and to avoid water concentrations which could further cause erosion, exposure to humidity under normal working condition cannot be totally avoided for the earth buildings. The mechanical properties are inevitably affected.

Deficiency of earth guidelines

Although some countries have published their own earth construction guidelines, a lot of uncertainties remain when considering the design methodologies in these standards based on empiricism and practical know how rather than engineering science. In addition, there are no uniform and internationally accepted laboratory testing procedures for determining material properties and design values for earth building constructions. The test procedures currently in use were often originally developed for testing soils (soil mechanics) or concrete and did not take into account the specific properties of earthen materials. The suitability of these 'adopted' procedures for earthen building materials and systems is still to be proven.

1.3 Research objectives

Compacted earth is considered as a granular mixture in which clay plays an essential role of binder, but is sentitive to water. During their service life, compacted earth can be subjected to large changes in relative humidity. Those perpetual changes of environmental conditions induce continuous changes of water content of the earth that impacts significantly its mechanical performance. The present work is aimed at investigating the mechanical behavior of compacted earth with respect to relative humidity and clay content. It involves an extensive experimental study and constitutive modelling. The main explicit scopes of the present study are:

- To draw some preliminary insight and understanding in regard to the effect of clay content and relative humidity on the local raw earth materials.
- To study the impact of clay content and relative humidity on the mechanical performance (strength, stiffness, residual strain). The independent and interaction influence of these two factors will be investigated based on one type of local raw earth and two types of artificial prepared earth.
- To propose an advanced hydromechanical constitutive model, based on the experimental results, specifically for compacted earth.

In order to reach these objectives, the following actions must be realized: making a preliminary identification of local raw earth materials; carrying out an exploration on the compaction method related to the fabrication of samples and it involves a double static compaction and dynamic compaction (Proctor test).

1.4 Thesis layout

The thesis is divided into six chapters:

Chapter 1 retraces the history of earth constructions and analyses the advantages and limitations of using earth as a construction material. The main objectives of the present study are also outlined.

Chapter 2 reviews the current state of knowledge concerning the experimental study and constitutive modeling of earth mechanical behaviour. This chapter presents the required principal concepts and provides the background to the study. Insufficiencies in the present state of knowledge are also pointed out.

Chapter 3 presents the results on the identification of four local raw earth materials. Some conclusions drawn from the comparison between two kinds of compaction methods are also indicated. Some preliminary insight and understanding in regard to the effects of clay content and relative humidity on local raw earth materials are also obtained through three specific laboratory tests.

Chapter 4 reports results from triaxial loading-unloading tests conducted to measure the stiffness, strength and residual strain of compacted earth with three controlling factors: relative humidity, clay content and confining pressure respectively. This chapter also describes a procedure to determine a unique failure state line regardless of suction and confining condition.

Chapter 5 presents the formulation of a poro-elastoplastic damageable constitutive model for compacted earth using Bounding Surface Plasticity (BSP) theory, incorporating stiffness degradation and suction hardening. The validity of the model is assessed by simulating the experimental results of this study.

Chapter 6 summarizes the main contributions of this thesis and gives some perspectives for future studies.

Chapter 2
Overview of earth mechanical behaviour: experimental investigation and modelling development

2.1 Experimental investigation on the mechanical behaviour of earthen materials

Understanding the hydro-mechanical behaviour of earth constructions is of vital importance to their durability. In the past decades, several studies have been carried out to analyze earth mechanical properties, either through field tests or by a series of laboratory tests, such as unconfined compression test, triaxial test, splitting and flexural test etc. Bruno (2016) classified the earth mechanical properties into the following two types according to their working state:

(1) Failure state: A failure state means the main frame has disintegrated to a point where basic conditions no longer function properly. When talking about earth materials, it usually refers to the failure compressive strength (noted as f_c) which is calculated using the maximum force (divided by the surface area of the sample) that a material can withstand in a compression test (unconfined or triaxial).

(2) Serviceability state: During its service life, earth construction is subjected to loads that will produce deformations even far from failure state. By applying a cyclic loading and studying the stress-strain relationship, the properties corresponding to the serviceability state can be determined (e.g. Young's modulus *E*, poisson ratio, and residual strain)

There are a lot of factors influencing the earth mechanical behaviour, from external interferences (such as test procedure, sample geometry) to inherent properties (e.g. dry density, moisture content, and clay content).

2.1.1 Sample geometry

Bui et al. (2009) evaluated the mechanical performance of rammed earth from the following three different experiment scales (in Figure 2.1):

- Scale 1: Full scale (in-situ test)
- Scale 2: Representative Volume Elements (RVE)
- Scale 3: Equivalent compressed earth blocks (CEBs)

Among these, the second scale is widely used in existing research on earth mechanical behavior, since this approach is classic in continuum mechanics and easy to operate in laboratory. As long as the mode of fabrication and the materials are chosen properly, samples fabricated in the laboratory can provide a good representation of in-situ earth. The representative specimens can

either be cylinders or prisms (including cubes). Table 2.1 summarizes the geometry of representative specimens in literatures.

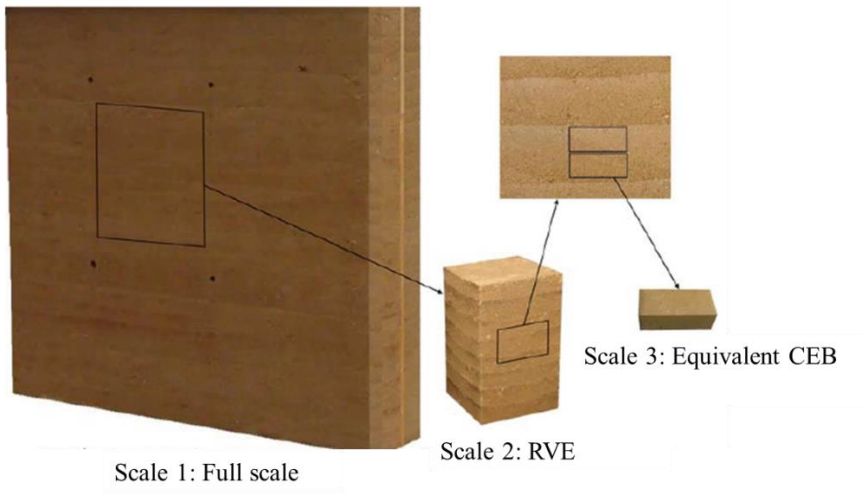

Figure 2.1 Three scales for rammed earth studied by Bui et al. (2009)

Table 2.1 Examples of the sample geometry in literatures

	Dry density (g/cm^3)	Geometry (cm)	Aspect ratio
M. Hall and Djerbib (2004)	2.02-2.16	Cube 10	1
Lilley and Robinson (1995)	1.87-2.17	Cube 15	1
Maniatidis and Walker (2003)	1.85	Cylinder D 10 H 20	2
Maniatidis and Walker (2003)	1.76-2.03	Prism 30×30×60	2
T. T. Bui et al. (2014)	1.92	Cylinder D 16 H 32	2
Piattoni et al. (2011)	Not Mentioned	Prism 46×31×13	0.42
		Prism 23×15×13	0.87
Ciancio and Gibbings (2012)	2.09	Cylinder D 10	From 0.75 to 2

There is no doubt the geometry can affect the measured values of compressive strength. Test results depend very much on the aspect ratio between height and width (prism)/ diameter (cylinder). This is because the friction between press plates and sample faces creates stronger confinement for samples with a lower aspect ratio, thus generating an apparent increase of strength. Piattoni et al. (2011) carried out compressive strength tests on two geometries of samples (46×31×13 (cm^3), aspect ratio = 0.42; and 23×15×13 (cm^3), aspect ratio = 0.87) and compared the results with those obtained on a wall of similar composition (aspect ratio = 2.55). They observed a significant increase in the compressive strength with decreasing aspect ratio: from 6.56 MPa for samples of aspect ratio= 0.42 to 1 MPa for the walls. In fact, different experimental studies seem to indicate that this additional boundary effect becomes negligible

when the samples have a slenderness ratio equal to or higher than two. Another detailed exploration on the effect of slenderness ratio and boundary conditions were carried out by Ciancio and Gibbings (2012). In their study, three different boundary conditions, including grinding flat the end surfaces, plywood blocks and plaster capping, were applied respectively on a series of cylinder cement-stabilized rammed earth samples with slenderness ratio equal to 0.75, 1, 1.25, 1.5, 1.75 and 2. It is concluded that for cylindrical samples with slenderness ratio equal to 2, the boundary conditions do not have a significant influence in the determination of the unconfined compressive strength.

Hence, in our study, a cylindrical specimen form with slenderness ratio equal to 2 (3.5cm in diameter and 7 cm in height) is adopted. It is fabricated by a home-made double static compaction mould. More details about sample fabrication will be described in next chapter.

2.1.2 Dry density

A number of studies have investigated the relationship between earth density and mechanical properties. They show that in general the compressive strength increases along with the dry density. Thus, when the material becomes denser, i.e. the particles are closer to each other, the compressive strength increases.

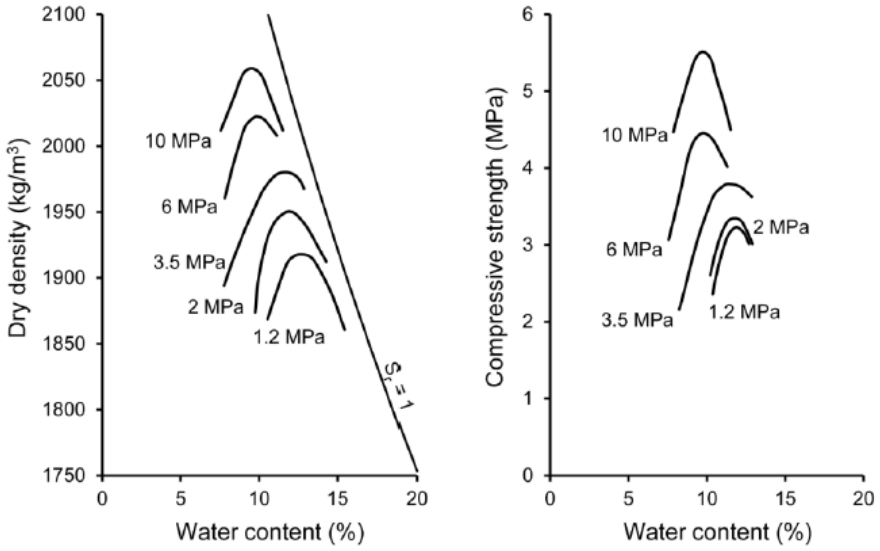

Figure 2.2 Compaction curves and variation of compressive strength with water content and compaction pressure (Olivier and Mesbah 1986)

Olivier and Mesbah (1986) studied the effect of the static compaction pressure on the mechanical properties of the "Isle d'Abeau" earth, using cylindrical samples at different pressure levels (from 1.2 MPa to 10 MPa). The optimum water content and the corresponding

maximum dry density for each compaction pressure is determined through testing at different water contents. After compaction, samples were stored at constant temperature (27 °C) and relative humidity (60%) and then tested under unconfined compression until failure. Results in Figure 2.2 confirmed that compressive strength increases as dry density increases.

Another study by Morel et al. (2007) also verifies this point. Compressive strength of compressed earth blocks, made of both stablilised earth and unstabilised earth, is strongly related to dry density achieved in compaction. Compressive strength of individual blocks consistently increases with increasing density, as shown in Figure 2.3.

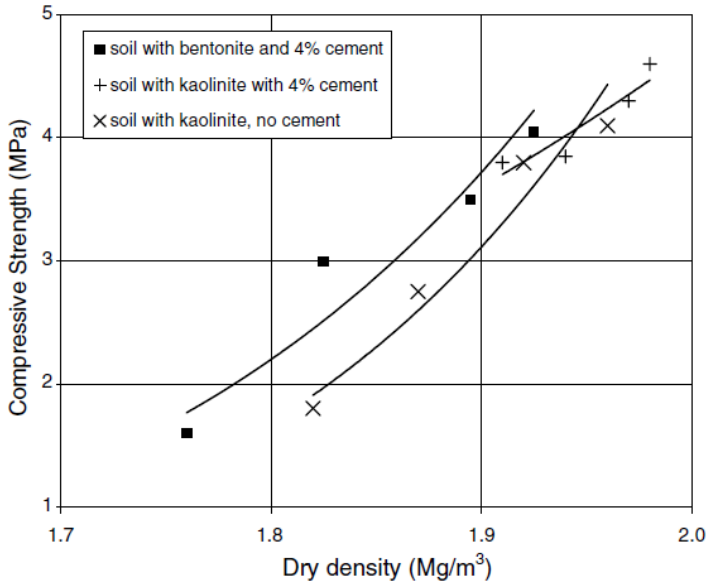

Figure 2.3 Variation of compressive strength with dry density (Morel et al. 2007)

In another study by Kouakou and Morel (2009), a very argillaceous earth with 25% clay content was used to fabricate two types of adobe: traditional adobe blocks and pressed adobe blocks (PABs). Traditional adobe blocks were manufactured by pouring the clay-water mixture at high water content inside wooden moulds with dimensions of 310×150×73 mm^3 and subsequently drying the demoulded blocks to the sun. Pressed adobe blocks were instead manufactured at much lower water contents and compressed to 2 MPa for increasing density. Both of these two kinds of adobe were cured in the laboratory at room temperature (22 °C) with a humidity of 60% until the block weight became constant. After curing, an unconfined compression test including three loading-unloading cycles at 30% of the compressive strength was carried out in order to determine their compressive strength, initial tangent modulus (E_t) and equivalent modulus during cycles (E_{eq}).

Results (illustrated in Figure 2.4) indicate that the compressive strength of adobes and PABs increases with dry density. Adobe and PABs have an elastoplastic behavior with accumulated

residual strains over subsequent cycles. Their stress–strain curve in unconfined compression gives two moduli, the initial tangent modulus (E_t) and the equivalent modulus (E_{eq}). These two moduli are different and do not vary significantly with the dry density.

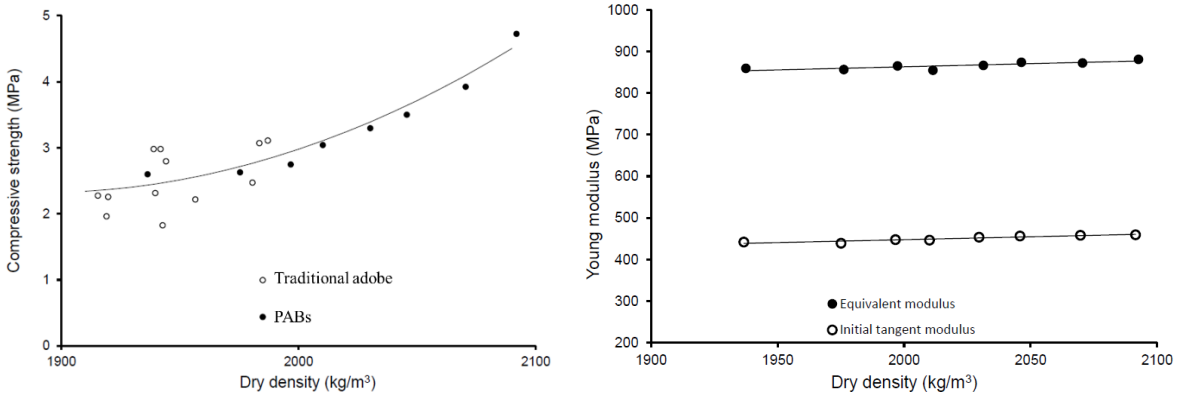

Figure 2.4 Variation of adobe compressive strength and Young's modulus with dry density (Kouakou and Morel 2009)

2.1.3 Clay minerals, effect of clay content on mechanical behaviour

Unstabilized earth material can be regarded as manufactured unsaturated soils. A general view of the mineralogy and earth structure is supposed to be illustrated based on the fundamental knowledge of soil mechanics (Hall et al. 2012). It has commonly been recognized that an unsaturated soil is a three-phase mixture, containing solid, liquid and gaseous phases. The solid phase is constituted of soil grains, which form a deformable solid skeleton (porous matrix). The fluid phases consisting of liquid and gaseous phases are able to flow through the voids of this skeleton. The liquid phase of most soil systems is composed of water containing various types and amounts of dissolved electrolytes. The gaseous phase, in partially saturated soils, is usually a mixture of several gases (dry air) and water vapour. The mutual interaction between these two fluids and their interactions with the soil skeleton play a key role in the mechanical and hydraulic response of unsaturated soils (Laloui 2013).

This section presents minerals commonly found in an earth and their corresponding compositions and structures, thereby providing intuitive insight as to their effects on mechanical behaviour.

Hierarchy of clay minerals

(1) Clay unit cell

The composition of earth used for constructions varies greatly and always contains clay but should not include any organic components. Clay acts as the binder between the grains, a

mixture of silt, sand, and gravel up to a few centimeters diameter (Q.-B. Bui et al. 2014). At the microscopic scale, the clay minerals are a group of hydrous aluminium silicates that are characteristically found in the clay fractions of sediments and soils (Reeves et al. 2006). As schematically illustrated in Figure 2.5, the layered structures of common silicates are made up of combinations of two simple structural units, the silicon tetrahedron and the aluminium or magnesium octahedron (Lei 2015).

- Silica tetrahedral sheet (also known as silica sheet) consists of two dimensional arrays of silicon-oxygen tetrahedral. These tetrahedra are interconnected in such a way that the bases of the tetrahedra are all in the same plane and all the tips point in same direction.
- Aluminium or magnesium octahedral sheet consists of two dimensional arrays of aluminium/magnesium-oxygen-hydroxyl octahedral.

(2) Clay layers

The unit cells are joined in spatial articulation to form basic unit clay layers. A unit layer is a basic repeating structural element of a clay mineral. Two types of composite layer structures in the clay minerals can be identified and illustrated in the middle position of Figure 2.5:

- The two-layer or 1:1 type represented by the kaolin and halloysite groups;
- The three-layer or 2:1 type represented by the pyrophyllite, montmorillonite, vermiculite, illite and chlorite groups.

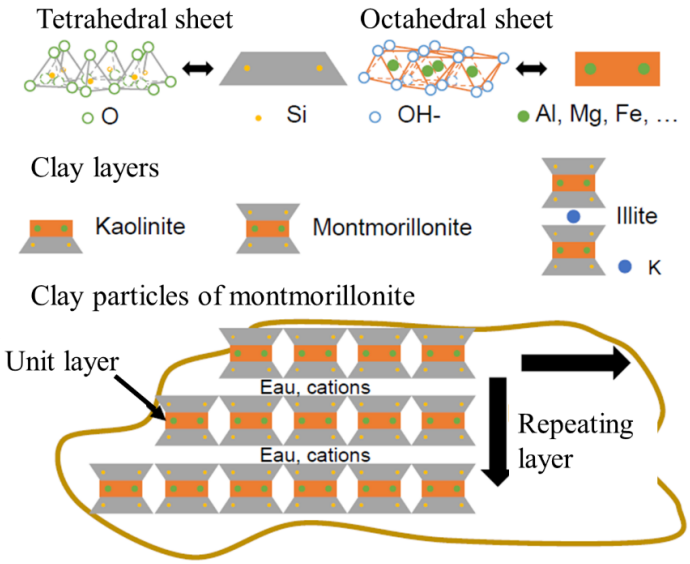

Figure 2.5 Schematic representation of microstructure units of clay minerals (Modified after CHAMPIRE (2017))

The unit layers of clay minerals are very thin with similar length and width. Since their edges are seldom straight, the unit layers can be visualised as thin flakes.

(3) Clay particles

A typical feature of clay minerals is that the layers usually do not exist as single units but combine to form stacks (as shown in the bottom portion of Figure 2.5). Such stacks represent clay particles, with 3-10 aligned coupled layers-depending on the bond strength (Pusch and Yong 2014). The bonding between unit layers is, however, qualitatively different in the two clay mineral types. In kaolinite, the bonding of unit layers is by a combination of both hydrogen bonds and van der Waals forces. This type of bond is sufficiently strong to prevent swelling between unit layers in kaolinite. In contrast, the bonding between unit layers in montmorillonite is by cations (which are attached to the surfaces of unit layers to balance the electric charge deficiencies) or by van der Waals forces. This type of bond is weak, and therefore, separation of the unit layers or swelling can occur when a polar liquid like water is available (Lei 2015).

(4) Aggregate

Generally, there exist several types of soil particle structural units in a clay soil. The bonding forces and energies of attraction between particles are considerably larger than the energies of repulsion, which results from an aggregation of particles acting as a single unit (Pusch and Yong 2014). These aggregations of particles are the backbone of the macrostructure of clay soils.

Clay soil structures

The organization of the layers, particles and aggregates in a clay soil gives rise to different types of pores (Villar 2004). Based on the research from Lei (2015), the following three types of porosities as well as their corresponding pore water can be identified:

- Interlayer porosity and interlayer adsorbed water

These pores relate to the interlayer space between the unit layers which contain cations and water molecules, to which only polar molecules have access. Water molecules occupying this porosity is influenced by the electrical field and is strongly bounded, as a result of which its properties are very different from those of free water. They have less mobility and are termed as interlayer adsorbed water.

- Intra-aggregate porosity and external adsorbed water

These pores are located inside the primary particles and between adjacent laminae piles (stacks), also known as lenticular porosity or microporosity. The diffuse layers develop in these pores. The water body that forms part of the diffuse layers is usually termed as external adsorbed

water. They contain cations and anions, but with an excess amount of one of them (normally cations at normal pH) to balance the charge of the clay surface.

- Inter-aggregate porosity and free water

Inter-aggregate porosity is always classified as macroporosity or mesoporosity with respect to the intra-aggregate porosity. In these pores, the water is retained by capillary or gravitational forces, and is known as free water.

A schematic diagram of the above-mentioned types of porosities and water in clay soil is given by Figure 2.6. Two levels of soil structure are distinguished in this solid-pore system: (a) at the macroscopic level, the soil is considered as a complex of clay aggregates, with the associated inter-aggregate pores (macropores) between them which can be filled by either free water or gases; (b) inside each aggregate, the microstructural system consists of several closely packed clay particles and the intra-aggregate pores between or within particles which are referred to as micropores, corresponding to adsorbed water (both interlayer and external)

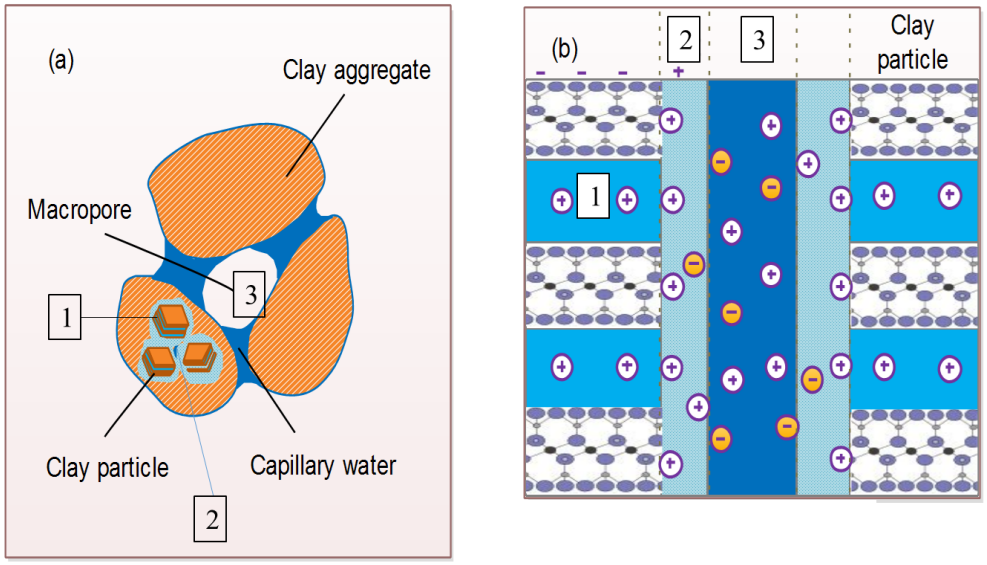

1 Interlayer porosity
2 Intra-aggregate porosity
3 Inter-aggregate porosity

1 Interlayer adsorbed water
2 External adsorbed water
3 Free water

Figure 2.6 Schematic representation of clay soil structures at macroscopic and microstructural level (Modified after Lei (2015))

Influence of clay content on the mechanical behaviour

The aforementioned studies indicate that clay mineral plays an important role in controlling the insides structures of earth material. In view of this, understanding of earth mechanical behaviour should take into account the presence of clay as well as its interactions with other phases. However, clay content is always purely regarded as a preliminary granular index to

evaluate the suitability of soil in the construction, mostly through an empirical knowledge rather than a systematic parametric study. Until now, there were only few studies on the subject.

Hamard et al. (2013) prepared a series of earth plasters with different clay contents of 18%, 12%, 9%, and 6% in dry weight, by adding Hostun sand to two kinds of raw earths (named earth 1 and earth 2). Earth plaster's longitudinal shrinkage for samples of 40 mm×40 mm×160 mm were obtained by measuring the length of specimen, thanks to a ruler, before and after drying. Meanwhile, three-point bending tests were also carried out on these specimens. Figure 2.7 presents the evolution of shrinkage and bending strength with clay content.

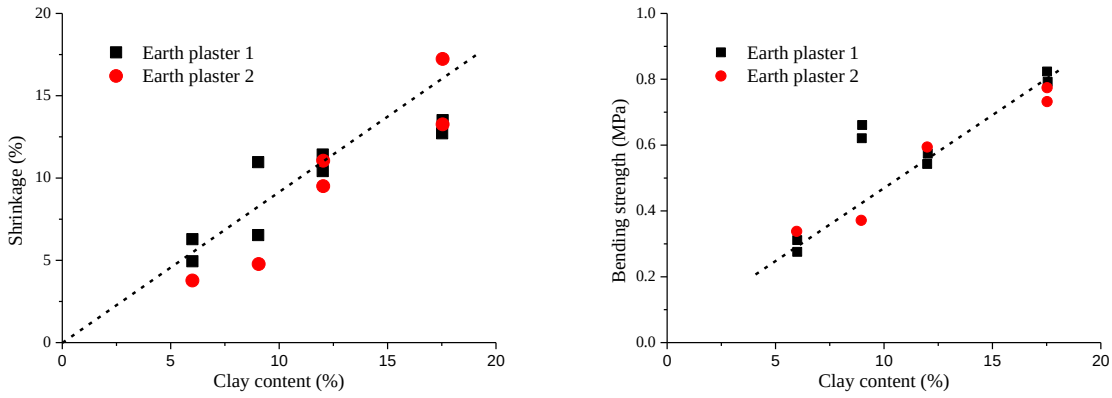

Figure 2.7 Variation of shrinkage and bending strength with clay content
(Modified after Hamard et al. (2013))

The results indicate higher clay content results in a greater amount of shrinkage. This observation is consistent with the study made by C H Kouakou and Morel (2009) for earth mortars and adobes. The bending strength of the earth 1 and earth 2 plasters increases with clay content. Hence, they conclude that an increasing of clay content will contribute to the development of shrinkage, thereby providing a higher dry density and a higher mechanical strength. Other researchers' studies also verified the above viewpoints through the study on the ready-mixed clay plasters (Delinière et al. 2014; Emiroğlu et al. 2015). Similarly, Taylor et al. (2006) reported an increase of the compressive strength of earthen plasters with increasing clay content, while the stiffness modulus was not affected.

In some other studies, conflicting opinions have been raised on the effects of clay content on the strength. Helson et al.(2017) reported that an increase of clay content did not result in an increase of unconfined compression strength (UCS) all the time, indicating the existence of an optimum clay content corresponding to the strength for clay plasters. In addition, a decrease of dynamic Young's modulus E_{dym} with increasing clay content is also observed. Kim et al. (2016)

conducted a series of cyclic triaxial tests on sand-clay mixtures with various sand-clay ratios. A threshold fines content was identified by consistency tests. The trend of cyclic strength variations observed was quite different below and above this threshold.

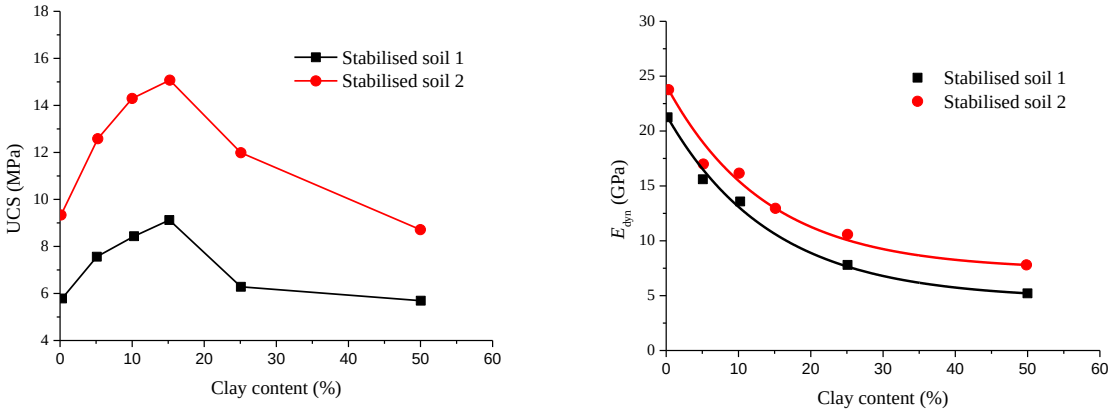

Figure 2.8 Variation of adobe compressive strength and Young's modulus with dry density (Modified after Helson et al.(2017))

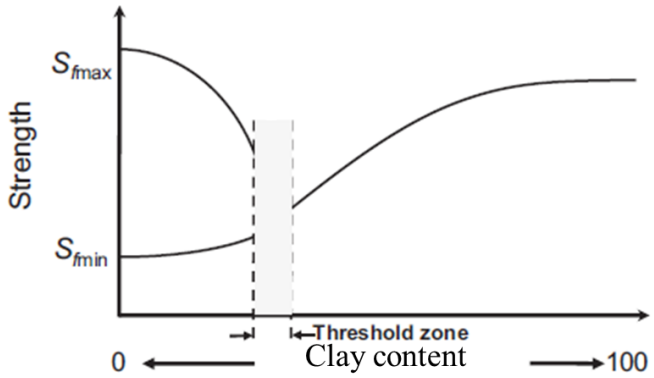

Figure 2.9 Schematic representation of clay thread zone (Kim et al. 2016)

S_{fmax} and S_{fmin}: maximum and minimum of cyclic strength

The aforementioned studies tend to focus on evaluating characteristics of clay plasters and few of them consider the interactions between clay content and moisture content. In view of the lack on this observation, a comprehensive investigation on the compacted unsabilised earth, considering the combined influence of both clay content and moisture content on the mechanical behaviour will be presented in this thesis.

2.1.4 Suction and its influence on earth mechanical behaviour

In partially saturated soils, three kinds of pore water (interlayer adsorbed water, external adsorbed water, and free water) occupy the pore space with specific energy states. The energy state is evaluated in terms of water potential which is the potential energy of water relative to pure water in a reference state and quantifies the tendency of water to move from one area to

another due to osmosis, gravity, pressure gradient, or capillarity (Koliji 2008). The equivalent of the water potential expressed on volume basis and with opposite sign is called suction (Gens and Olivella 2001). The major components of soil suction include matric suction s_m and osmotic suction s_o. Matric suction is due to the capillary force existing in the soil matrix while osmotic suction arises from the dissolved salts contained in the soil water. The sum of these two components is termed total suction s.

$$s = s_m + s_o \tag{2-1}$$

Capillary or matric suction

Capillarity originates from mutual interactions of different interfaces between solid, liquid and gas phases. It may be defined in terms of matric suction, and depends on the surface tension of the pore fluid, the degree of saturation, and capillary radius.

As shown by Figure 2.10(a), the surface tension is due to an imbalance between intermolecular attractions at a boundary surface separating two immiscible fluids (Laloui 2013). In cases where the wetting fluid is liquid water and the non-wetting fluid is dry air, there is a difference between the forces experienced by the water molecules belonging to the bulk water in a pore and the forces exerted on the molecules on the liquid surfaces. In bulk liquid, the forces acting on a molecule are effectively equal in all directions and the molecule feels no net force. As a molecule moves to the surface, it loses some nearest neighbours, thus leaving it with unbalanced attractive forces with an inward resultant (Lu and Likos 2004). For a molecule to stay in the surface region, it must gain excess energy (and entropy) over those in the bulk liquid. This excess energy (surface free energy) is the origin of surface tension phenomena and causes the surface to act like a membrane in tension, which tends to minimise its area.

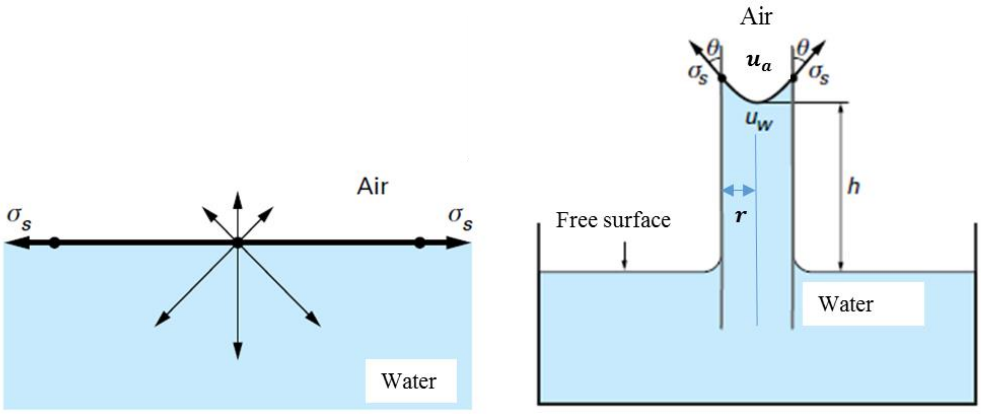

(a) (b)

Figure 2.10 Schematic illustration of (a) surface tension at the gas-liquid interface (b) matric suction generated by meniscus concave on the air side

When in contact with a solid surface, the water-air interface will curve near that surface to form a meniscus, as shown by Figure 2.10(b). Menisci that are concave on the air side render the water pressure u_w lower than the air pressure u_a. Matric suction s_m is then defined as the difference between pore air pressure u_a and pore water pressure u_w. Let us consider a meniscus in a capillary tube of radius *r*, as illustrated in Figure 2.10(b). The water pressure at the back of the meniscus can be calculated by considering the vertical force equilibrium of the air-water interface:

$$s_m = u_a - u_w = \frac{2\sigma_s}{\delta} = \frac{2\sigma_s \cos\theta}{r} \tag{2-2}$$

where σ_s (N/m) is the surface tension measured as the tensile force per unit length of interface, θ (°) the contact angle between the water and the boundary, and δ (m) the radius of curvature of the interface. As can be seen, the pressure drop across the curved interface is directly proportional to the interfacial tension and inversely proportional to the radius of curvature.

Osmotic suction

Osmotic suction arises as a result of a reduction in the chemical potential of the pore water in clays due to the presence of dissolved salts in the pore water (Y. Xu et al. 2014). Thus, a gradient in chemical potential is developed that causes water (solvent) to flow from the pure water into the salt solution through clays. Equilibrium is reached when the induced hydrostatic pressure becomes large enough to balance the osmotic suction tending to cause the water flow (Y. Xu et al. 2014). When distilled water is used in the specimens' fabrication, osmotic suction is always assumed negligible, which is commonly used in literatures (Dao et al. 2011; Delage and Cui 2008; Patil et al. 2017; Rowe 2012).

Effect of suction on earth mechanical behaviour

There are three main techniques to apply and to control suction in various experimental researches on unsaturated soils: (i) axis translation technique, (ii) relative humidity or vapour equilibrium technique, and (iii) osmotic technique. Among them, vapour equilibrium technique is frequently used when dealing with experiments on compacted earth material. In fact, earth is always compacted at its optimum moisture content inside a temporary formwork, thereby producing different construction forms. After the construction, compacted earth can be subject to large changes in relative humidity. Those perpetual changes of environmental conditions induce continuous changes of water content of the earth that impact significantly its mechanical and hydraulic performances. Therefore, applying a vapour equilibrium method on the earth

mechanical test can to a large extent reflect the real working condition over the life cycle of earth structures.

The control of suction by the relative humidity technique is based on the regulation of the relative humidity of the atmosphere surrounding the sample by means of an aqueous solution of a given chemical compound (a product at various concentrations or different saturated saline solutions). According to the relative humidity of the air, water exchanges occurring by vapor transfers between the sample and its surrounding induce a given suction at equilibrium within the sample (Gerard et al. 2015). The relationship between suction at equilibrium inside the soil sample and the relative humidity of the surrounding air is given by Kelvin's law:

$$s = -\frac{\rho_w RT}{M_w}\ln(RH) \tag{2-3}$$

In the above relation, s is theoretically the total suction (sum of matric and osmotic components), R is the constant of perfect gases (R = 8.3143 J/mol/K), T is the temperature in Kelvin, M_w is the molar mass of water (M_w = 0.018 kg/mol), $\rho_w$is the bulk density of water (ρ_w = 1000 kg/m^3).

The influence of suction (relative humidity) on the mechanical behaviour (e.g. strength stiffness) of compacted earth has been largely studied (Q.-B. Bui et al. 2014; Gerard et al. 2015; Jaquin et al. 2009). Bruno et al. (2017) further explored this aspect with reference to hyper-compacted raw earth by testing five sets of three cylindrical samples compacted to the three pressure levels of 25, 50 and 100 MPa, respectively, at the corresponding optimum water contents. After compaction, each set of samples was equalized at different relative humidities of 95, 77, 62, 44 and 25% under a constant temperature of 25 °C. After equilibrium, unconfined compression tests were carried out on these specimens to determine the failure strength, as well as the stiffness through five cycles of loading–unloading at the initial stage. Results (shown in Figure 2.11) indicate that both unconfined compression strength and Young's modulus increase with growing suction. It is also observed that these two mechanical indexes increase remarkably at lower suction range and tend to a constant at higher suction range. This is logical and explainable because at high suction regime, water content is mainly composed of intra-aggregate porosity and adsorbed water, which is sometimes thought to have little influence on the mechanical behaviour.

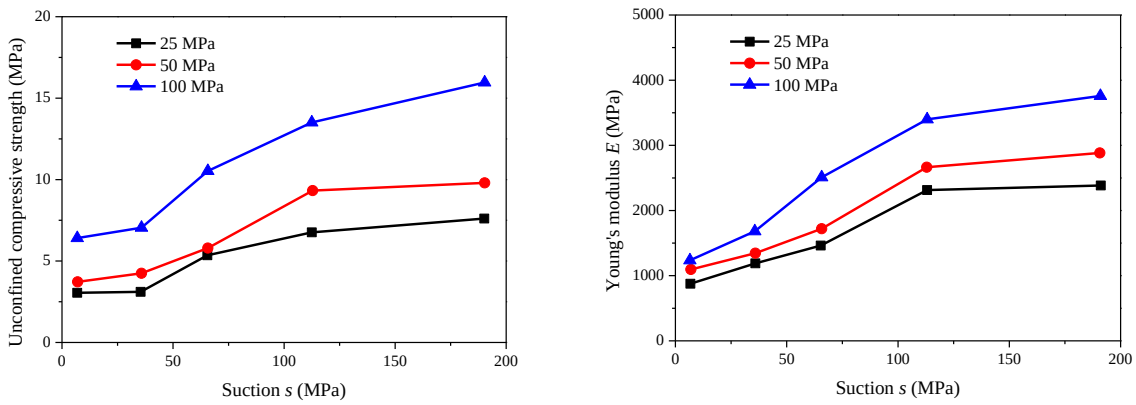

Figure 2.11 Variation of strength and Young's modulus with suction (relative humidity) (Modified after Bruno et al. (2017))

Another recent study by Champiré et al. (2016) confirmed the above results. Firstly, cylindrical samples with a diameter of 64.4 mm and a length of 140 mm were cored from CEBs (compacted earth blocks) which were fabricated by three types of raw earth materials, named STR, CRA and ALX respectively. Their characteristics are described in Table 2.2.

Table 2.2 Summarization of characteristic for the selected earth (Champiré et al. 2016)

	STR	CRA	ALX
Liquid limit (W_l)	24%	29%	20%
Plastic limit (W_p)	18%	16%	16%
Plasticity index (I_p)	7%	14%	4%
Blue value (MB)	1.0	2.7	0.8
Main clay minerals	Illite + Chlorite	Illite + Kaolinite	Illite + Vermiculite

After fabrication, samples were cured at three different relative humidities (23%, 75%, and 97% at 23°C), corresponding to three different suctions. Two types of mechanical loadings were applied at constant relative humidity. The first loading type is a classical unconfined compression tests: loading is applied at constant speed until failure. After measuring the maximum deviator stress at failure for one particular specimen, noted f_c in the following sections, the second loading type consisting of loading–unloading cycles at prescribed stress levels, respectively 20%, 40%, 60% and finally 80% of f_c was conducted with two other specimens prepared under identical conditions as the first one. Young's modulus E and the irreversible plastic strain ε_{res}, (hereafter named as the residual strain) are therefore deduced from these cycles. The results presented in Figure 2.12 confirmed the above results in (Bruno et al. 2017) and showed that both strength and stiffness increase with suction growing (decreasing relative humidity). In addition, the authors also observed a degradation of the secant Young's modulus and an accumulation of residual strain induced by the increasing applied stress (from 20% to 80% of f_c).

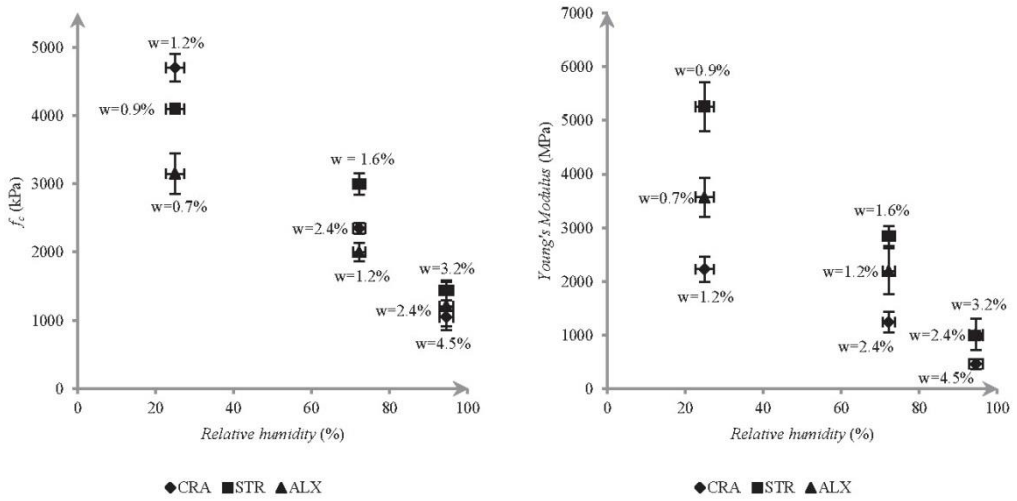

Figure 2.12 Variation of strength and Young's modulus with suction (relative humidity) (Champiré et al. 2016)

The same loading method is adopted by Xu et al. (2017) for triaxial tests on compacted earth (named CRA), at two confining pressures (100 kPa and 600 kPa) and two temperatures (23°C and 30°C). The results (see Table 2.3) in different confining and thermal conditions are also in consistent with that observed from (Bruno et al. 2017; Champiré et al. 2016): both strength and stiffness increase with suction increasing. The authors again verified the degradation of stiffness with the rise of applied stress, as illustrated in Figure 2.13.

Table 2.3 Failure strength f_c (MPa) at different test conditions for earth CRA (Xu et al. 2017)

	RH 23%		RH 75%		RH 97%	
	100 kPa	600 kPa	100 kPa	600 kPa	100 kPa	600 kPa
30 °C	6,6	9,2	4,3	6,2	3,0	4,7
23 °C	6,8		4,1		2,8	

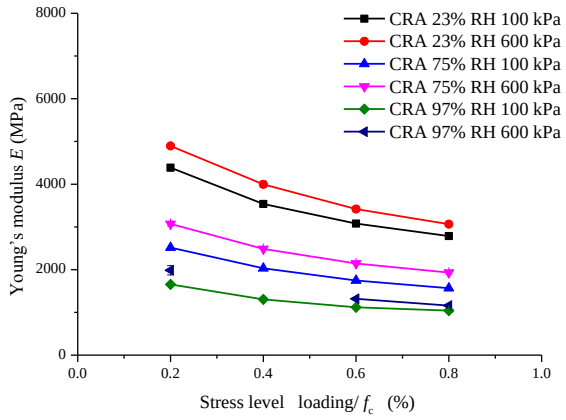

Figure 2.13 Evolution of Young's modulus *E* versus stress level at different relative humidities and confining pressure (Xu et al. 2017)

2.2 Modelling development of earthen materials

In order to study the behaviour of unsaturated earthen materials, a series of extensive laboratory tests were carried out by several researchers. But few research concentrate on developing earth modelling, which is quite helpful to estimate safety factors against failure and to optimize design.

In addition, existing unsaturated soil constitutive models are not applicable to earth constructions. One of the most outstanding problems concerns the choice of effective stress parameter which weighs the contribution of suction on the total stress. The construction of constitutive models for unsaturated soils usually starts by combining stress variables together to form a single effective stress. For this purpose, much research on unsaturated soils has been devoted to the formulation of effective stress (Nikooee et al. 2012; Nuth and Laloui 2008). The most widespread definition is called Bishop effective stress (Bishop 1959):

$$\sigma'_{ij} = (\sigma_{ij} - u_a\delta_{ij}) + \chi(u_a - u_w)\delta_{ij} \tag{2-4}$$

where σ_{ij} is the total stress tensor, u_a is the pore air pressure, s is the difference between pore air and pore water pressure $(u_a - u_w)$, referred as matric suction, δ_{ij} is the second order identity tensor, χ is defined as the effective stress parameter and could be a function of suction , saturation etc.

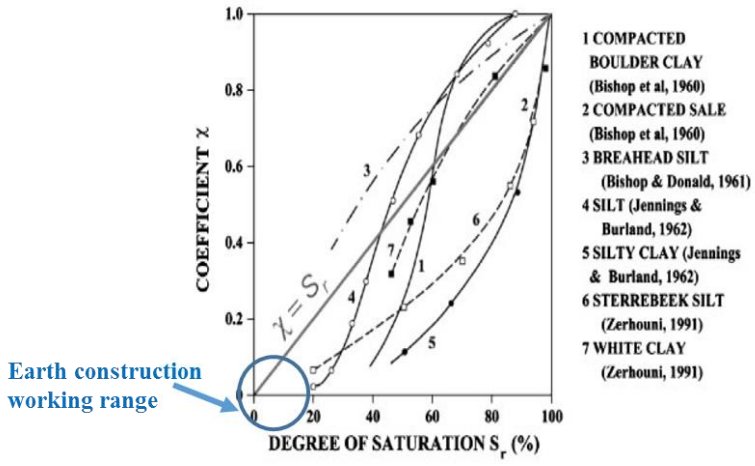

Figure 2.14 Evolution of effective stress parameter with degree of saturation (Modified after Nuth and Laloui (2008))

Various functional forms for the effective stress parameter have been proposed in the literature. Most of them are eastablished based on inter-aggregate porosity regime with suctions ranging from 0 kPa to 10 MPa. Compared to cases investigated in classical unsaturated soil mechanics, the water content of an unstabilized earth construction subject to atmospheric conditions is

generally much lower (1–2%), which corresponds to a much higher suction range (10-200 MPa). There is hardly any study of effective stress parameter χ in such a dry range, as illustrated in Figure 2.14. Moreover, a progressive but non-negligible degradation of Young's modulus E with increasing stress level were observed in recent experimental study (Champiré et al. 2016; Xu et al. 2017). This stiffness reduction is conjectured to be a consequence of damage induced by initiation and development of micro-cracks.

All the factors mentioned above motivate the development of a new constitutive model which can simulate the suction-dependent poroplastic behaviour of earthen materials while also accounting for damage effects. In the following section, we will recall some important concepts of damage models for useful future references, followed by those of elastoplasicity and the coupling between the two phenomena.

2.2.1 Damage models

When engineering materials are subjected to unfavorable conditions such as cold and hot working processes, temperature variation, chemical action, radiation, mechanical loading or environmental conditions, microscopic defects and cracks may develop. It is generally accepted that a crack is induced or formed by nucleation of micro-cavities that are enclosed in a region of discontinuities or defects (Zhang and Cai 2010). The distributed defects in materials are termed as damage, which is responsible not only for the crack initiation and the final fracture, but also for the induced deterioration of mechanical properties, such as a reduction in strength, rigidity, toughness, stability, life span (Lemaitre 2012). These phenomena are generally investigated by means of a damage model, which can represent variations of material properties and processes of material failure due to damage initiation, growth and propagation. A damage model generally possesses the following features (Zhang and Cai 2010):

(1) An appropriate damage variable to represent the macroscopic effects of microscopic cracks of materials. It can be a scalar function under the assumption of isotropic damage. In more complicated case, it is a tensor, and the behaviour is anisotropic.

(2) A damage kinetic equation (damage growth equation) to describe damage growth. It is written in terms of stress and/or strain in order to simulate the effects of growth of macro-cracks.

(3) A constitutive equation incorporating the damage variable to describe the mechanical behavior of the damaged material. Depending on the type of undamaged behaviour, the

damage model can be classified as: isotropic elastic damage model, elastoplastic damage model (isotropic and anisotropic), and visco- elastoplastic damage model.

One of the most famous isotropic damage models is called Mazar's model, proposed by (Mazars 1986) specially for concrete. The relationship between stress and strain in Mazar's model is given by the following equation based on the form of a generalized Hooke's law:

$$\boldsymbol{\sigma} = (1 - D)\mathbb{E}\boldsymbol{\varepsilon}^{\boldsymbol{e}} \tag{2-5}$$

where $\mathbb{E}$ is the Hooke matrix, D is the damage variable, and $\boldsymbol{\varepsilon}^{\boldsymbol{e}}$ is the elastic strain. The progression of damage is distinguished by the sign of solicitation and is modeled by two scalar internal variables in tensile (D_t) and compressive damage (D_c).

$$D = \alpha_t D_t + \alpha_c D_c \tag{2-6}$$

where α_t and α_c are the weight coefficients depend on the principal strains in tension and compression.

Bui et al. (2014) recently used Mazar's model to simulate the behavior of rammed earth wallets under a compression loading. Figure 2.15(a) shows the comparison of the load-displacements between experiments and the simulation. Results indicate that Mazar's model was able to retrieve the initial stiffness and the level of the maximum response of the stress-strain curve that was found throughout experiments. However, the pre-peak and post-peak behaviour was not simulated correctly.

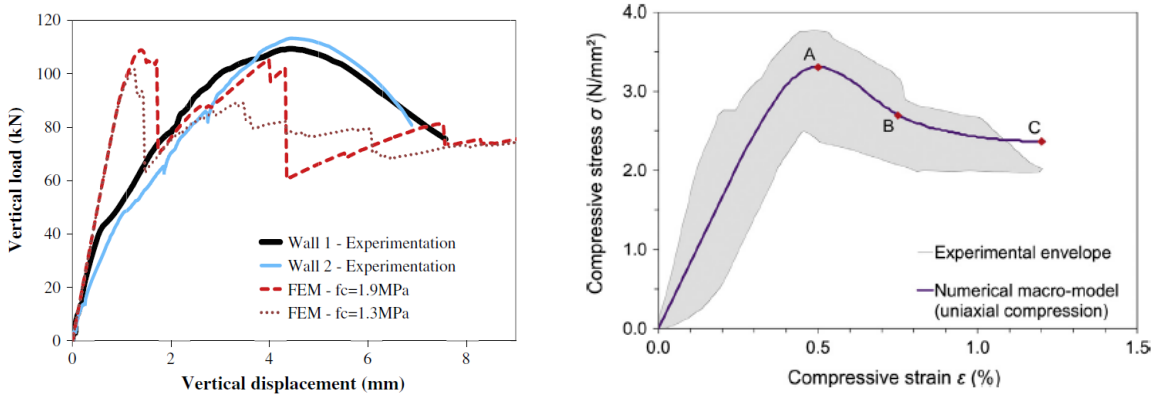

(a) rammed earth wallet using Mazars' model (T. T. Bui et al. 2014))

(b) earth block masonry using TSRCM model (Miccoli et al. 2015)

Figure 2.15 Comparison between experiments and simulations of uniaxial compression test

The Total Strain Rotating Crack Model (TSRCM) is another constitutive model used for earth problems (rammed earth or earth block masonry) modelling (Miccoli et al. 2014, 2015,2016). TSRCM belongs to the class of isotropic elastic-damage models since it involves the

degradation of the elastic properties like in Mazar's model. In the TSRCM, the degradation of the material due to cracking and crushing is monitored by six internal damage variables. Figure 2.15 (b) presents a comparison between experiments of uniaxial compression test on earth block masonry and its corresponding simulations using TSRCM model (Miccoli et al. 2015). Similar to the results in Bui et al. (2014), this model can roughly capture the initial stiffness and peak strength, but the smooth stress–strain behaviour usually observed in the experiments is not reproduced in the simulation.

2.2.2 Elastoplasticity model

The second approach on constitutive modeling belongs to the framework of elastoplasticity. The basic assumption of plasticity is that the increment of the total deformation is decomposed into an elastic and a plastic part as:

$$\boldsymbol{\varepsilon} = \boldsymbol{\varepsilon}^{e} + \boldsymbol{\varepsilon}^{p} \tag{2-7}$$

There are plenty of plasticity models suitable for geomaterials, such as model with Mohr-Coulomb theory, model with Drucker-Prager theory and Cam-Clay model. According to Vermeer and De Borst (1984): model with Drucker-Prager theory is suitable for the case of soft clay with a low friction angle. In other cases, model with Mohr-Coulomb theory is generally used as a first approach to model possible irreversible strains in geotechnical boundary value problems. While Cam-Clay model is based on critical state and suitable for normal or slightly over-consolidated soil.

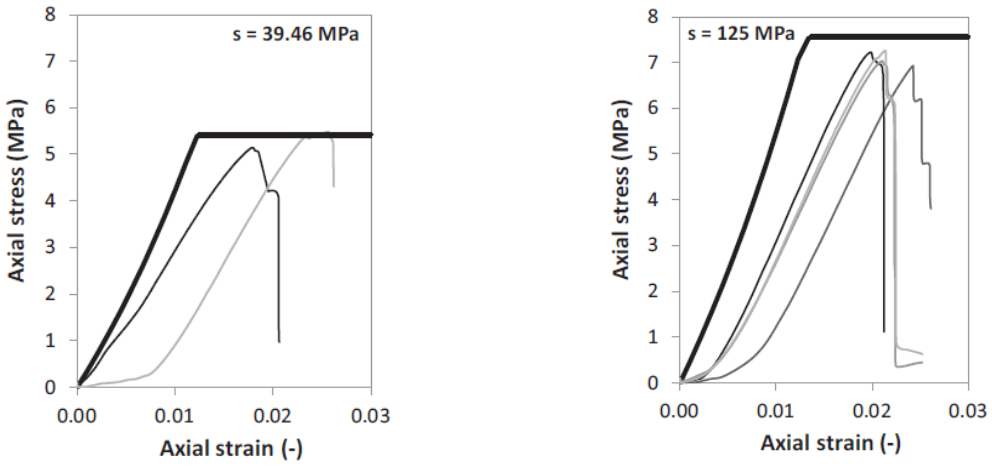

Figure 2.16 Comparison between experimental results and model predictions using a non-linear elastic perfectly plastic model (Gerard et al.2015)

Gerard et al.(2015) proposed a hydro-mechanical model, in order to simulate the unconfined compression tests results for unstabilised rammed earth at different controlled suctions. The

elastic component of the strain is governed by a nonlinear hypoelastic law while the plasticity is based on the Drucker-Prager failure criteria. The numerical results in Figure 2.16 indicates that the non-linear elastic perfectly plastic model is able to reproduce the effect of suction on stiffness and ultimate strength. However, the sharp transition appearing in the simulation results is not consistent with experimental observations. In fact, the main drawback of classic elastoplastic models is their erroneous prediction of a sharp transition at yield from elastic to elastic-plastic behaviour (jump of apparent stiffness), as well as their difficulty to reproduce realistic volumetric behavior (typically a smooth transition from contractancy to dilatancy).

Models developed using the Bounding Surface Plasticity (BSP) theory can overcome these limitations. This theory, firstly proposed by Mroz (1967) and Dafalias (1986) to simulate metal behaviors, was successively applied by Bardet (1986) on saturated sands and later on followed by Gajo and Wood (2001) as well as by Yu and Khong (2003). BSP theory was later extended to partially saturated materials in order to describe suction effects (Morvan et al.2010; Russell and Khalili 2006; Wong et al.2010). In addition, BSP theory is also applied on geomaterials other than soils due to its versatility, such as rockfills and clay-fouled ballast (Kan and Taiebat 2014; Tennakoon et al. 2015).

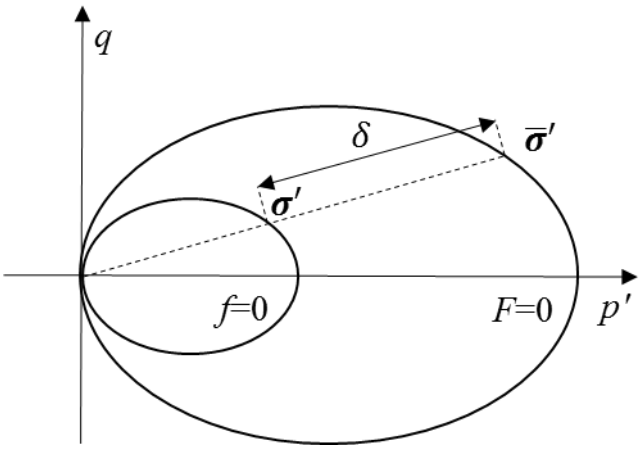

Figure 2.17 Schematic representation of bounding surface plasticity and the radial mapping method

In BSP model, two surfaces are introduced generally (see in Figure 2.17): a Loading Surface (LS) $f = 0$ containing the current stress point $\boldsymbol{\sigma}'$ and a bounding surface (BS) $F = 0$ with an image stress point $\overline{\boldsymbol{\sigma}}'$. The central idea of BSP is that the plastic strain rate, which governs the rate of hardening hence the movement of the BS, depends on the distance separating the current stress point and an image stress point on the BS. The plastic strain rate is designed to be small at small distances and increases when this distance decreases. A "radial mapping" is frequently used to define this image stress point. It consists of extrapolating the position vector linking the

origin to the current stress until it intersects the image stress on the Bounding Surface as illustrated in Figure 2.17.

2.2.3 Coupling between damage and elastoplasticity

In parallel, there have been extensive studies on the development of coupled elastoplastic damage models (Chiarelli et al. 2003; Dragon and Mroz 1979; Hayakawa and Murakami 1997; Ju 1989; Mazars 1986). However, most of them are devoted to modeling dry materials without considering coupled hydromechanical interactions, not to mention the capillarity effects due to partial saturation. In recent years, several researchers have attempted to couple damage with hydromechanical interactions. For instance, a coupled poro-elastoplastic damage model is proposed by Shao et al. (2006) and extended to partially saturated conditions in order to study coupled hydromechanical damageable behaviours in drying–wetting processes. Zhang et al. (2013) developed a unified elastic–viscoplastic damage model to describe long-term hydromechanical behavior of argillites under unsaturated condition. Bui et al. (2016) presented a new constitutive model accounting simultaneously for the impact of damage on hydraulic and mechanical properties of unsaturated poroplastic geomaterials, by means of the thermodynamic framework for partially saturated media.

Chapter 3
Characterisation of local earthen materials

3.1 Overview of crude earthen materials

Earthen material has been widely used in the Rhone-Alpes region (South-East of France) where earth constructions account for approximate 40% of the rural architectural heritage (Collectif FFB 2012). A lot of these structures date to more than 300 years ago and many are still inhabited. Indeed, the still existing earth heritage demonstrates the longevity of these constructions and therefore the suitability of local earth used for construction (Hamard 2017b). In modern constructions, apart from the earth heritage history, a series of geotechnical tests are also carried out on earthen specimens in the laboratory, thereby assessing their applicability on the construction.

In this study, four kinds of crude earth were selected from Rhone-Alpes region, respectively from the village of Saint Trivier de Courtes, Cras sur Reyssouze, Saint-Antoine-l'Abbaye and Limonest, hereafter named STR, CRA, STA and Lim for simplicity. Their locations in the map are shown in Figure 3.1.

Figure 3.1 Location of the crude eath in this study

There are many existing earth buildings in these villages, as shown in Figure 3.2. Accordingly, some of them need renovation works and some new earth construction activities occur. The main purpose of choosing such crude earth in this study is to study their physical and mechanical characteristics, thereby pushing forward the application of raw earth in modern construction.

STR

CRA

STA

Lim

Figure 3.2 Existing earth buildings in four villages from Rhone-Alpes region

3.2 Basic properties of crude earthen materials

3.2.1 Particle size distribution

In the laboratory, the grain size distribution of earthen material is always regarded as an important property when assessing their suitability for construction. In terms of making representative earthen samples in the laboratory, the material grain size should be considered carefully thereby fulfilling the requirement of dimension scale and homogeneity of specimens at the considered scale. Considering that the specimens used in this study belongs to a micro-mechanical scale (Q.-B. Bui et al. 2008), the raw earth material, which directly came from the construction sites, was crushed into small particles, then passed 2 mm sieve to obtain homogenous state. Particle size distribution tests will be carried out on the remaining soil passing 2 mm sieve through the wet sieving method and sedimentation test (French Standard NF P 94-056 1996; French Standard NF P 94-057 1992).

Wet sieving method

Wet sieving method is adopted for removing clay and silt fraction (<0.08 mm) from gravel and sand, later using various sieves, gravel and sand quantities is calculated. Clay and silt fractions are obtained through sedimentation test using hydrometer. The main procedure is expressed as following:

- Two piece of earth samples are used in this test with equal amount (m_{wet}), one is dried in oven at 100-110°C to identify the initial water contents w_{int}, while another piece is used for the wet sieving. In this case, the test is carried out at the initial water content, which aims to avoid any disadvantages resulted from drying before sieving. The dry mass used in the test can be calculated through the following equation.

$$m_{dry} = \frac{m_{wet}}{1 + w_{int}} \tag{3-1}$$

- Soaking the wet sample in advance (2 to 24 hours), then the 0.08 mm sieve is used to separate the retained fraction (coarse particles) and passing fraction (fine particles).

- Both of them are dried in oven at 100-110°c for 48 hours, until the difference between two successive readings of dry mass is negligible with an accuracy of 0.01g, recording the dry mass separately, named m_R and m_P. The material loss is checked after wet sieving and it should fulfill the following precision:

$$\frac{m_{dry} - (m_R + m_P)}{m_{dry}} \times 100 \leq 2\% \tag{3-2}$$

- The retained fraction m_R is then allowed to pass through the sieves arranged in descending order from the largest sieve size of 2 mm to 0.08 mm (Figure 3.3).
- After sieving process, material retained on each sieve is weighed with precision to 0.01g and the combined retained fractions are recorded as R_i. The percentage φ_{wet} of the corresponding passing fractions are calculated through the following equation, which will be illustrated in the particle size distribution curve.

$$\varphi_{wet} = 100 - \frac{R_i}{m_{dry}} \times 100 \tag{3-3}$$

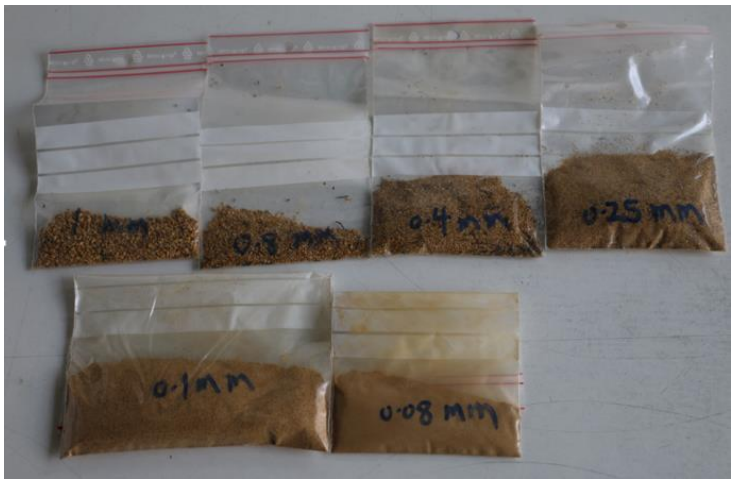

Figure 3.3 Experimental sieves and the retained fractions in wet sieving method

Sedimentation test

Sedimentation analysis is a test which complements particle size distribution test by wet sieving method. It is adopted to calculate the percentage of finer soil particles (<0.08 mm) which is not possible to use sieves. By assuming all fines to be spherical, they are placed in homogenous suspension in a standing liquid and fall at different speed according to their diameters. As a result, the density of the initial homogeneous mixture will increase from the top to the bottom as time passes. By measuring times and densities using hydrometer (illustrated in Figure 3.4), a spread of the diameters of the fine particles could be calculated through Stokes' law.

- Fine particles m_P, passing through the 0.08 mm sieve mentioned in last section, is used for the sedimentation test.
- Using laboratory pestle and mortar the dry fine particles sufficiently until obtaining fine powder, 80g of which is soaked in solution of 300 cm^3 of distilled water and 60 cm^3 of dispersing agent for about 12-15 hours (overnight).
- The solution is then mechanically stirred for about 3 minutes before transferring it to a 2L graduated cylinder half filled with distilled water. Fill up the rest of 2L graduated cylinder with distilled water, and use another 2L graduated cylinder filled with distilled water and same quantity of dispersing agent for hydrometer reading correction
- Shake graduated cylinder with the solution, such that the solution is uniformly suspended (distributed), immediately insert the clean hydrometer into solution and note down the hydrometer reading value *R* with respect to time intervals of 30 seconds, 1, 2, 5, 10, 20, 40, 80, 240 minutes and finally 24 hours, all these times being counted from the start of the test.

- In order to correct the recorded values, accounting for the influence of temperature, meniscus and dispersing agent, another value *C* is read from the hydrometer placed in the control cylinder.
- The percentage of fine particles φ_{sed} is then calculated using the following formula:

$$\varphi_{sed}(\%) = \frac{\mathrm{v}}{\mathrm{m}} \times \frac{\rho_s}{\rho_s - 1} \times \frac{R + C}{10} \tag{3-4}$$

where v is the volume of suspension, 2000 cm^3; m is the mass of earth sample used in sedimentation test, 80 g; ρ_s is the soil grain density 2.7 g/cm^3; *R* is reading value from testing hydrometer, while *C* is correction reading value from the hydrometer placed in the control cylinder, both of them represent the density of suspension at time t, in mg/cm^3.

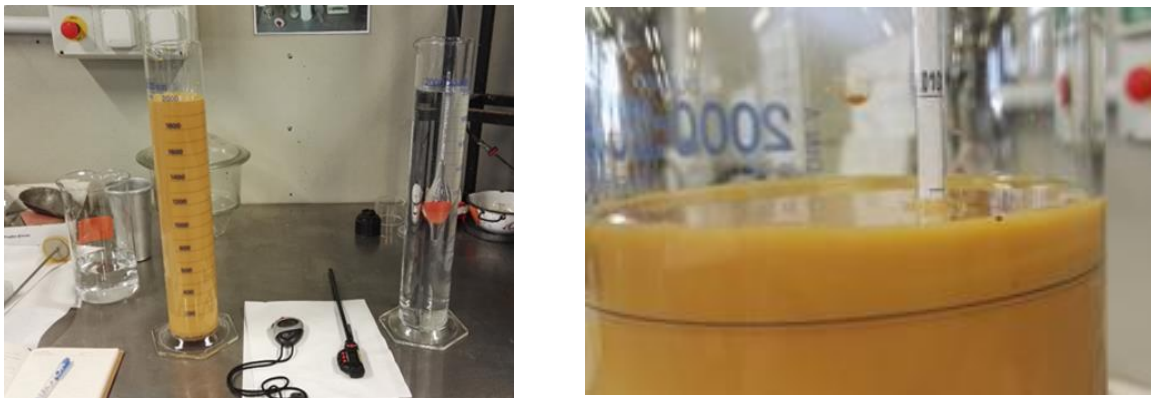

Figure 3.4 Experimental procedure and apparatus for sedimentation test

Discussion about the particle size distribution of four kinds of crude earth

By combining the results from wet sieving method and sedimentation test, particle size distribution curves for STR, CRA, STA and Lim are presented in Figure 3.5 and Table 3.1.

Table 3.1 Grain Size of soils considered in this study

Grains		STR(%)		CRA(%)		STA(%)		Lim(%)	
Sand (0.05-2 mm)	Coarse (0.5-2mm)	3	**40**	8	**57**	8	**40**	1	**29**
	Medium (0.25-0.5mm)	13		18		10		2	
	Fine (0.05-0.25mm)	24		31		22		26	
Silt (0.002-0.05mm)	Coarse (0.02-0.05mm)	20	**45**	9	**26**	7	**31**	18	**36**
	Fine (0.002-0.02 mm)	25		17		24		18	
Clay (<0.002 mm)	(<0.002 mm)		**15**		**17**		**29**		**35**

Inspection of Table 3.1 illustrates among these four kinds of crude earthen materials, Lim possesses the highest clay content (<0.002 mm) with value equal to 35%, followed by STA with clay content of 29%; finally, STR and CRA have almost the same clay content which is about half of that in Lim and STA.

Generally, an earth material suitable for construction has a great dispersion but should contain fine gravel and sand with cohesive soils (silt and clay) to act as a binder between the grains (Maniatidis and Walker 2003). Much work has already been done to give the recommended maximum and minimum grain size distribution of earthen materials (Jiménez Delgado and Guerrero 2007; Maniatidis and Walker 2003; Peter Walker et al. 2005).

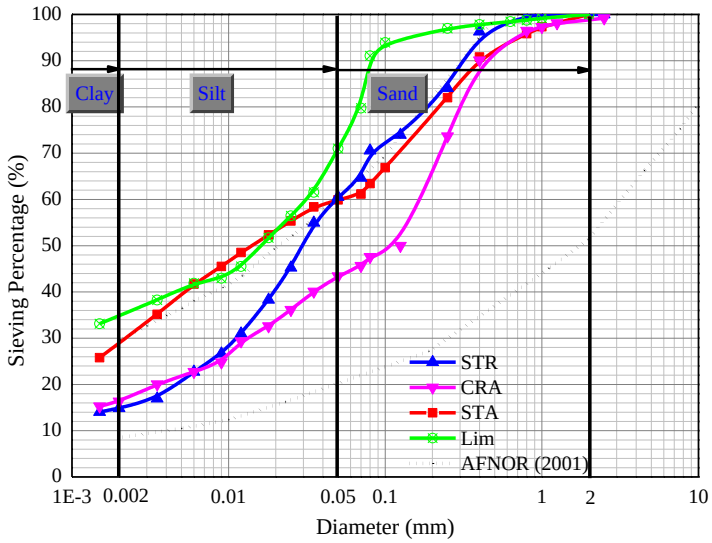

Figure 3.5 Particle Size Distribution of four crude earthen materials and maximum and minimum grain size distribution of soil recommended by (AFNOR 2001).

Figure 3.5 illustrates the lower and upper limits of the particle size distribution as prescribed by the guideline for the manufacture of compressed earth bricks (AFNOR 2001). Comparison with the particle size distribution curves of other four kinds of earthen materials indicates STR and CRA roughly lie in the recommended region. While STA lies close to the finer limit (upper limit) of the admissible region, which means they possess more fine particles (clay and content) than sands. As for Lim, the dispersion in fine particles is quite similar to that of STA, but an absence of coarse sand makes it lying partially outside the region. It should be noticed the same circumstance occurs in the study of (NABOUCH 2016; Narayanaswamy 2017) when they selected their earth named “Dagneux” . This soil possesses 85% of fine particles (silt and clay) and 15% of sand respectively, which is quite similar with that of Lim in our study.

In fact, the recommended region should not be the only criterion when selecting earthen materials for construction, because the great variability of possible soils and techniques are not taken into account. Besides, it is worth noticing that the earth used in this study comes from an existing construction and it is essential to understand the behavior of soil already used in existing structures without any discard to the sustainable aspect of using available local earth (J. C. Morel et al. 2001).

3.2.2 Plasticity property

In crude earth, the fine particles act as a binder of larger grains and must therefore satisfy some specific plasticity requirements to ensure adequate bonding. The Atterberg limits are conventional constants evaluating the plasticity and marking the thresholds between:

- Liquid limit W_L: It indicates the water content of a soil at the state of transition from a liquid state to a plastic state.
- Plastic limit W_P: It indicates the water content of a soil at the state of transition from a plastic state to a solid state.

The difference of plastic limit and liquid limit defines the range of the plastic zone and is named plastic index I_P:

$$I_P = W_L - W_P \tag{3-5}$$

In this study, the test is conducted on the fine particles (<0.4 mm) in agreement with the norm of (French Standard NF P 94-051 1993). More exactly: The liquid limit is defined as the water content at which the two halves of a plaster of soil, placed in a cup and divided into two parts by a groove, come into contact a fixed length as the result of a fixed number of blows (25) delivered to the cup. This is done using the Casagrande apparatus as shown in Figure 3.6. While the plastic limit is defined as the water content at which it is possible to form 3 mm diameter rolls without cracking.

Figure 3.6 Casagrande apparatus and 3 mm diameter rolls without cracking

Liquid limit, plastic limit and plasticity index have been determined and reported in Table 3.2. In addition, the evolution of plastic index I_P with clay content are presented in Figure 3.7. It indicates the plastic index I_P roughly increases linearly with the rise of clay mass content for the four kinds of earth studied. This observation indicates clearly that the clay content exerts a non-negligible influence on the earth behaviour, which motivates the research goal in this thesis.

Table 3.2 Plasticity properties of four crude earthen materials

	STR	CRA	STA	Lim
Liquid limit W_L (%)	24	29	52	43
Plastic limit W_P (%)	18	16	31	21
Plasticity index I_P (%)	7	14	21	22

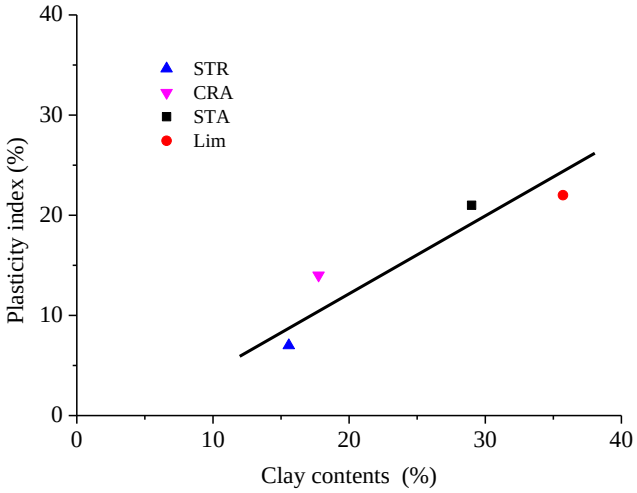

Figure 3.7 Plastic index I_P versus clay content

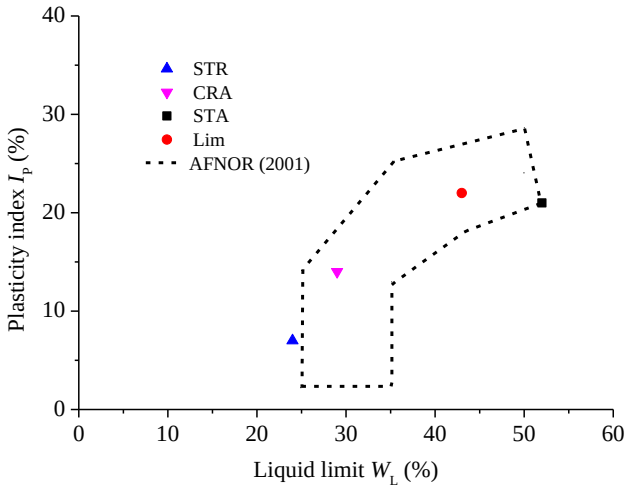

Figure 3.8 Plastic I_P against liquid limit and the recommended region proposed by (AFNOR 2001)

Figure 3.8 presents the confrontation between the values of plastic index and liquid limit, as well as the recommended region proposed by the norm of (AFNOR 2001). It is obvious that CRA and Lim fall well within the admissible region while STR and STA lie on the boundary of this admissible region. Like the recommended upper and lower particle size distribution mentioned in the last section, such kind of admissible region provides a preliminary identification and evaluation on the earthen materials. A more complete characterisation with a more refined consideration of the variety and complexities of earth materials (e.g. specific information on pedological or geological origin for earthen materials) should be taken into account when assessing the suitability as a construction material (Hamard 2017).

3.2.3 Methylene blue value

Object and principle of blue value test

The blue value test quantifies the ionic adsorption capacity of a soil by measuring the quantity of methylene blue necessary to cover the total (external and internal) surface of the clay particles contained in the soil. This testing technique works on the basis of the chemical reactions triggered by an excess of negative electric charges in the clay particles and the ionic exchange phenomena taking place between the easily exchangeable cations of the clay and the methylene blue cations released by methylene blue during its decomposition in water (Chiappone et al. 2004). The particles having the largest specific surface and the greatest negative charge are those of clay minerals, which therefore are the ones which possess the largest number of ions that can be most readily "exchanged." Hence, this test is particularly suitable for studying clays or clay fractions of a soil. In this study, clay and silt fraction (<0.08 mm) is taken as testing sample and the standard (French Standard NF P 94-068 1998) is adopted.

Procedure and results for the methylene blue test

- 30 g of dry fine particles (clay and silt) passing through 0.08 mm sieve are placed in a container with 500 mL of distilled water, dispersed in the water, and maintained in suspension by means of a stirrer.
- With a burette, unit doses (5 mL) of the methylene blue solution, with a concentration of 10 g/L, are added to the suspension.

- After adding each unit dose, a small quantity of the suspension is collected with a rod and a small drop is made to fall onto standard filter paper; this produces a dark blue stain, surrounded by a colourless wet area (Figs 3.9 and Figs 3.10).
- Further unit doses of the solution are then added and more drops are deposited on the filter paper until a light blue halo is seen to form inside the wet area and around the blue stain. This reflects the presence of an excess quantity of methylene blue that is no longer adsorbed by the clay mineral and remains in suspension.
- At this point, no more methylene blue is added and the suspension is checked at 1 min intervals to determine the stability of the light blue halo; if the halo persists after 5 mins, a sufficient quantity of methylene blue has been added. Otherwise, the titration process is continued until the halo becomes stable enough.

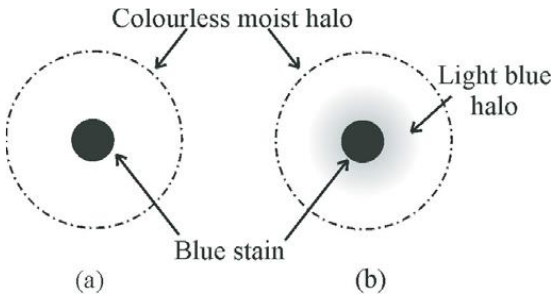

Figure 3.9 Schematic outcome for methylene blue test (a) blue stain surrounded by a colourless wet area; (b) blue stain surrounded by a light blue halo (Chiappone et al. 2004)

Figure 3.10 Experimental procedure and apparatus for methylene blue value test

The index supplied by this testing method is referred to as the blue value of the soil (V_B, in g/100 g) and is given by:

$$V_B = V \times 0.01 \times 100/W \tag{3-6}$$

where V is the volume (in cm^3) of the methylene blue solution used, 0.01 is the concentration (g/cm^3) of the methylene blue solution used, and W is the dry weight (in g) of the specimen.

Because the blue value test is carried out on fine particles (a mixture of clay and silt), V_B does not only reflect the clay content of the sample, but also indicates the activity of clay minerals. Accordingly, the index of activity is defined to purely reveal the activity of clay fraction in soil:

$$A_{CB} = \frac{V_B}{C_B} \tag{3-7}$$

where A_{CB} is the index of activity (in grams of methylene blue in a 100 g clay fraction), V_B is the blue value for the testing sample (in grams of methylene blue per 100 g of dry soil), and C_B is the clay content (<0.002 mm) in the 0-0.08 mm fraction.

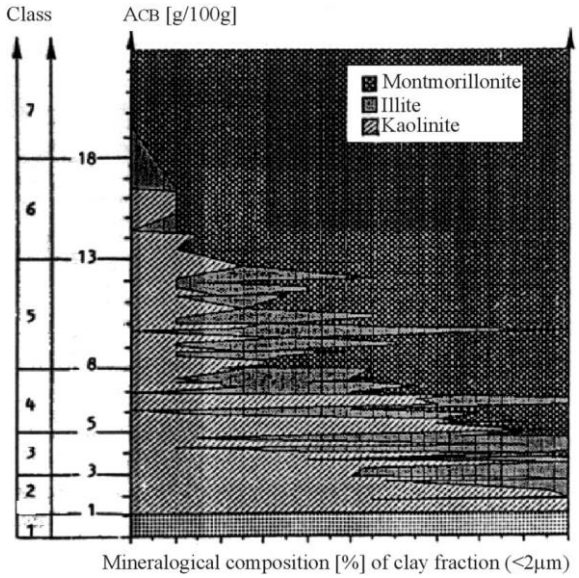

Figure 3.11 Blue activity diagram (Lautrin 1989). Classes as follows: 1. not clayey soil; 2. soil with interactive clay fraction; 3. soil with not much active clay fraction; 4. soil with normal clay fraction; 5. soil with active clay fraction; 6. soil with very active clay fraction; 7. soil with noxious clay fraction.

Table 3.3 Methylene blue value results and an evaluation of clay contained in earth

	STR	CRA	STA	Lim
Clay contents in the 0-0.08 mm fraction (C_B)	22.7 %	31.5 %	45.7 %	38.4 %
Blue value (V_B)	1.0	2.7	1.7	3,0
Index of clay activity (A_{CB})	4.4	8.6	3.7	7.8
Evaluation of clay activity	Class 4 Normal	Class 5 Active	Class 3 Not much active	Class 5 Near active

Lautrin (1989) proposed a classification of soils as a function of their index of activity (Fig 3.11). According to this proposition, the methylene blue value results and an evaluation of clay contained in four kinds of earthen materials are presented in Table 3.3.

Inspection of Table 3.3 shows that the clay minerals contained in CRA possesses the highest activity, and clay in Lim has almost the same activity. In contrary, clay minerals presenting in STR and STA are not very active. It is worth noting that the evaluation of clay minerals is quite consistent with the analysis using XRD (X-ray powder diffraction) by (CHAMPIRE 2017) on STR and CRA. This last study showed the presence of illite and kaolinite in the clay minerals of CRA, by opposition to the presence of illite and chlorite in STR. The more active property of kaolinite than chlorite explains the higher clay activity of CRA compared to STR.

3.3 An exploration of the optimum state based on dynamic compaction (Proctor test) and double static compaction

3.3.1 Motivation of this exploration

There is no doubt Proctor test is commonly used in the laboratory to determine the optimum moisture content and maximum dry density for earthen materials. It is particularly applicable to rammed earth constructions, because both Proctor test and in-situ rammed construction belong to the family of dynamic compaction. In contrary, other kinds of earth construction (e.g. compacted earth blocks (CEB)) are generally produced by compaction of soil under a quasi-static pressure. Obviously, it is not pertinent using the Proctor test in laboratory to estimate the optimum moisture content and maximum dry density of a static field process like CEB. This is because the energy required for static compaction is generally quite different from the energy supplied in a Proctor test, as static compaction and dynamic compaction are two totally different methods. Hence, the optimum water content derived from the Proctor test is possibly not relevant to the static compaction process.

Many researchers have realized this problem, and several studies on the comparison between static compaction and Proctor test have been done in the past few years (Attom 1997; Kenai, Bahar, and Benazzoug 2006; Mesbah, Morel, and Olivier 1999; Olivier and Mesbah 1986; Venkatarama-Reddy and Jagadish 1993).

Olivier and Mesbah (1986) studied the effect of the static compaction pressure on the mechanical properties of the “Isle d’Abeau” earth, using cylindrical samples at different pressure levels (from 1.2 MPa to 10 MPa). The optimum water content and the corresponding maximum dry density for each compaction pressure is determined through testing at different water contents. It was observed that by using higher pressure, compaction curves shift towards

lower values of water content and high values of maximum dry density. Influence of compaction energy on the compressive strength were also presented in this study.

In the study of Kenai, Bahar, and Benazzoug (2006), three different compaction methods (dynamic, static and vibro-static) were carried out on clay sandy soil and their effect on the soil characteristic and performance were also investigated. Static compaction is obtained by applying a static pressure using an universal compression testing machine on stabilized soil put in a cylindrical mould 100 mm diameter and 165 mm height until the desired compaction stress (2.1MPa, 4.2MPa, 6.3MPa and 7.3MPa) was obtained. The only difference between static and vibro-static compaction is the one-minute vibration before being subjected to a static compaction force. A modified Proctor test was used to fulfill the requirements of dynamic compaction, with variation of compaction energy. It was found that the three different methods of compaction used did not affect significantly the optimum dry density of the soil. In addition, mechanical stabilization by dynamic compaction of a local clay sandy soil seems to enhance better the mechanical properties and water resistance of the soil as compared to the static or the vibro-static compaction methods.

In the aforementioned study, the final compaction stress concept was applied to conducting a series of static compaction tests, rather than the widely used iso-energy concept in the Proctor test. Therefore, the following questions motivated an exploration of optimum state applicable to the developed double static compaction mould:

- Is there a series of iso-energy curves in the static compaction?
- If such kind of curves exist, what is the relationship between the iso-energy curves in static compaction and Proctor test (dynamic compaction)?
- Concerning the optimum state derivable from static compaction and Proctor test, which ones are more suitable for the specimen fabrication?

3.3.2 Dynamic compaction (Proctor test)

Introduction

Proctor test is always used in the laboratory to determine the “optimum moisture content” and “maximum dry density”. Optimum Moisture Content (OMC) is the moisture content at which the maximum possible dry density is achieved for a particular compaction energy or compaction

method. The corresponding dry density is called Maximum Dry Density (MDD). Water is added to lubricate the contact surfaces of soil particles and improve the compactability of the soil matrix. It should be noted that increase in water content increases the dry density in most soils up to the OMC (Dry side). Water acts as lubrication. Beyond this level, any further increase in water content (Wet side) will only increase the void space after compaction, thereby reducing the dry density. Hence OMC indicates the boundary between the dry side and wet side.

Generally, Proctor test is divided into normal Proctor test and modified Proctor test according to the compaction energy. In this study, Proctor test is carried out in accordance with the norm of (French Standard NF P 94-093 1999). A pneumatic mechanical compactor is used for the compaction test. As shown in Figure 3.12, it has multiple options to generate standard, modified or even personalized desired compaction energy by changing the weight of drop hammer, the drop height of the hammer, the number of blows per layer and the number of compaction layers. A unified CBR mould is applied in this study with dimension of 152 mm in diameter and 126.6 mm in height without collar. Once the aforementioned parameters are set, the compaction energy can be calculated by the following equation:

$$E = W_h \frac{H}{V} N_B N_L \tag{3-8}$$

where E represents the compaction energy, W_h is weight of hammer, H shows the drop height of the hammer, V is volume of Proctor test specimens and equals to 2296 cm^3 in our study corresponding to CBR mould, N_B defines number of blows per layer and N_L indicates the total compaction layers.

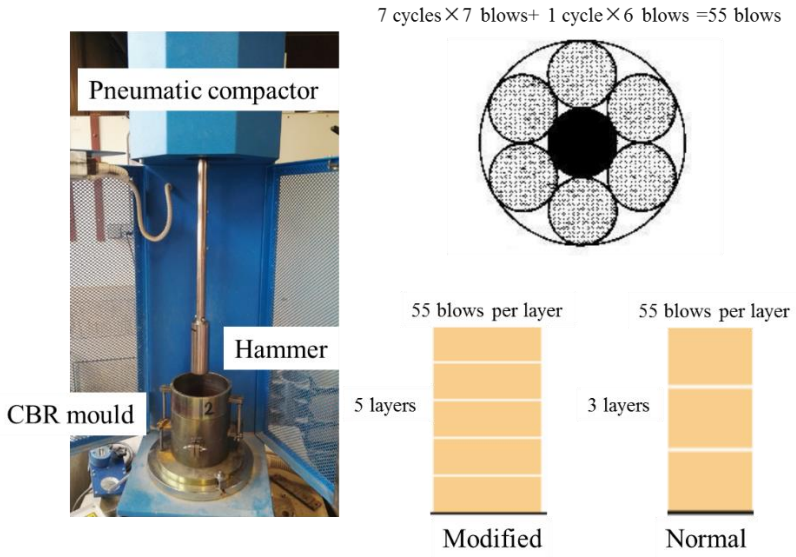

Figure 3.12 Pneumatic compactor system and illustration of normal, modified Proctor test

In this study, three kinds of compaction energy were used during Proctor test: two of them refer to the classic normal and modified Proctor test using CBR mould; in addition, another personalized test with energy between normal and modified Proctor tests was also applied using CBR mould, hereafter named "middle Proctor test". The detailed parameter and calculated energy are presented in Table 3.4.

Table 3.4 Parameters and calculated energy for different kinds of Proctor test using CBR mould

	Type	Weight of hammer (Kg)	Height (cm)	Number of layers	Number of blows per layer	Compaction Energy (KJ/m^3)
Proctor Test	Normal	2.49	30.5	3	55	533
	Middle	4.54	45.7	3	55	1461
	Modified	4.54	45.7	5	55	2435

Test procedure

(1) Approximately 6kg of dry soil passing 2 mm sieve is mixed with 6% of water by weight of the soil as a first trial. The soil is mixed by hand until homogeneous mix of moist soil is achieved.

(2) Mould with base plate is firstly weighed, recorded as W_1 , then they are assembled with upper collar. The inner surfaces of mould, base plate and collar are greased, meanwhile a filter paper is placed on the base plate. These operations aim to facilitate the removal of specimen.

(3) The moist soil is then poured into the CBR mould and the compaction is performed by a pneumatic mechanical compactor shown in Figure 3.12. The detailed parameters (layers, weight of hammer, etc.) are presented in Table 3.4, thereby fulfilling different compaction energy.

(4) When the compaction is finished, the upper collar is then taken away and the compacted sample should protrude from the mould about 1 cm (Figure 3.13). Excess soil is scrapped using a flat knife, then the soil sample and mould (including the base) are weighed as W_2 and the wet density of the soil sample is calculated.

(5) A representative sample from the middle is kept for the determination of water content by measuring the difference in weight of moist soil sample and over dry sample in oven at 100-105°C for 48 hours.

(6) The procedure is repeated with increasing water content of 2 %. The number of trials shall be at least 5 with a few after the decreasing trend of bulk density.

Figure 3.13 Prepared soil with different moisture contents and compacted sample

Optimum state from Proctor test

In this thesis, the modified Proctor tests are carried out on four crude earthen materials: STR, CRA, STA and Lim. To study the influence of compaction energy, three kinds of Proctor test with normal, middle and high compaction energy are conducted on earth STA. The variation of dry density with respect to increase in moisture content of the compacted soil is given in Figure 3.14, in which four crude earth materials are represented. It can be seen that among these four kinds of soils, CRA possesses the highest maximum dry density of 2.08 g/cm^3, followed by STR of 2.03 g/cm^3. Here, it should be noticed that both STR and CRA have almost the same optimum moisture content (approximately 9%). STA has the lowest maximum dry density among the four types of soil. Lim possesses the maximum dry density of 1.95 g/cm^3 and the corresponding optimum moisture content is about 12.5%.

It is worth noting the maximum dry density of STA obtained here is quite consistent with the value reported by (Chabriac 2014). In his study, the dry density of samples, taken from the in-situ construction wall located in St Antoine l'Abbaye, is measured based on the Archimedes principle. An average value of 1.73 g/cm^3 is found that is quite near to our value (1.76 g/cm^3) from modified Proctor test. This observation confirms the fact that the modified Proctor test is one of the most efficient methods in laboratory to determine the maximum dry density and optimum moisture content, which would be relatively useful in assessing the suitability of earth used for construction, especially for rammed earth.

From Figure 3.15, it can be seen that the optimum moisture content of the soil decreases and maximum dry density increases with increasing compaction energy. In addition, it should be

noticed that this increasing trend roughly follows a line of constant saturation degree (S_r = 95%) and all the optimum points approximately lie on this line.

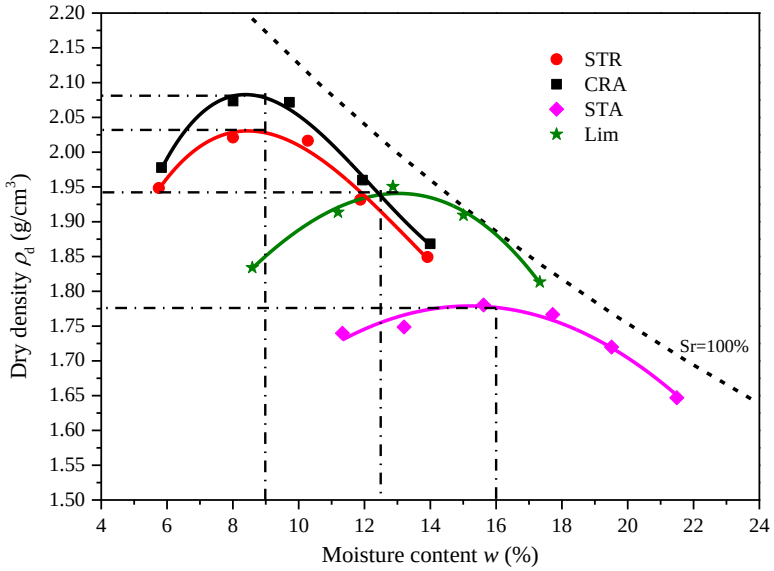

Figure 3.14 Variation of dry density with respect moisture content using modified Proctor test (E=2435 KJ/m^3)

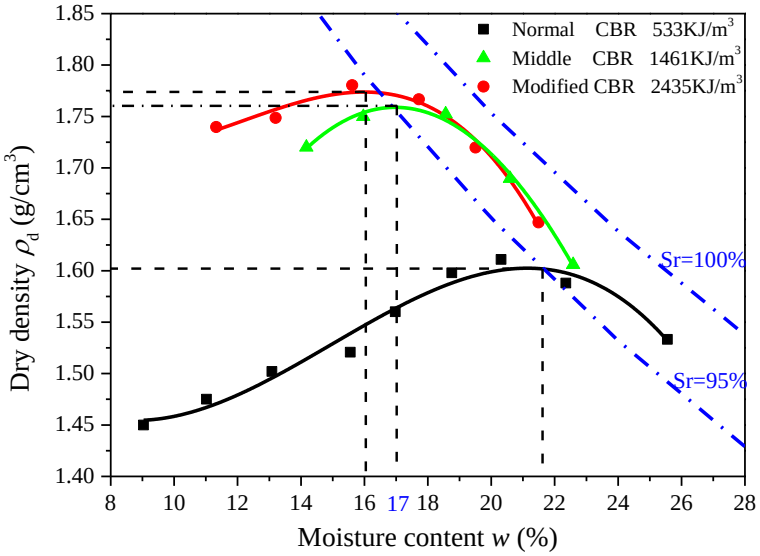

Figure 3.15 Evolution of dry density versus moisture content for STA under three kinds of compacted energy

3.3.3 Double static compaction

Homemade mould description

Due to the stress gradient in the dynamic compaction process, earth specimens manufactured tend to possess higher density at the top of the layer and lower density at the bottom of the layer. This conclusion has been validated by many researchers through different studies on earth

specimens (Quoc Bao Bui and Morel 2009; Narayanaswamy 2017). This inhomogeneity, caused by dynamic compaction, should be avoided for earthen specimens destined to laboratory testing, because dry density has a vital impact on the mechanical behaviour of compacted earth. By comparison, one advantage of static compaction is compacting the soil in one homogeneous layer, contrary to the dynamic compaction, where the soil is compacted into several layers. In view of these considerations, a double static compaction mould was designed and developed by (CHAMPIRE 2017) at ENTPE.

The following requirements are to be considered and satisfied when designing the compaction mould:

(1) The geometry of fabricated specimens should be easily treated during tests.

(2) The mould must be strong enough to bear the high lateral pressures exerted by the compressed soil, thereby guaranteeing the desired size of fabricated specimens.

(3) Utilization of the mould should be simple, allowing the possibility of operation by a single person.

(4) The specimen's density should be as homogenous as possible, thereby reducing its impact on the mechanical behaviour.

To satisfy the above requirements, a double static compaction mould was designed and illustrated in Figure 3.16. Small cylindrical samples with a diameter of 35 mm and a height of 70 mm were selected in this study, in order to facilitate manufacturing and to avoid the presence of corners always appearing in compacted earth blocks, which could result in stress concentration during compaction. Overall, the mould used in this work consists of a hollow stainless steel cylinder with an assembled cover, two piston cylindrical stainless steel pistons acting at the top and bottom of the sample, and two springs. More exactly: the mould material stainless steel guarantees the bearing capacity on the lateral pressures and provides enough abrasion performance occurring between soil particles and the inter wall of mould; the hollow stainless steel cylinder makes sure the size of specimens and the cover with screws fulfils the facility of taking out specimens after compaction; finally, two pistons and two springs placing at the top and bottom imposes a double compaction, which efficiently reduce the effect of friction between the mould and the sample, thus increasing uniformity of stress levels inside the soil and ensuring the homogeneity of specimens.

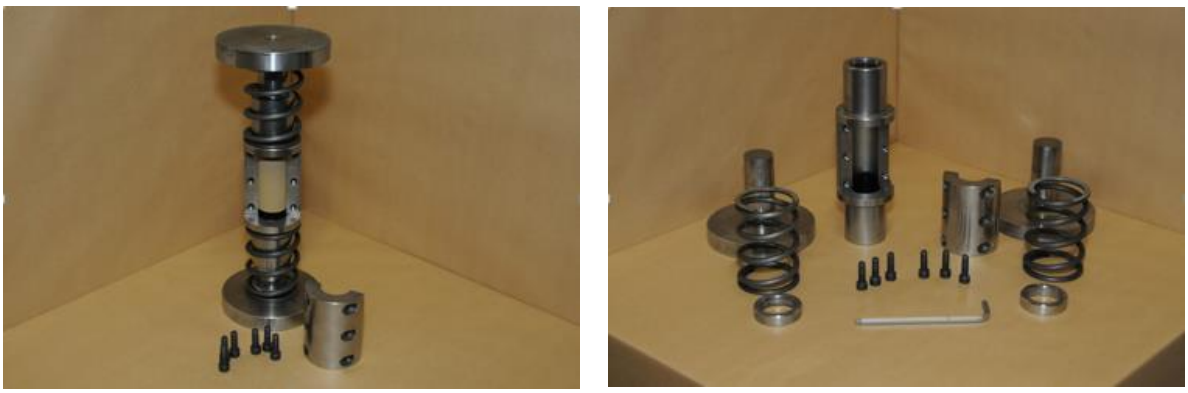

Figure 3.16 A double static compaction mould and its components (CHAMPIRE 2017)

Operational procedures for this mould

The procedure for assembling the mould and compacting the earth is detailed as follows and illustrated in Figure 3.17:

- (a). An assistant device is designed for filling the soil into the mould, it consists of a plastic tube, a wooden piston and a funnel.
- (b). Plastic tube and funnel are properly assembled to their required position, then the moist soil is poured into the tube with the assistance of a funnel, at a constant filling speed in order to ensure homogeneity. The tube is filled by soil particles to a height approximately twice that of the desired specimens (70 mm).
- (c) and (d). The funnel is taken away firstly, then the plastic tube is inserted into the cylindrical mould until reaching the piston at bottom, meanwhile keeping the tube and the mould vertically.
- (e) (f) and (g). The assembled tube and mould are firstly inverted upside-down, the plastic tube is then removed meanwhile keeping the position of the lower piston. The above procedures aims at minimising the soil loss resulted from the removal of plastic tube.
- (h) and (i). The upper piston is emplaced and the entire assembled mould is put under the press. The compaction pressure is applied to the soil specimen at both ends until the target specimen height is attained.
- (j) (k) and (l). When the compaction is terminated, the six screws are discharged and the specimen is taken out from the mould.

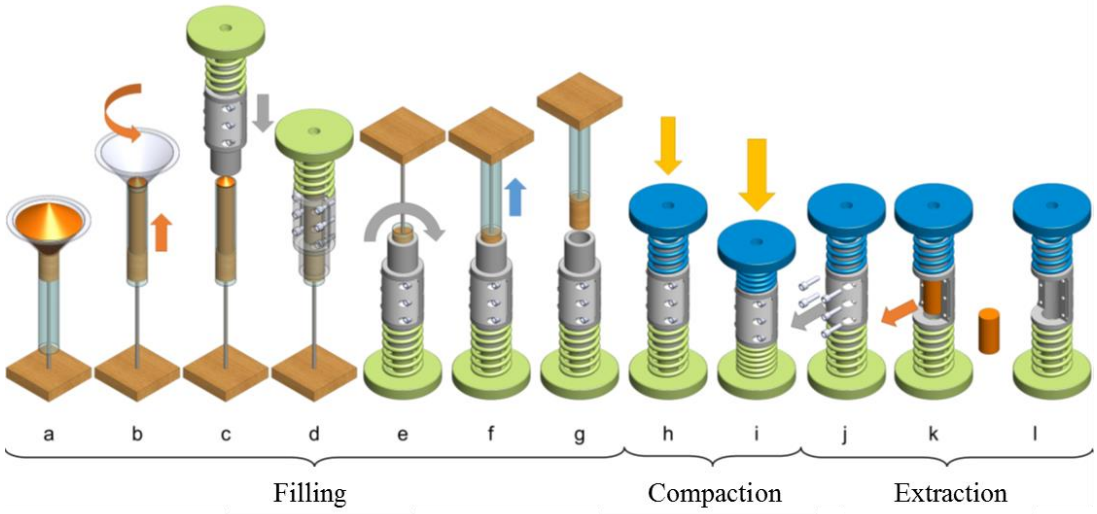

Figure 3.17 Procedure for assembling the mould and compacting earth samples (CHAMPIRE 2017)

A typical compaction process (variation of speed and force against time) is described in Figure 3.18, which is inspired from the study of (Olivier 1994). In our study, the procedure consists of four compaction stages: The first stage refers to the state at which the soil is relatively loose and the principle compaction comes from the expulsion of pore air. The speed (0.25 mm/s) in this stage is large. For the second stage, the soil particles have already come into contact and a drainage of excess pore water pressure dominates. In order to make sure that the applied force is efficiently converted into effective stress, a smaller speed of 0.125 mm/s is adopted. For the purpose of arriving at the desired position gradually, another stage with speed of 0.025 mm/s is settled at 1.5 mm before reaching the desired height. Finally, the last stage consists of maintaining the final position until reaching the stabilization of measured force.

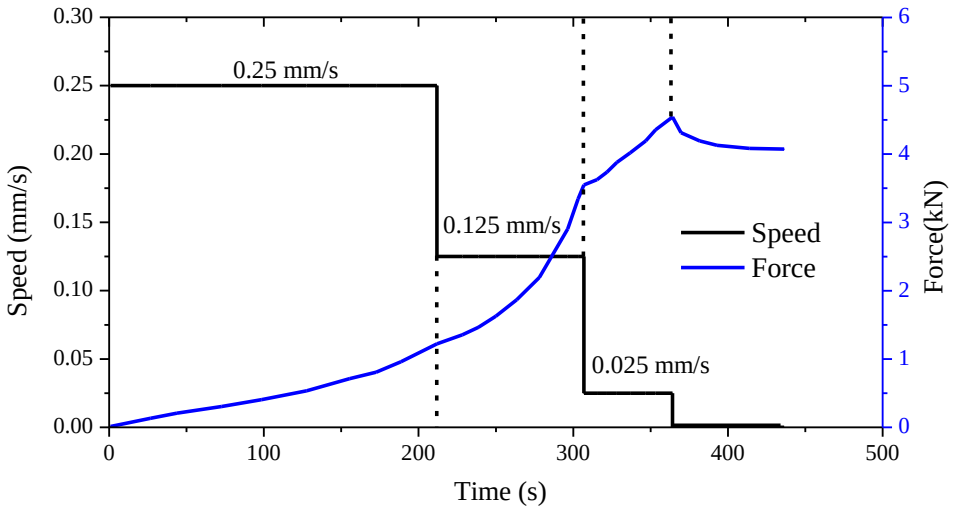

Figure 3.18 Compaction curves illustrated speed vs time and force against time

Verification for specimen's homogeneity

After compaction, the specimen is placed on a balance to check whether the mass loss is below a tolerance of 0.5 g compared to the initial mass of moist soil. In addition, the height of specimen is measured by a vernier caliper, and the distribution of specimen's height for CRA is shown in Figure 3.19(a). It can be seen the deviation of specimen's height is around 0.01 mm-0.02 mm, which sufficiently meets the test requirements in laboratory.

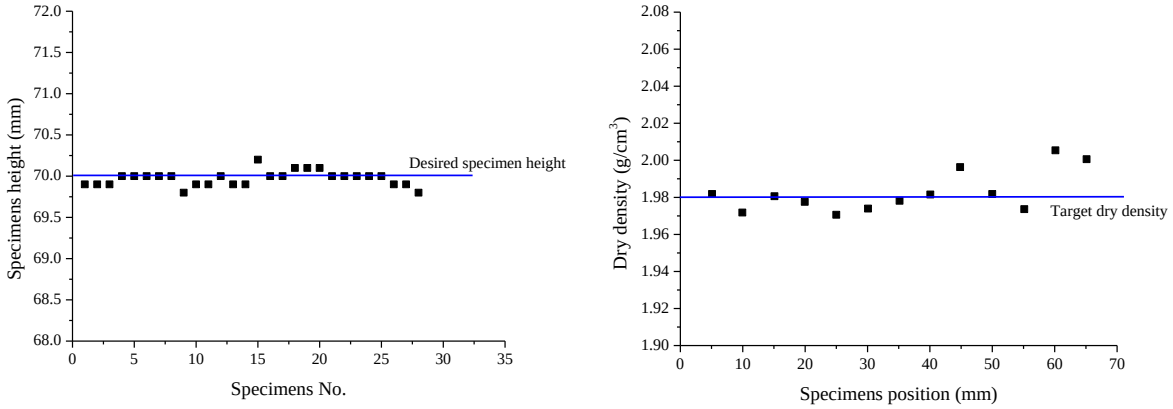

a b

Figure 3.19 (a)Distribution of specimens' height stated on CRA (b) Distribution of dry density along with the position in the direction of specimen's height for CRA (CHAMPIRE 2017)

In addition, a distribution of dry density along with the position in the direction of specimen's height was presented in the study (Florian CHAMPIRE 2017) on CRA. The result obtained by the aide of gamma density meter is shown in 3.19(b). The level of homogeneity of fabricated specimens is quite high, given the maximum deviation of only 1.5%. It is worth noting that in a dynamic compaction, the variation of dry density from top to bottom can reach 11% (Narayanaswamy 2017). This finding further demonstrates the advantage using the double static compaction mould developed by Champiré (2017).

Exploration of optimum state by double static compaction

The experimental set-up for this exploration is shown in Figure 3.20(a), and the static compaction was carried out in a strain-controlled compression testing machine using our developed double compaction mould. STR and CRA were selected as the experimental materials and their characteristics have been presented in the past sections. The oven-dried soil was mixed with different quantity of water and placed in the sealed bags at least 24 hours to reach homogenization. Before making specimens, the moisture content in each sealed bag was checked again to make sure there was not excessive water loss. Each quantity of moist soil was put into the mould and compacted until the desired height (70 mm) is reached. The force of

compaction and the corresponding displacement were recorded constantly at one-second intervals. A specific force-displacement curve was obtained from these readings. The test is performed for different quantities of moist soil, finally a family of force-displacement curves are obtained for different dry densities (depending on the quantity of moist soil) and various water contents. When compaction is finished, the specimen is carefully taken out from the mould and put on a balance to recheck the current mass. In addition, the height of specimen is also verified by a vernier caliper. After that, the specimen is immediately wrapped with a filter paper and a plastic paper to maintain its moisture content in view of suction measurements.

a b

Figure 3.20 (a)Experimental set-up (b) Compacted specimens wrapped with filter paper

To calculate the static compaction energy for each case, an integral formula (3-9) was used accounting for the force-displacement curve measured.

$$E_s = \int F(h)dh \approx \sum \Delta h_i \times F_i \qquad (3\text{-}9)$$

where $\Delta h_i$is the displacement in every integral step, F_i is the corresponding fore.

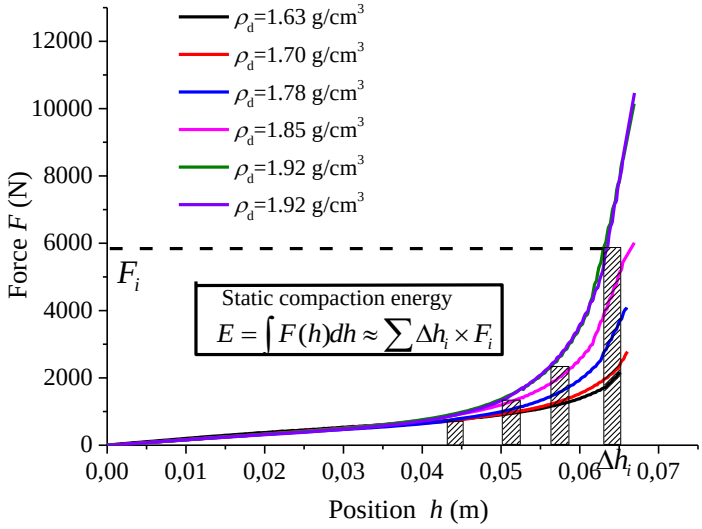

Figure 3.21 Static compaction curves for CRA (w=4.5%) under different dry densities

A compression test on the empty mould was conducted. The corresponding energy was calculated and used for the correction of energy. Table 3.5 and table 3.6 summarize the characteristics of compacted specimens for CRA and STR: moisture content, dry density, void ratio, saturation degree and the corrected static compaction energy.

Table 3.5 Characteristics of compacted specimens for CRA

Moisture Contents (%)	Dry density (g/cm^3)	Void ratio	Saturation degree	Compaction energy (kJ/m^3) after correction
4.45	1.63	0.63	0.19	147.88
4.49	1.70	0.56	0.21	184.41
4.50	1.78	0.49	0.24	302.34
4.49	1.85	0.44	0.27	527.07
4.45	1.92	0.38	0.31	824.12
4.40	1.92	0.38	0.31	875.65
4.20	1.92	0.38	0.29	805.08
10.23	1.77	0.50	0.54	137.06
10.19	1.80	0.47	0.58	154.61
10.15	1.84	0.44	0.61	198.02
10.18	1.91	0.39	0.69	324.10
11.98	1.91	0.39	0.81	194.32
11.94	1.87	0.42	0.76	223.01
11.23	1.94	0.37	0.96	309.05
12.05	1.63	0.63	0.51	19.36
12.05	1.70	0.56	0.57	52.38
12.03	1.77	0.50	0.64	87.15
12.06	1.84	0.44	0.73	122.60
12.15	1.91	0.39	0.83	142.05
13.69	1.88	0.41	0.88	120.27
13.30	1.87	0.42	0.84	113.56
13.17	1.89	0.40	0.86	140.57
14.17	1.85	0.43	0.87	52.61
14.91	1.79	0.48	0.82	49.69
15.07	1.81	0.46	0.86	62.45

Table 3.6 Characteristics of compacted specimens for STR

Moisture Contents (%)	Dry density (g/cm^3)	Void ratio	Saturation degree	Compaction energy (kJ/m^3) after correction
10.58	1.78	0.49	0.57	232.14
10.57	1.78	0.49	0.57	199.27
10.57	1.81	0.47	0.60	215.85
10.54	1.84	0.44	0.64	283.60
10.63	1.86	0.42	0.66	349.98
10.60	1.87	0.41	0.68	426.78
10.50	1.90	0.39	0.71	484.30
11.63	1.83	0.45	0.68	224.13
11.58	1.85	0.44	0.70	249.01
11.60	1.85	0.43	0.71	271.00
11.62	1.86	0.43	0.72	289.70
11.57	1.88	0.41	0.75	378.93
11.62	1.90	0.39	0.78	431.36
12.45	1.80	0.47	0.70	163.64
12.38	1.84	0.44	0.75	217.85
12.38	1.89	0.41	0.81	346.95
13.19	1.86	0.42	0.83	199.72
13.07	1.86	0.42	0.82	241.28
13.00	1.89	0.40	0.86	263.15
14.39	1.78	0.49	0.78	118.39
14.06	1.83	0.45	0.83	173.93
13.56	1.89	0.40	0.90	236.11

3.3.4 Comparison between dynamic compaction and static compaction

All the specimens were placed on the moisture content- dry density curve, marked with related static compaction energy. Meanwhile, the results from Proctor test and the optimum point from fabrication of compacted blocks (CHAMPIRE 2017) were also superposed in the same figure.

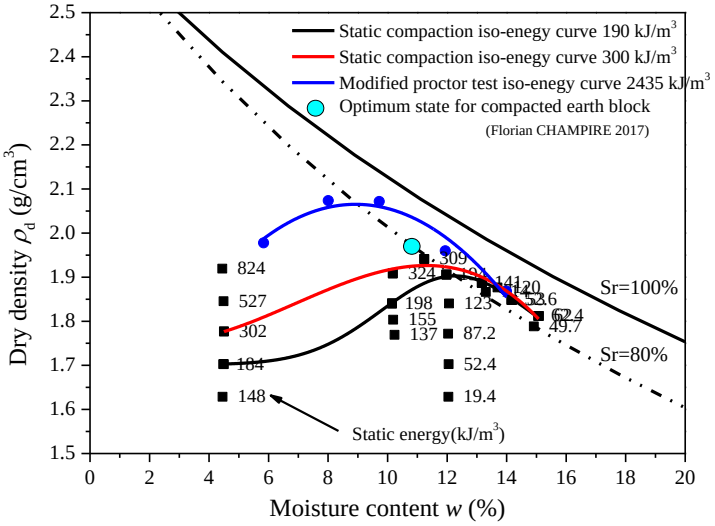

Figure 3.22 Dry density versus moisture content for CRA

Dry density plotted against moisture content for CRA is shown in Figure 3.22. Two iso-energy curves for static compaction (190 kJ/m^3 and 300 kJ/m^3 respectively) are found. With increasing of static energy, the iso-energy curve shifts leftwards and upwards, leading to a reduction of optimum moisture content and an increase of maximum dry density. This indicates that the effect of static compaction energy on the iso-energy curve is quite similar to that resulted from the dynamic compaction energy in Proctor test. Besides, it is worth noting that all the optimum points approximately lie on a line of constant saturation degree (here $S_r = 80\%$ for CRA) regardless of the compaction method (static compaction, Proctor test and CEB fabrication) and compaction energy. This line is quite useful in verifying the optimum state adopted for specimen's fabrication. Similar conclusion can be drawn for STR from Figure 3.23. Two iso-energy curves (220 kJ/m^3 and 350 kJ/m^3 respectively) are observed and all the optimum points lie on a specific saturation degree line ($S_r = 75\%$).

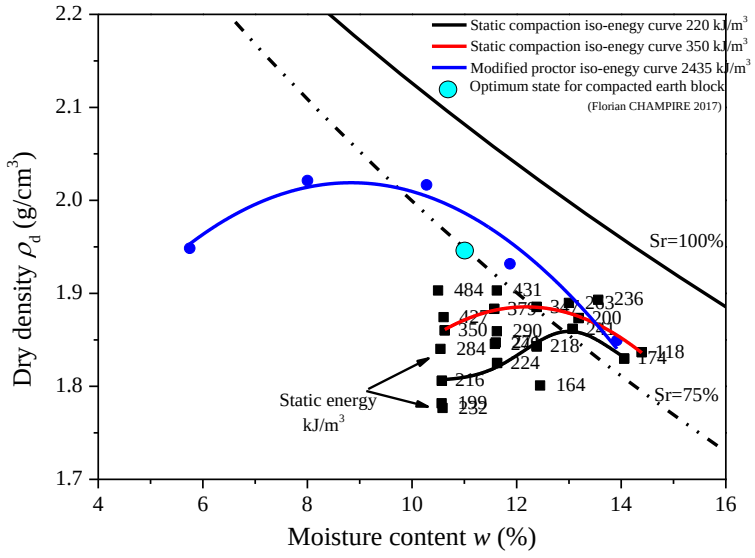

Figure 3.23 Dry density versus moisture content for STR

One thing that should be mentioned here is that the iso-energy curve on the wet side is pseudo due to a drastically decreasing of static compaction energy on this side. At moisture contents beyond the optimum in the case of static compaction, the water phase becomes continuous. Any volume compression would lead to water being expulsed. This leads in turn to an occurrence of consolidation and water begins to exude from the location of screws on the mould, which efficiently reduces the final energy. But the dynamic nature of Proctor test precludes the development of a consolidation phase. The similar kind of behaviour is also found in the study of (Venkatarama-Reddy and Jagadish 1993) for static compaction, in which only the rising portion is presented in his iso-energy curves.

Based on the completed study, it is found that amplitude of dry density obtained from static compaction is lower than that in the Proctor test. Hence the corresponding energy is far less than 2435 kJ/m^3 used in the modified Proctor test. But what will happen for the static compaction energy when dry density is increased to the same level as that of Proctor test?

To answer the aforementioned question, five points on the dry density- moisture content plot, come from the modified Proctor test for soil Lim, were repeated using the double static compaction mould. The repeated points and corresponding energy is illustrated in Figure 3.24. It is found that these points roughly lie on an iso-energy with a value about 900 kJ/m^3, noticing that the energy on the wet side is still lower as mentioned earlier. In comparison with the energy used in Proctor test (2435 kJ/m^3), it seems to say the static compaction process is more energy efficient, perhaps due to the higher energy loss during the impact of falling weight in the Proctor test (Venkatarama-Reddy and Jagadish 1993).

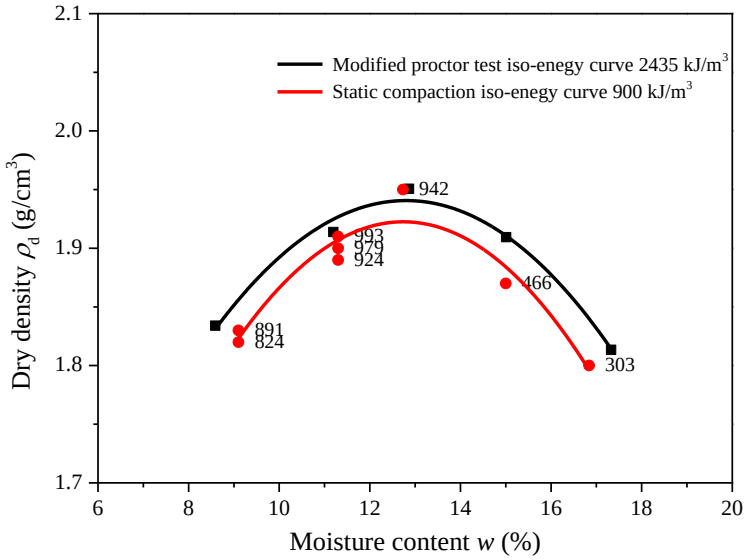

Figure 3.24 Repeating Proctor test points using static compaction and the corresponding energy

3.4 Specimen's suction at fabrication stage

3.4.1 Basic concepts and measurement techniques

The soil suction in the literature usually refers to the matric suction and is defined as the difference between the pore air pressure and the pore water pressure(Sheng 2011). Suction plays an important role on the strength of the earthen materials and relevant studies have been done by (Q.-B. Bui et al. 2014; Gerard, Mahdad, Robert McCormack, et al. 2015; Jaquin et al. 2009). It is widely accepted that earthen materials achieve a component of strength through matric suction which can be considered as an apparent cohesion. As earth material dry, so suction

increases, and consequently there is an increase in apparent cohesion and hence strength. Q. B. Bui et al. (2014) studied suction effects based on three types of soil: a sandy soil, a clayey soil and a clayey soil stabilised by 2% NHL. The results confirmed that suction was an important factor governing the mechanical characteristics of earthen materials. It is also proposed that suction may depend also on type of soil (percentage of clay, type of clay).

A large variety of methods are available for measuring suction in the field or in the laboratory, and all the methods can be classified into two main categories: either direct or indirect. A summary of various instruments used for measuring soil suction is presented in Table 3.7. Each of these measurement techniques has its own limitations and capabilities, and active research is ongoing for further improvement.

Table 3.7 Summary of suction measurement methods (Hu, Yang, and Li 2010)

		Technique (Method)	Suction range (kPa)	Equilibrium time
Direct suction measurement	Matric suction	axis-transition technique		hours
		tensiometer	0-1500	hours
		suction probe		minutes
Indirect suction measurement	Matric suction	time domain reflectometry	0-1500	hours
		electrical conductivity sensor	50-1500	6-50hours
		thermal conductivity sensor	0-1500	hours-days
		in-contact filter paper	all	7-14 days
	Osmotic suction	squeezing technique	0-1500	days
	Total suction	psychrometer technique	100-10000	1 h
		relative humidity sensor	100-8000	hours-days
		chilled-mirror hygrometer	150-30000	10 minutes
		non-contact filter paper	all	7-14 days

Among those methods mentioned above, the technique of filter paper is considered to be simple, economical and reliable (Hu, Yang, and Li 2010). In addition, its wide range of suction measurement attracts many researchers. Using filter paper method, both total suction and matric suction can be studied. The total suction of the soil can be measured by suspending the filter paper (without physical contact) with the specimen in a sealed container. The in-contact filter paper technique is used for measuring matric suction. Direct contact between the filter paper and the soil allows water in the liquid phase and solutes to exchange freely. In the in-contact filter paper technique, water content of an initially dry filter paper increases due to a flow of water in liquid form from the soil to the filter paper until both come into equilibrium. Therefore, a good contact between the filter paper and the soil has to be established. When equilibrium is established between the filter paper and soil, the water content of the filter paper is measured. Then, by using the appropriate calibration curve of the filter paper, suction is estimated. The most commonly used filter papers are “Whatman 42” and “Sleicher & Schuell 59”. The

calibration chart for these two types of filter paper proposed by (ASTM D5298-03 2003) is given in Figure 3.25, the calibration chart corresponds to both total and matric suction.

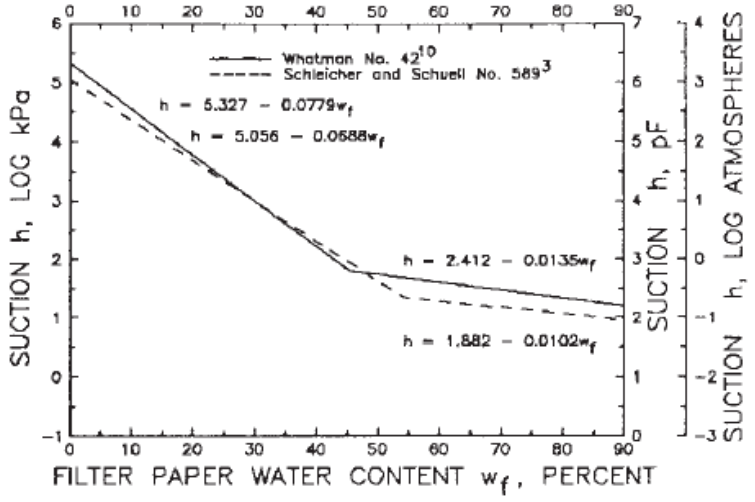

Figure 3.25 Calibration Suction-Water Content Curves for Wetting of Filter Paper (ASTM D5298-03 2003)

3.4.2 Procedures for suction measurement

In this study, only matric suction is measured using "Whatman 42" filter paper in accordance with (ASTM D5298-03 2003). In fact, the osmotic suction could be negligible, since distilled water was always used in the tests, the solute concentration is expected to be very low. Two types of samples are used for the suction measurement: one is the samples from Proctor tests (152 mm in diameter and 126.6 mm in height) and the other comes from the static compaction exploration in last section (35 mm in diameter and 70 mm in height). Both of them have a variety of initial fabrication water contents, which provide the possibility to study the evolution of suction versus moisture content in the soil.

In more details, for samples from Proctor tests, two groups of triple layer of "Whatman 42" filter paper, dried before-hand, were placed in-between the two layers during manufacture. The selected position depends on the total layers in different kinds of Proctor tests (normal or modified). While for the specimens from the static compaction mould, a triple of filter paper was wrapped around the specimen after fabrication, considering the difficulty of putting filter paper into it due to its relatively small diameter. Then, two types of specimen were covered with plastic film to prevent any further evaporation. Samples were then stored at least two weeks in a climate controlled room. So the moisture equilibrium was well established between the sample and the filter paper. Then the filter paper was extracted and the moisture content of the middle sheet, which was not contaminated thanks to its non-contact with the specimen

surface, was determined. The moisture content of samples after equilibrium was measured simultaneously. Using the calibration curve of the filter paper in Figure 3.25, the suction of the sample was calculated. Both of the filter paper arrangements and experimental procedures are shown in Figure 3.26 and Figure 3.27.

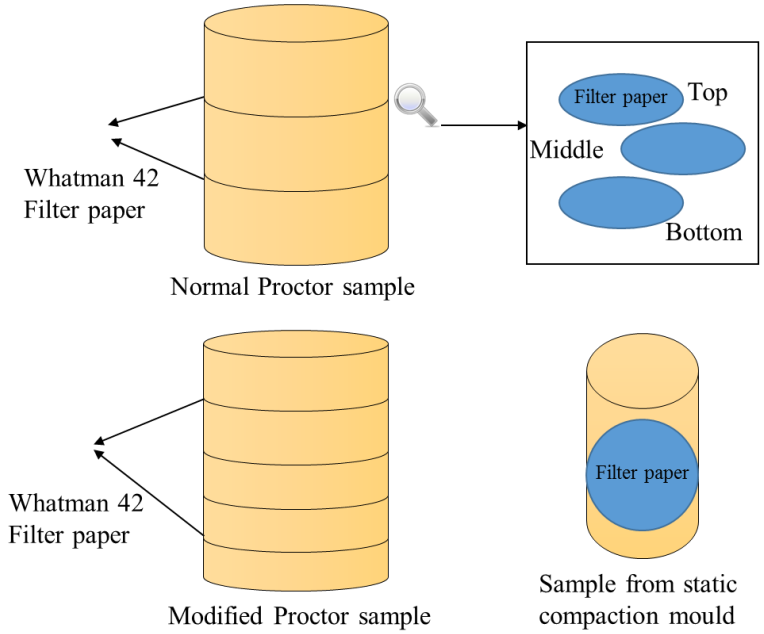

Figure 3.26 Filter paper arrangements for different types of samples

Figure 3.27 Experimental procedures for suction measurement

3.4.3 Results and discussion

The measured suction is plotted against the corresponding moisture content as shown in the following section. It should be pointed out that the suction on these figures represent measurements taken on different specimens with different initial fabricated water contents (i.e. it is not a continuous drying curve from a single specimen) and dry densities. This kind of protocol efficiently reduces time taken in drying process, hence it is widely used in the study of suction on earth materials (Gerard et al. 2015; Jaquin et al. 2009; Narayanaswamy 2017; Soudani 2017).

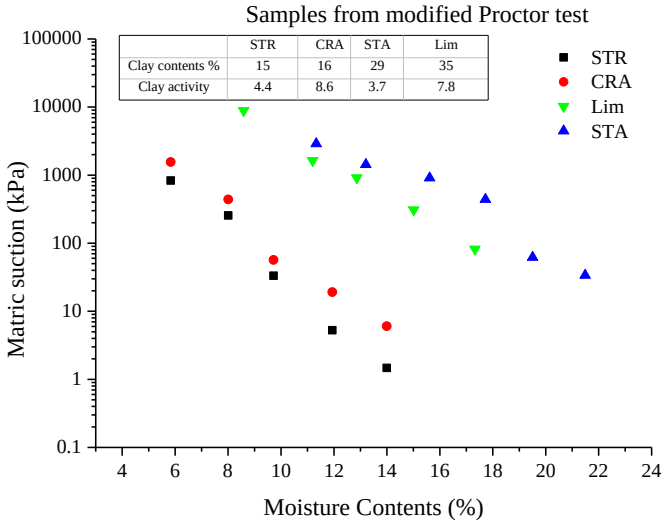

Figure 3.28 Variation of suction following water content for samples from modified Proctor test

Figure 3.28 and Figure 3.29 show the measured suction versus the corresponding water content of sample from modified Proctor test and static compaction respectively. Results of different types of earthen materials are superposed in the same figure. It is obvious to see that the matric suction increases with decrease in soil water content for both of two kinds of compaction method, which is an acknowledged conclusion for the suction in earthen materials. Besides, from the comparison among STR, CRA, STA and Lim in Figure 3.28, these four types of earth materials are approximately divided into two sets: the first set consists of Lim and STA, and they possess a relatively high suction when referring to the same soil moisture content compared with the other set composed by STR and CRA. For example, when the water content in soil is 12%, the magnitudes order of suction in STR and CRA is about 10 kPa while the magnitudes order can reach 1000 kPa for another set. The great difference in suction indicates STA and Lim have higher water sensitivity. This observation can be explained by their higher clay contents which are around double than that contained in STR and CRA. Clay particles have smaller size (<0.002 mm) and the shape of thin sheets, which combine to give clay a very large

surface area for a given volume of solid, making surface effects dominant. This allows an adsorbed water layer, more structured than that of free water, to form around clay particles, thereby generating a higher suction at the same moisture content. Considering that suction plays an important role on the strength, it is necessary and interesting to study the influence of clay content on the hydro-mechanical behaviour of the earthen materials. The relevant study about the effect of clay will be introduced in next chapter.

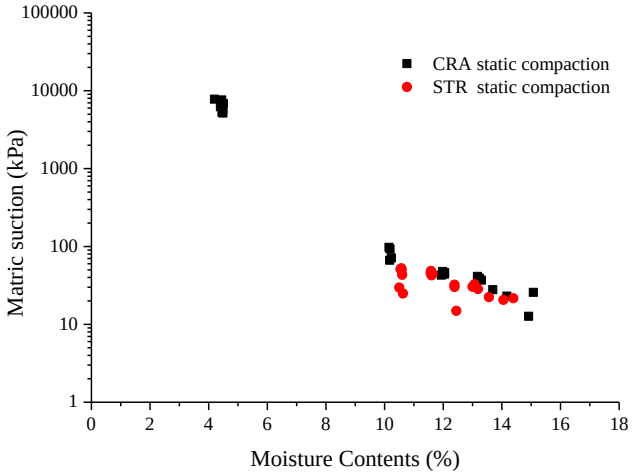

Figure 3.29 Variation of suction following water content for samples from static compaction

A comparison of measured suction for CRA between samples from modified Proctor test and static compaction is illustrated in Figure 3.30. Meanwhile, the suction of CRA measured by Narayanaswamy (2017) is also superposed in the same figure. Narayanaswamy (2017) focus on studying the relatively dry range (0.1%- 8%) in terms of moisture content in the soil while our study is concentrated upon the range from 4% to 16%. However, it is found that the measured suction values are quite consistent in the coincident range. In addition, it is worth noting that all suction values approximately lie on the same line regardless of the compaction method employed for sample fabrication.

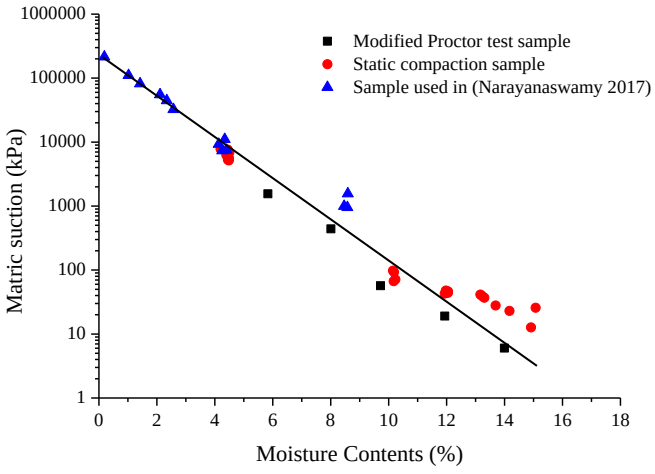

Figure 3.30 Comparison of measured suction for CRA using filter paper from different sources

The influence of compaction energy on the evolution of suction is reported in Figure 3.31. It is found the evolution of suction versus water content approximately lies on a specific line for all cases. It is also worth noting the superposition extent in high suction range is better than that on lower suction range, in other words, suction is more easily influenced by compaction energy in the lower range.

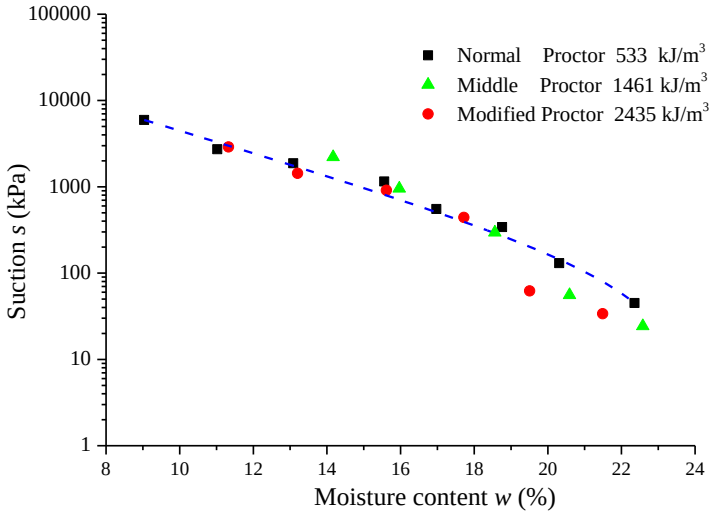

Figure 3.31 Influence of compaction energy on the evolution of suction

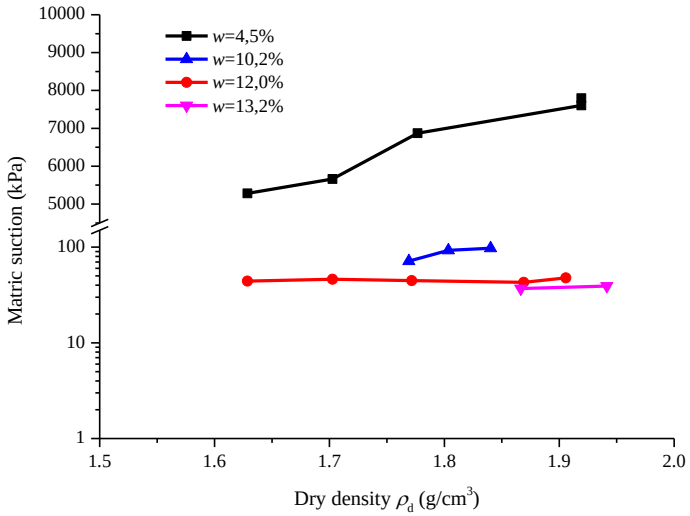

Figure 3.32 Variation of suction versus dry density for CRA samples from static compaction

There is no doubt the compaction method and compaction energy will result in the change of dry density. Hence, measured suction with respect to sample dry density is plotted with different moisture contents for samples STR and CRA from static compaction. Observation of Figure 3.32 and Figure 3.33 indicates the measured suction is insensitive with variation of dry density at the same water content; which explains why the compaction method and compaction energy have little influence on the evolution tendency as mentioned earlier.

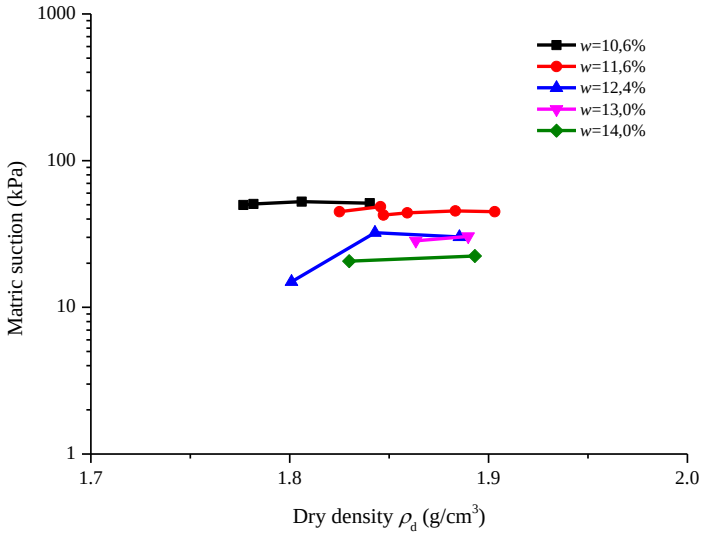

Figure 3.33 Variation of suction versus dry density for STR samples from static compaction

A recent study (Bruno 2016) indicates that compaction effort has a significant influence on the mechanical properties of earthen materials (affected by density and, hence, by inter-aggregate porosity) but has no influence on hygroscopic behaviour (controlled by intra-aggregate porosity). This result is based on the microstructural analysis and provides a possible explanation for the suction behaviour in our study. Mercury intrusion porosimetry tests is suggested to be done on the specimens from different compaction form (method or energy) in the future study, thereby assessing the effect of the compaction procedure on the microstructural properties of earthen samples.

3.5 Shrinkage test

In order to maximize its density so as to acquire appropriate mechanical properties, crude (untreated) earthen material is compacted at its optimum moisture content (around 8-12%) inside temporary formwork to form rammed earth walls. After construction, both internal and external compacted earth walls are left to dry in a suitable climate and reach a generally lower moisture content at working conditions (1-2%). This drying process is expected to cause an obvious shrinkage and induce internal stresses to earthen infrastructures. Hence, it is important to observe and quantify this behaviour of compacted earthen samples in the laboratory, thereby providing a proper evaluation and eventually preventive measures for the in-situ earth construction.

Some investigations on the shrinkage of earthen materials have been carried out in the past. Ashour and Wu (2010) studied the shrinkage behaviour of earth plasters with natural fibres under different curing conditions. It was established that shrinkage-induced crack formation

decreases with increasing fibre content and decreasing temperature. Hence, lower curing temperature and higher fibre content are to be preferred to improve the performance of earth plasters. In the study of P. Walker and Stace (1997), drying shrinkage tests were carried out on the cement-stabilised compressed earth blocks with different clay contents. It was found that the drying shrinkage increased as clay mineral content increased and higher cement usage proved more effective at controlling shrinkage. Kenai, Bahar, and Benazzoug (2006) used samples from Proctor test to explore the linear shrinkage behaviour. Cement and sand stabilization on the variation of final linear shrinkage were also investigated and compared to that of unstabilised soil. The experimental results indicate that the initial water content at fabrication has important impact on the final shrinkage and the addition of a stabilizer can effectively reduce shrinkage.

The aforementioned studies emphasize on the measurement of final shrinkage for the stabilised earth. In this study, a quasi-continuous shrinkage measurement was performed on the unstabilised earth sample (STR and CRA) under a controlled environment at 20° C and 55% RH.

3.5.1 Test procedures and apparatus

The specimens made by static compaction method were used for the shrinkage test, with different initial water content at fabrication and dry densities, allowing us to study the effects of these factors on shrinkage. The shrinkage measurements were effectuated after the suction tests mentioned in the last section. More exactly, the height and moisture content of samples were measured precisely through a vernier caliper and balance respectively; thereby determining their initial state. Then the sample was put into a thermostatic room at 20° C and 55% RH, on an electronic balance with a 0.01 g precision and allowed for evaporation to take place. The time evolution of the sample height was measured using a previously calibrated LVDT (Linear Variable Differential Transformer) with a resolution of 0.00l mm. The weight and height of the sample were recorded quasi-continuously at 1 min interval until they stabilised to constant values, which took about 3 to 4 days. At the end of the test, the sample was placed into the oven to obtain its dry mass which would be used later as a reference base for other deductions. The experimental set-up and thermostatic condition for shrinkage tests are illustrated in Figure 3.34.

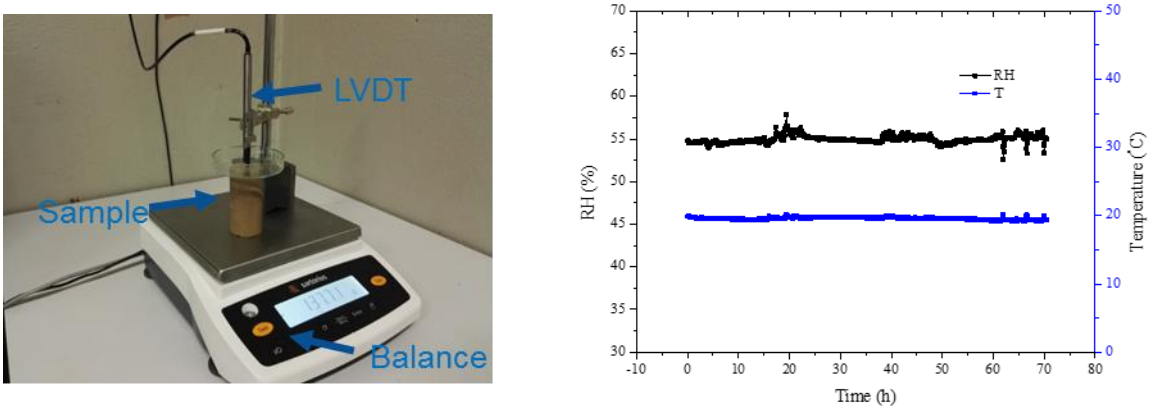

Figure 3.34 Experimental set-up and thermostatic condition for the quasi-continuous shrinkage test

3.5.2 Results and discussion

The evolution of moisture content against time are presented in Figure 3.35 and 3.36 for STR and CRA respectively. Inspection of these evolutions indicate the final water content stabilises at a specific value regardless of initial moisture content and dry density at the time of fabrication. In addition, under the same experimental conditions, CRA possesses a higher stabilised water content (around 2%) than that of STR (about 1%), which indicates that CRA has a higher ability to absorb and store moisture from the surrounding air. This is attributable to the higher clay activity of CRA, considering that their clay contents are similar. More detailed sorption-desorption tests will be shown in the next section to characterise the hygroscopic behaviour of earthen materials.

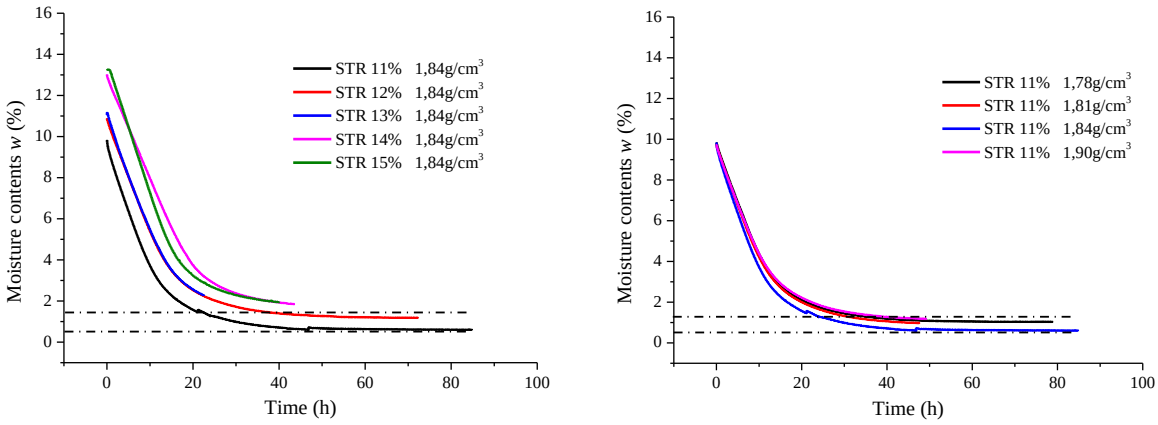

a b

Figure 3.35 Water content evolution against time for STR: a. series with different initial fabricated water content b. series with various compacted dry density

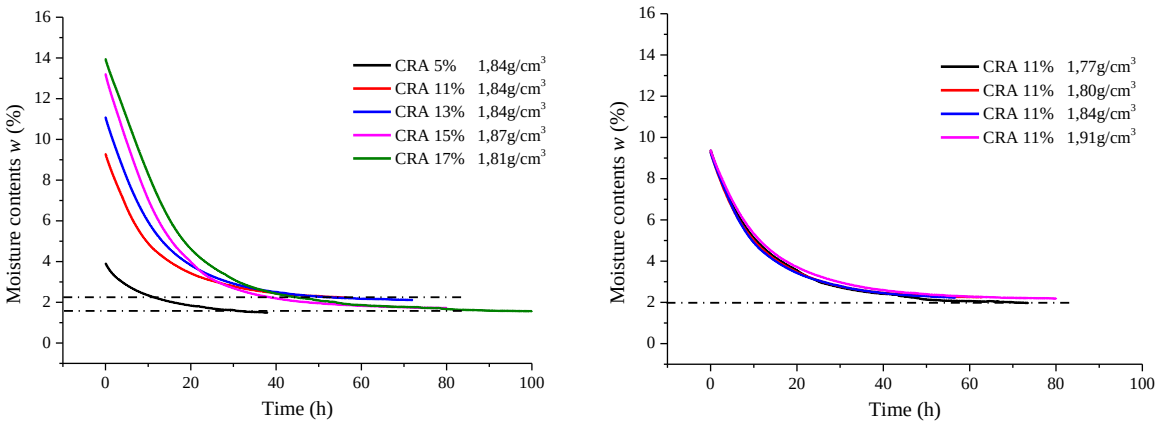

a b

Figure 3.36 Water content evolution against time for CRA: a. series with different initial fabricated water content b. series with various compacted dry density

Fig 3.37 and 3.38 depict the vertical strains versus time elapsed during the test, for STR and CRA respectively. The majority of vertical strains in soils was observed within the first 20 h, and subsequent axial strains were continuously recorded until no shrinkage movement was observed. It is observed the compaction moisture content has a large influence on the magnitudes of vertical shrinkage strain values: with increasing of moisture content, this value increases drastically. Take CRA for example, when water content increases from 11% to 15%, the final vertical shrinkage strain changes from 0.4% to1.3% with a three times of amplification. Meanwhile, the corresponding needed time for equilibrium becomes larger. In contrary, the effect of compacted dry density can be negligible, and the vertical shrinkage strain curves tend to coincide within the dry density range investigated in this study. A comparison between these types of soil shows CRA possesses higher vertical shrinkage strain, particularly at relatively higher water content (e.g.15%).

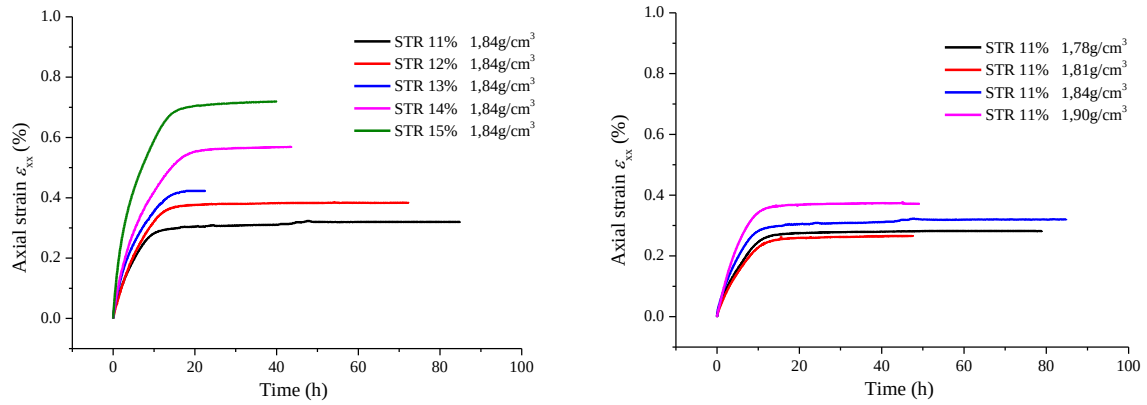

a b

Figure 3.37 Vertical shrinkage strain results for STR: a. series with different initial water content at fabrication b. series with various compacted dry density

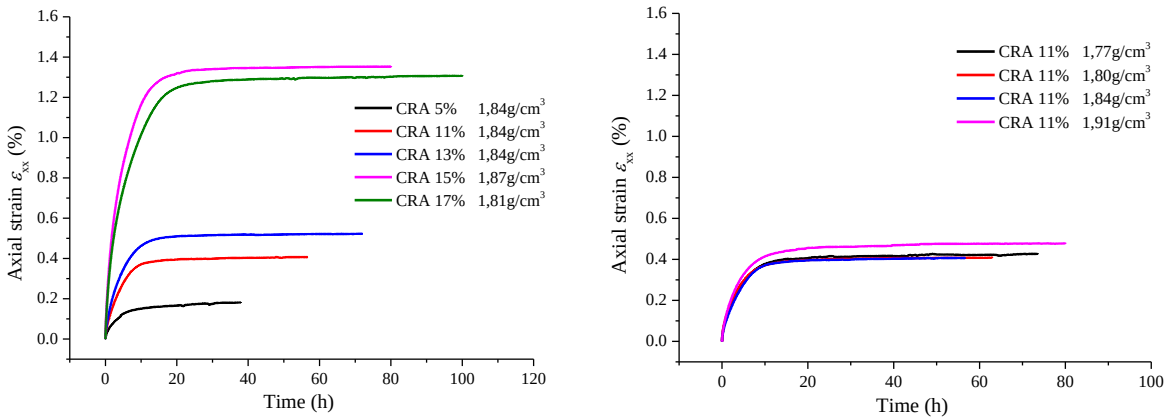

a b

Figure 3.38 Vertical shrinkage strain results for CRA: a. series with different initial fabricated water content b. series with various compacted dry density

The soil shrinkage behaviour is often presented by plotting the void ratio against the moisture ratio (Peng and Horn 2005); they are defined as:

$$e = \frac{V_V}{V_s}; \qquad \vartheta = \frac{V_w}{V_s} \tag{3-10}$$

e and ϑ are void ratio and moisture ratio, V_V, V_s and V_w are the volumes of pore, solid and water.

This shrinkage curve generally portrays four distinct shrinkage zones as shown in Figure 3.39:

i. Structural shrinkage: soil volume decrease is smaller than the water loss.

ii. Proportional shrinkage: soil volume decrease is equal to the water loss.

iii. Residual shrinkage: soil volume decrease is smaller than the water loss.

iv. Zero shrinkage: the volume of soil does not change as soil water is removed.

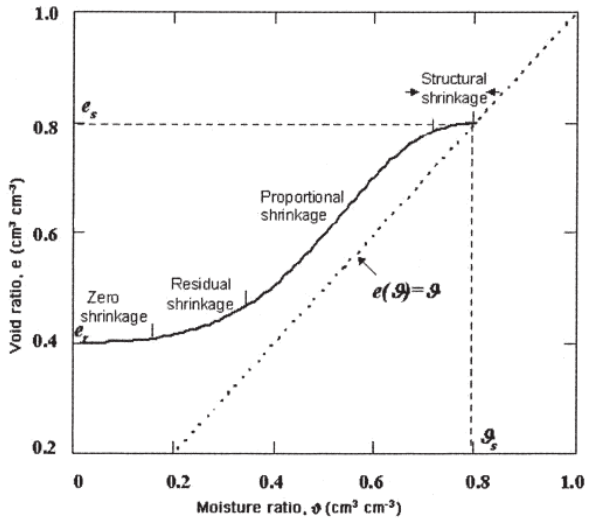

Figure 3.39 Schematic diagram for the typical shrinkage curve with four shrinkage zones (Peng and Horn 2005)

In this study, only the vertical shrinkage strain is measured while isotropic shrinkage is assumed to calculate the volume change. The corresponding variation of void ratio and moisture ratio during shrinkage are calculated through Eq. (3-10) and presented in Figure 3.40

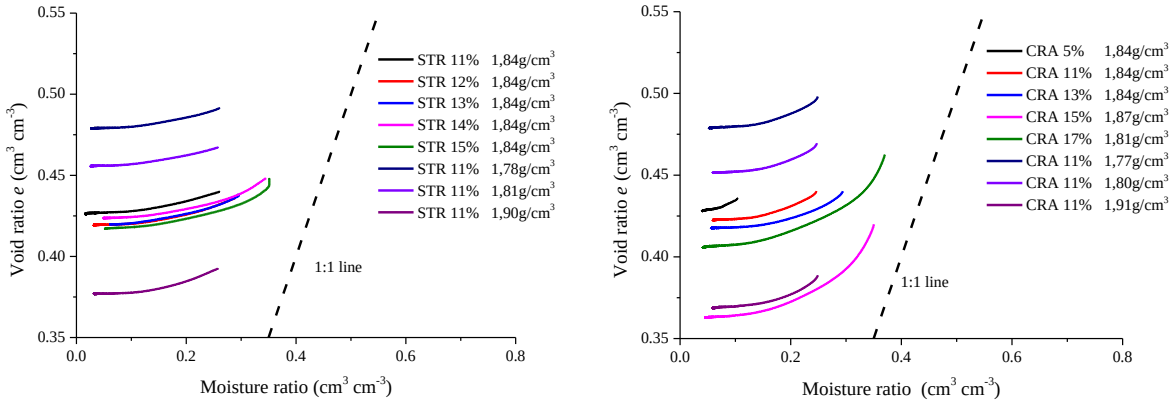

STR CRA

Figure 3.40 Shrinkage curves plotting void ratio versus moisture ratio for STR and CRA

A synthetical observation in Figure 3.40 shows only residual shrinkage and zero shrinkage appear for most of samples in our test. For some cases with higher water content (e.g. CRA 15%, CRA 17%), a period of proportional shrinkage is captured. Therefore, shrinkage tests with higher compaction water content are suggested to be carried out in the future study, in order to obtain a more complete shrinkage curve for earthen materials.

Furthermore, the distribution of shrinkage curves (void ratio versus moisture ratio) are visibly affected by the compacted dry density while the influence of initial compaction water content is not obvious. The results also indicate that the shrinkage curves for different intensities of soil compaction (i.e. different dry densities after compaction) are approximately parallel.

3.6 Isothermal sorption-desorption test

Earthen material is taken as hygroscopic porous material which has the ability to absorb and store moisture from the surrounding air. In order to maintain thermodynamic equilibrium with ambient air at changing relative humidity, the material absorbs or desorbs moisture. Sorption-desorption isotherms are usually used to depict the hygroscopic behaviour of materials. It establishes the relationship between the moisture content in the material and the relative humidity of the environment in contact with it, at a given temperature. The sorption-desorption isotherm refers to two different curves, one for sorption, and another for desorption. Together, they reveals the existence of a hysteretic behaviour of sorption and desorption.

There are two kinds of widespreadly used methods in laboratory for the determination of isothermal sorption-desorption: one is called desiccator method using different salt solutions, and the other one is dynamic gravimetric sorption method, commonly called the DVS (dynamic vapor sorption) method.

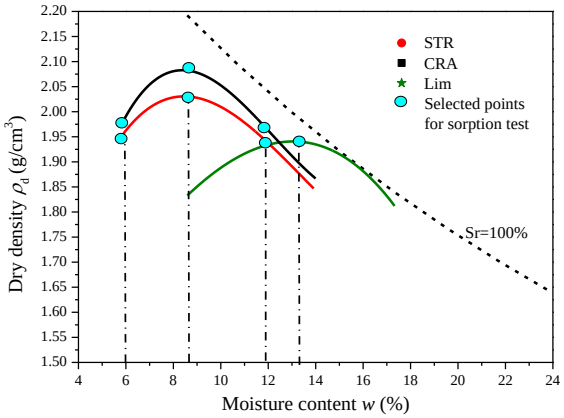

Figure 3.41 Schematic diagram of selected points for isothermal sorption-desorption tests

In this study, samples of STR, CRA and Lim, fabricated at the optimum state with double static compaction mould, are used to conduct isothermal sorption-desorption tests using desiccator method. Besides, the effect of deviation to 'wet side' and 'dry side' (referring to optimum state) on the sorption curves has also been investigated. The selected points for desiccator method is presented in Figure 3.41. Only Lim is used for the DVS method, and the corresponding result is compared to that from desiccator method.

3.6.1 Desiccator method

Desiccator method is used in sorption-desorption test according to ISO 12571 (2000). The sorption stage consists in successively putting a previously dried sample in several environments of increasing relative humidity (RH) and constant temperature. The sample is periodically weighed and it stays within a given environment until constant mass (Fabbri et al. 2017). While the desorption stage can be fulfilled through the inverse process. In more detail, three representative samples of each experimental condition were firstly placed in aluminum containers, in order not to lose material during the sorption test. Then all the samples were placed into oven at 105 °C in order to start the test at dry mass. It should be noticed the dry mass obtained here will be taken as a reference for the calculation of moisture contents during sorption-desorption test. After that, all the samples were placed in a series of sealed plastic box with several relative humidity. The relative humidity within the box is fixed by equilibrium with saturated saline solutions through the activity of its solvent (that is liquid water). Test

begun with the lowest relative humidity, samples were weighed periodically (once per day) using a balance with an accuracy of 0.0001g. When equilibrium at this RH level was reached, all the samples were transferred to next level of relative humidity thereby a sorption stage is ongoing. The same procedure was repeated until reaching the highest RH selected (here refer to 97%), then the desorption stage started following decreasing of relative humidity. Experimental apparatus and samples for isothermal sorption-desorption test using desiccator method are shown in Figure 3.42.

Table 3.8 Summary of RH values for the selected saturated salt solutions at 23° C

Saturated Salt solutions	KCH_3CO_2	K_2CO_3	$Mg(NO_3)_2$	NaCl	KCl	K_2SO_4
RH (%)	23	43	54	75	85	97

All the procedures were performed in a climate controlled room at 23°C and a Rotronic HygroLog HL-NT sensor was used to monitor and guarantee the relative humidity and temperature in those boxes. The value of the equilibrium relative humidity for the selected saturated salt solutions at 23° C is given in Table 3.8.

Figure 3.42 Experimental apparatus and samples for isothermal sorption-desorption test using desiccator method

Results from isothermal sorption-desorption test using desiccator method are reported in Figure 3.43. Comparison of sorption-desorption curves reveals Lim has the highest ability to absorb and store moisture from the surrounding air among three types of earth, due to its relatively higher clay content (35%). CRA possesses little higher hygroscopic property in comparison with STR. Noting the quite similar quantity of clay content between STR and CRA, this observation is conjectured attributing to the higher clay activity in CRA. In addition, when sample desorption stage reaches 55% RH, the relevant absorbed water contents in STR and CRA are 1% and 2% respectively, which verifies the final equilibrium moisture content in the shrinkage test.

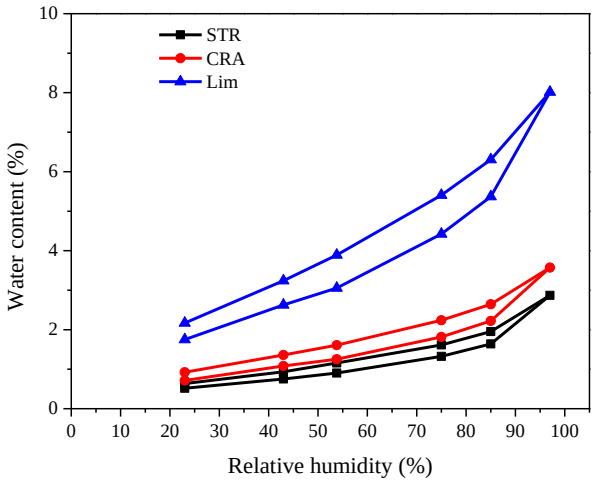

Figure 3.43 Sorption-desorption curves for three earthen materials using desiccator method

The influence of wet side' and 'dry side' (referring to optimum state) on the sorption-desorption curves has been presented in Figure 3.44 for both STR and CRA. It has to recognize there is no obvious difference in terms of hygroscopic ability when comparing these three states. This conclusion tends to in consistent with the suction behaviour mentioned earlier: compaction procedure has a significant influence on the mechanical properties of earthen materials (affected by density and, hence, by inter-aggregate porosity) but has no influence on hygroscopic behaviour (controlled by intra-aggregate porosity).

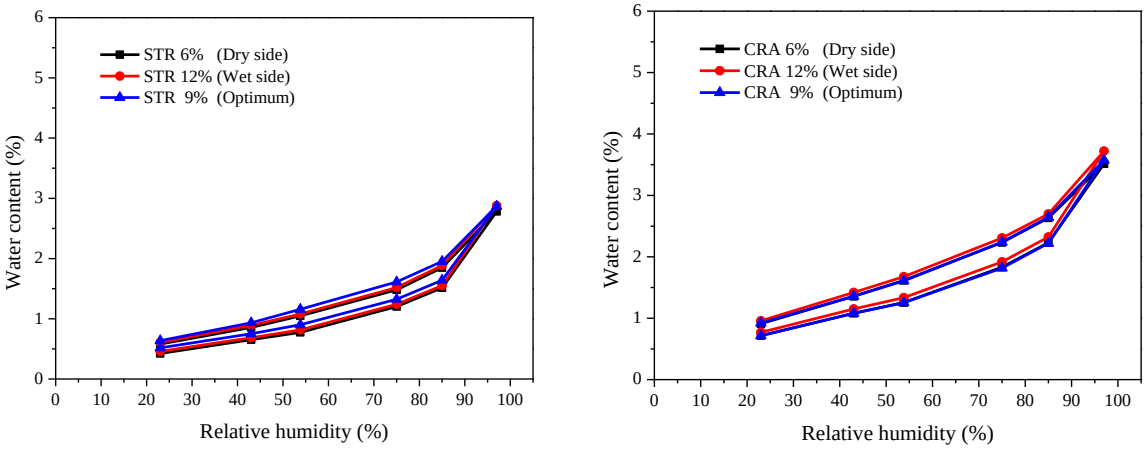

Figure 3.44 Sorption-desorption curves for STR and CRA at different state (dry, wet and optimum)

3.6.2 DVS (dynamic vapor sorption) method

Dynamic Vapor Sorption (DVS) is a gravimetric technique that measures how quickly and how much of a solvent is absorbed by a sample: such as a dry powder absorbing water. It does this by varying the vapor concentration surrounding the sample and measuring the change in mass which this produces. Water vapor is most commonly used in the measurement. DVS Intrinsic

from the Surface Measurement Systems was used in this study. It is able to rapidly measure uptake and loss of moisture by flowing a carrier gas at a specified relative humidity (or partial pressure) over a sample (from several milligrams to several grams depending on the device used) suspended from the weighing mechanism of an ultra-sensitive recording microbalance. DVS Intrinsic has the similar theory with desiccator method for drawing sorption–desorption curves: variations in the gas's relative humidity are increased to next level automatically when the target condition in mass stability is reached in the current RH level. But the usage of microbalance provides the possibility to determine sorption behaviour accurately on very small sample sizes, thus minimizing the equilibration time required. Using this protocol, a sorption–desorption loop can be made in only a period of 10 days while it takes approximatively 3 months by using the desiccator method (Time from this study on the earthen materials).

Sorption-desorption test results for Lim from DVS method is reported in Figure 3.45 (a) as well as the result from desiccator method. A misalignment is found through the direct comparison between curves from these two different methods. The reason for this phenomenon has been pointed and underlined by (Labat et al. 2016): the reference dry mass used to calculated the water content is intrinsically different for the two methods; the dry mass considered by the DVS is obtained by drying the sample through a flow of dry air at 23 °C, while the dry mass for the desiccator method is commonly estimated by drying in oven at 105 °C.

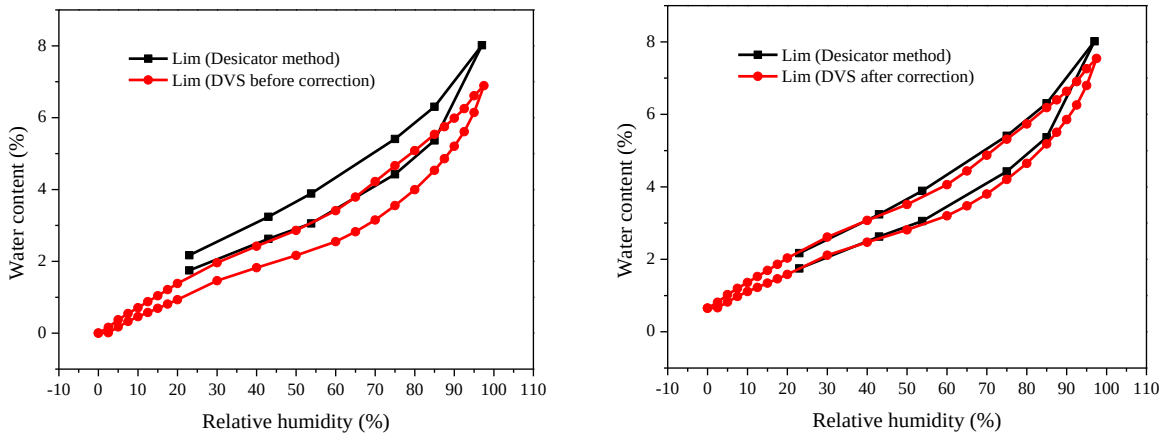

a before correction b after correction

Figure 3.45 Comparison between the sorption curves obtained with the DVS and with the desiccator method for Lim

Therefore, a correction process is adopted following the method proposed by (Fabbri et al. 2017): DVS sample is dried in an oven at 105 °C after (or before) the sorption–desorption test. This dry mass, noted as $m_d^{105°C}$ is taken as the reference to calculated the water content by the following formula:

$$w_{DVS}^{Corrected} = \frac{m_d^{105°C}}{m_d^{23°C}} (1 + w_{DVS}) - 1 \quad (3\text{-}11)$$

where $m_d^{23°C}$ is the dry mass through a flow of dry air at 23 °C in DVS Intrinsic, w_{DVS} and $w_{DVS}^{Corrected}$ are the water contents before and after correction. After correction, it can be seen results from these two kinds of methods are quite consistent (Figure 3.45 (b)).

3.7 Conclusion

In this chapter, a series of physical properties tests were firstly carried out in laboratory on four kinds of crude earth materials (STR, CRA, STA and Lim). Results indicate all these soils have a dispersion in particle size distribution curves, they contain fine gravel and sand with cohesive soils (silt and clay) to act as a binder between the grains. To be precise, clay content in STA and Lim are double than that in STR and CRA. Correspondingly, the plastic index is found to be affected by the clay content.

A detailed specimen fabrication procedure using a homemade double static compaction mould was described and compared with the traditional Proctor test. A series of iso-energy curves are observed for the static compaction. In addition, all the optimum points approximately lie on a specific saturation degree line regardless of the compaction method (static compaction, Proctor test and CEB fabrication) and compaction energy. This line should be quite useful in verifying the optimum state used for specimen's fabrication.

Suction was measured by a simple filter paper method. Materials with high clay content tend to possess a higher suction. Besides, matric suction increases with decrease in soil water content and all the suction values approximately lie on the same variation tendency line regardless of various compaction methods and compaction energy during sample fabrication. Meanwhile, sorption-desorption tests were conducted through desiccator method and DVS method respectively. Results from two methods is quite consistent. Lim has the highest hygroscopic ability to absorb and store moisture from the surrounding air among three types of earth, due to its relatively higher clay content (35%).

All the results indicate clay content and water content (relative humidity) are of vital importance to the characteristics of earthen materials, which greatly motivates the study in next chapter: triaxial test to study the effect of clay content and relative humidity on loading-unloading shear behaviour.

Chapter 4
Loading-unloading shear behaviour of compacted earth with respect to clay content and relative humidity

4.1 Introduction and research motivation

In unstabilised compressed earth, the clay mineral acts as a binder and provides adequate bonding for larger grains. Experimental investigation in laboratory on four types of crude earth materials indicates clay content has a non-negligible effect on their characteristics, particularly on the plastic index I_p, suction and hygroscopic ability. In addition, as a hygroscopic porous material that contains quantity of active clay minerals, crude (untreated) earth is always compacted at its optimum moisture content inside temporary formwork to form walls. After the construction, both internal and external compacted earth walls can be subject to large changes in relative humidity from ambient environment.

All factors mentioned above motivate the following queries in regard to the performance of compacted earthen materials:

- What is the impact of clay content and relative humidity respectively, on the mechanical performance (strength, Young's modulus, residual strain etc.) of compacted earthen materials?
- Is there an interactive influence of clay content and relative humidity on the mechanical behaviour of compacted earthen materials?

In order to answer the above query, some studies have been conducted by several researchers in the past. J.-C. Morel et al. (2007) carried out direct testing, RILEM test and indirect flexural strength testing, to determine the compressive strength of compacted earth blocks, thereby exploring the influence of moisture content and dry density on the mechanical behavior. Incidentally, these authors also studied the effects of aspect ratio of the sample on the measurements. A clear understanding on the influence of moisture content, has been obtained by a few recent studies with different kinds of earth samples(Q.-B. Bui et al. 2014; Champiré et al. 2016; Gerard, et al. 2015). All these studies lead to the conclusion that the behavior of earthen materials is strongly influenced by its water content (which is linked to the relative humidity of the surrounding air). However, most of the previous studies tend to explore earth mechanical behavior using unconfined compression tests, and in a few cases indirect traction tests, which is not sufficient to consider the complicated stress condition. Hence, triaxial tests are suggested to be done in order to complete the study of mechanical behaviour on compacted earth materials.

The performance of clay plasters in regard to the water content and the clay/sand ratio was examined by Emiroğlu et al. (2015). It was found that both the compressive strength and amount

of shrinkage decreased with decreasing amount of clay in the mixture, and an optimum clay/sand ratio between 0.43 and 0.66 by weight was proposed when shrinkage and compressive strength were considered. Other researchers' studies also verified the above viewpoints (Delinière et al. 2014; C H Kouakou and Morel 2009). Similarly, Taylor et al. (2006) reported an increase of the compressive strength of earthen plasters with increasing clay content, while the stiffness modulus was not affected. In some other studies, conflicting opinions have been raised on the effects of clay content on shear strength. Aforementioned studies tend to focused on evaluating characteristics of ready-mixed clay plasters rather than compacted earth.

In this chapter, the first objective is to explore the influence of clay content on the loading-unloading shear behavior at variable water contents, controlled by relative humidity. To this end, the evolution of stress and strain components (axial, radial, volume) were measured; the evolution of mechanical properties (failure strength f_c, Young's modulus E and residual strain ε_{res}) were also deduced from these measurements.

Beyond the investigation of the above mechanical characteristics and their evolutions at various hydric condition, the second objective is to explore the failure condition under the framework of unsaturated soil mechanics using Bishop's generalized effective stress approach. It is a classical result in unsaturated soil mechanics that with a suitable definition of the effective stress, failure states plotted in the (p', q) plane lies approximately on a single line (Khalili and Khabbaz 2002; Nuth and Laloui 2008). The possibility of extending this classic result from unsaturated soil mechanics to the case of compacted earths seen as sand-silt-clay mixtures at very low water contents was explored here. The existence of such a "unified" failure criterion would be an important element for the eventual development of a constitutive model and ultimately to the practical design of earthen constructions.

4.2 Materials and methods

4.2.1 Lim and two artificial earthen materials

To study the impact of clay content on the hydro-mechanical behaviour, the protocol of reducing the clay content by adding fine sand into crude earth is adopted. Observations on the characteristics of four crude earth (mentioned in last chapter) indicate Lim possesses the highest clay content of 35% with a high activity. These properties make Lim more suitable and easy-to-operate for this protocol. Therefore, two artificial soils Mix1 and Mix2 were prepared by mixing natural soil Lim with fine sand, with clay contents respectively of 17% and 26%. The

fine sand used in this study was prepared from dry Hostun HN31 sand. This fine-grained siliceous sand is characterized by a grain density of 2.65. This material is considered as a reference sand for the European geotechnical laboratories. Fig 4.1 represents the grain size distributions of Lim, sand, ‘‘artificial” soils Mix1 and Mix2.

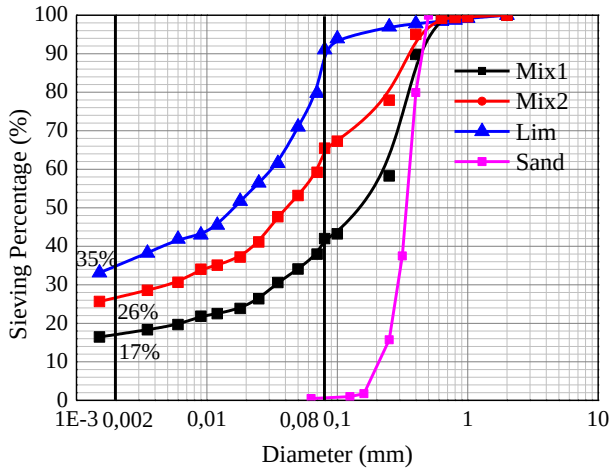

Figure 4.1 Particle size distributions of Lim, Mix1, Mix2 and fine sand

The isothermal sorption-desorption tests have also been carried out on these three soils by DVS method. It should be noticed that the results shown in Figure 4.2 depict the raw data before correction.

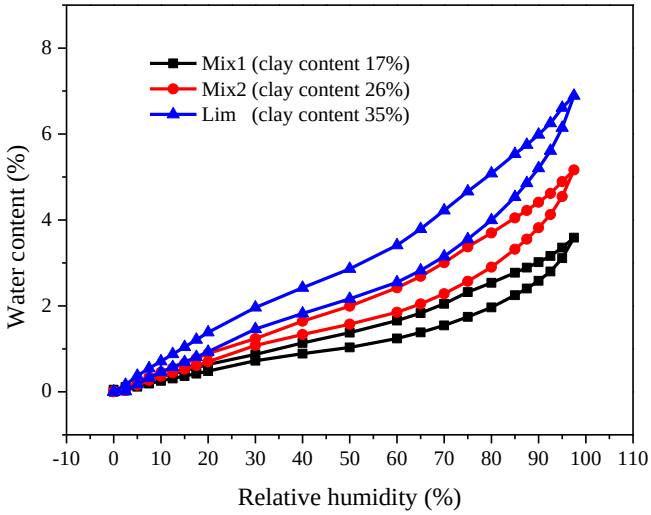

Figure 4.2 Sorption-desorption curves for three soils using DVS method

As expected, the results show an increase of the hygroscopic ability with increasing clay contents. Taking the end of sorption process for example (RH=97.5%), when clay content increases from 17% to 35%, the corresponding absorbed water content becomes double (from

3.5% to 7%). In addition, soils with higher clay content tends to possess more obvious hysteresis phenomenon.

4.2.2 Sample preparation

The optimum condition of the Lim earth from modified Proctor test was used to prepare specimens. Besides, in order to make the comparison of different soils meaningful and easily interpretable, this optimum condition (12.5%, 1.95 g/cm^3) is also applied to Mix1 and Mix2. Adequate quantities of each soil were prepared at the target moisture content and placed in sealed bags at least 24 hours to reach homogenization. Before making specimens, the moisture content in the sealed bags was rechecked to make sure that there was not excessive water loss. Cylindrical samples (3,5cm diameter and 7cm high) were fabricated using a home-made mold which allows a double compaction (compression applied simultaneously at both ends of the sample) at controlled displacement rate. This double compaction ensures an adequate homogeneity.

Figure 4.3 Fabricated samples and their conditioning process using saturated salt solutions

After fabrication, samples were cured following a desorption process in home-designed sealed box containing saturated salt solutions, themselves stored in a climatic chamber at a constant temperature of 23 °C ± 2 °C. The relative humidity inside these boxes was regulated with saline solutions according to the (ISO 12571 2000) standard at three different relative humidities (23%, 75%, and 97%).The temperature and relative humidity were monitored with HMP50 sensors from Campbell Scientific, Inc., Logan, UT. The specimens were weighted every day until thermodynamic equilibrium is reached (i.e. constant mass with a variation lower than 2% for at least one week). Due to the relative humidity of the air in the sealed box, water exchanges appear through vapor transfers between the sample and its surrounding, which induces a given total suction at thermodynamic equilibrium within the sample, given by Kelvin's law:

$$s = -\frac{\rho_w RT}{M_w}\ln(RH) \tag{4-1}$$

In the above relation, *s* is theoretically the total suction (sum of matric and osmotic components), *R* is the constant of perfect gases (*R* = 8.3143 J/mol/K), *T* is the temperature in Kelvin, M_w is the molar mass of water (M_w = 0.018 kg/mol), ρ_w is the bulk density of water (ρ_w = 1000 kg/m^3), and *RH* is the relative humidity. Since distilled water was used in the tests, the solute concentration is expected to be very low; hence, the osmotic suction should be negligible. The total suction in the above relation is therefore reduced to matric suction. Note that this assumption is also commonly used by other researchers (Dao et al. 2011; Delage and Cui 2008; Patil et al. 2017; Rowe 2012).The matric suctions corresponding to the three values of RH imposed at 23 °C and computed from Eq. (4-1) are reported in Table 4.1

Table 4.1 Suction imposed by means of the different saturated saline solutions at 23 °C

Saturated salt solutions	Relative humidity RH (%)	Suction (MPa)
KCH_3CO_2	23	201
NaCl	75	39
K_2SO_4	97	4

Before and after every triaxial test, moisture content of specimen has to be measured in order to evaluate the water loss during the tests, considering the tests were not performed in a humidity-controlled environment and lasted nearly thirty minutes. This verification confirms the nearly zero evolution of water content during the whole triaxial test. Hence, suction of the specimens can be considered to stay constant during the whole test.

4.2.3 Experimental apparatus

Triaxial compression tests were performed with the electro-mechanical press (Z020TN, Zwick Roell, Ulm, Germany). The accuracy of the press sensor was about ±20 N for the axial load and ±2 µm for its displacement. Deformations were measured using a home-designed measuring system which is illustrated in Fig 4.4.

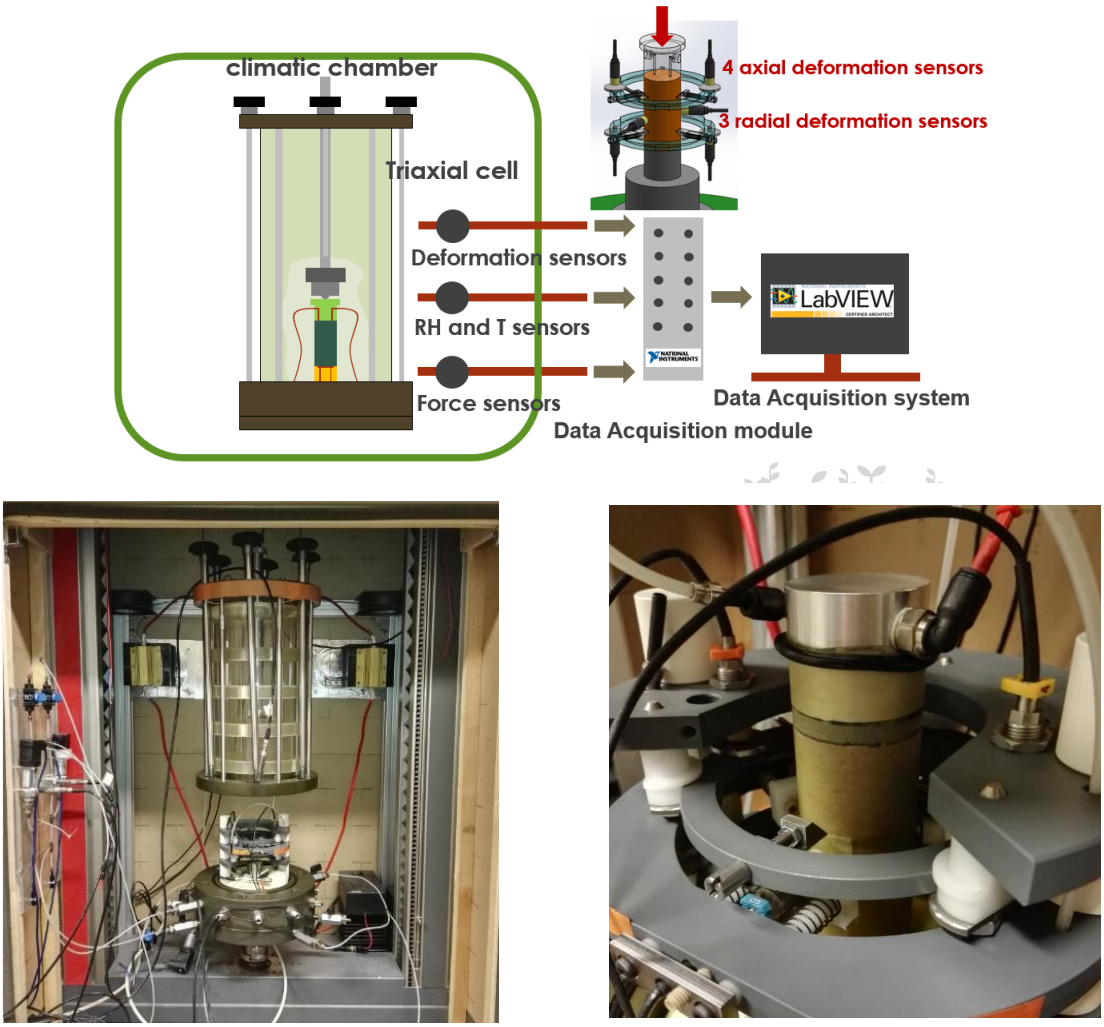

Figure 4.4 Home designed experimental apparatus for loading-unloading triaxial tests

Four non-contact sensors (accuracy of 0.4 μm) were installed at 1/3 and 2/3 of specimen's height, to measure the axial deformation; meanwhile, three non-contact sensors were placed at the middle plane of the specimen with the included angle of 120° to measure the radial deformation. Combining the axial and radial deformation, the volume changes during triaxial tests can be deduced. A special climatic chamber was built to contain the triaxial cell and electric heater which allowed to maintain temperature at 23 °C, the same as that during curing. Two temperature sensors were placed in the cell and the chamber separately to monitor thermal change. All the sensors (including loading, deformation and temperature) were integrated in LabVIEW ensuring an automatic data acquisition.

4.2.4 Loading method

The confining pressure is imposed by compressed air. Two types of mechanical loadings were applied at constant relative humidity conditions, as illustrated in Figure 4.5. The first loading type is a classical drained triaxial test: loading is applied at constant speed until failure. Here,

it should be noticed that despite the qualification "drained test", there is no water flowing out from the specimens and the excess air pressure remains zero all the time. After measuring the maximum deviator stress at failure for one particular specimen, noted f_c in the following sections, the second loading type consisting of loading–unloading cycles at prescribed stress levels, respectively 20%, 40%, 60% and finally 80% of f_c was conducted with two other specimens prepared under identical conditions as the first one. The loading cycles were implicitly assumed to have no impact on the unconfined compressive strength. In addition, unloading-reloading cycles are assumed not to generate any irreversible strains, so that they can be used to estimate Young's modulus E and the irreversible plastic strain ε_{res}, (hereafter named as the residual strain). One of the objectives of this paper is to investigate the evolution of these two parameters with the level of axial stress applied (in this study, 20%, 40%, 60% and finally 80% of f_c). Young's modulus E is therefore computed from the following equation:

$$E = \frac{\Delta\sigma_{xx}^{cycle}}{\Delta\varepsilon_{xx}^{cycle}} \tag{4-2}$$

where $\Delta\sigma_{xx}^{cycle}$, $\Delta\varepsilon_{xx}^{cycle}$ are the differences respectively of the axial stress and axial strain between the maximal and minimal a load cycle.

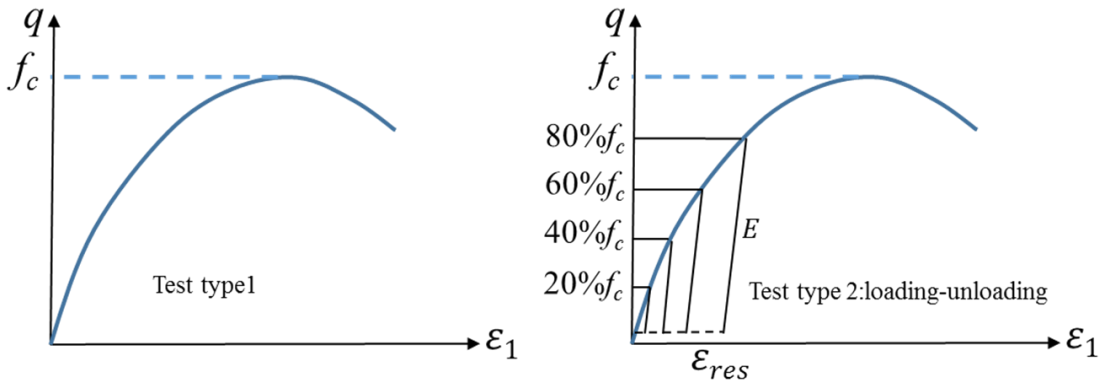

Figure 4.5 Schematic diagram of two types of mechanical loadings

The loadings were applied by imposing a constant axial displacement rate of 0.002 mm/s (corresponding to 0.003%/s) in loading and unloading. Before the commencement of each test, a pre-loading up to 100 N was applied for sample mounting. This value was chosen to be far lower than the strength of the tested material in order to minimise its effects.

4.3 Experimental Results

In summary, nature crude earth Lim was mixed with fine sand to reduce its clay content, thereby obtaining two types of artificial soil, named Mix1 and Mix2, with clay contents of 17% and 26% respectively. A series of triaxial tests incorporating loading-unloading cycles were

conducted at three relative humidities (23%, 75%, and 97%) and three confinement pressures (0 kPa, 100 kPa and 600 kPa). A global experimental arrangement is shown in Figure 4.6.

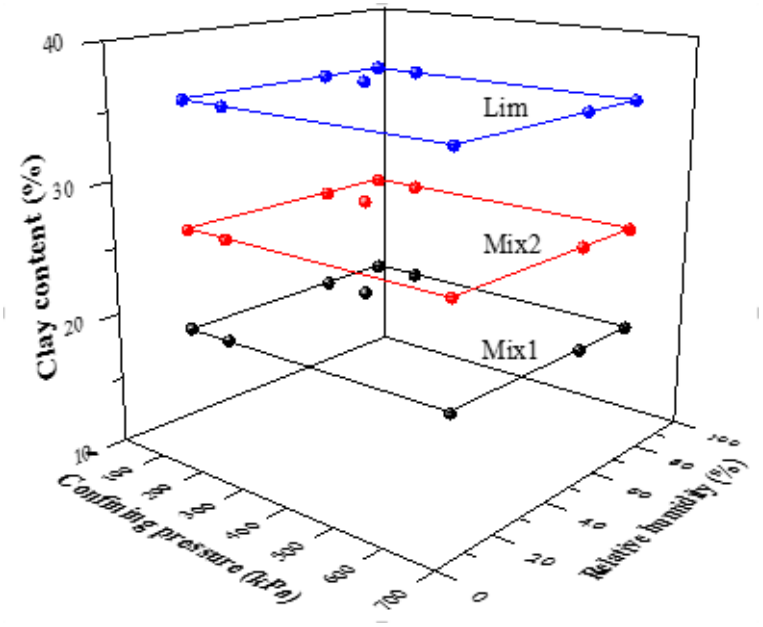

Figure 4.6 Schematic diagram of experimental arrangement considering various impact factors

4.3.1 Experimental repeatability

For every combination of the controlling parameters (RH, confining pressure), three tests are conducted under identical conditions to verify repeatability. Figure 4.7 here below showing the evolution of deviator stress and volumetric strain versus axial strain is a particular example of such test results obtained on Mix1 at 75%RH and 100kPa confining pressure. As can be seen, the results show good repeatability. This verification gives confidence on the reliability of the experimental device and the system of measurements.

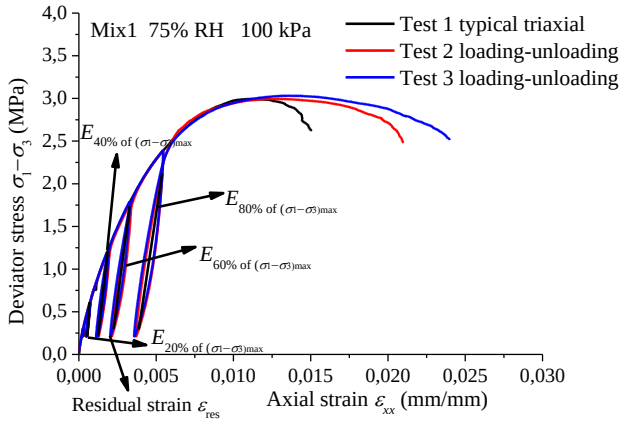

a

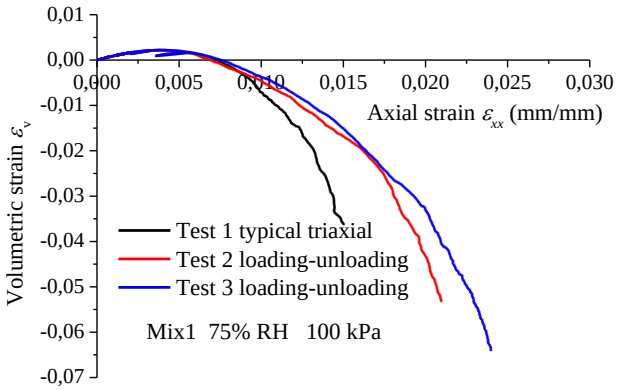

b

Figure 4.7 Evolution of deviator stress (a) and volumetric strain (b) versus axial strain during loading and unloading for Mix1 at 75% RH, 100 kPa confining pressure

4.3.2 Influence of relative humidity on loading-unloading shear behaviour

Stress-strain and volumetric behavior

Figure 4.8 shows the evolution of stress-strain behavior at 3 given values of relative humidity (23%, 75% and 97%) and at a confining pressure of 100 kPa for all the 3 soils tested. It can be observed that an increase of relative humidity induces a significant reduction of shear strength f_c, while the residual strain (defined as strain after unloading) becomes larger. Moreover, it is interesting to notice that the soil Lim with the highest clay content (35%) changes from a relatively brittle behaviour at low RH (23% RH) to a more ductile behaviour at high RH (97%). However, this transition from brittle to ductile behaviour is not observed for the other two soils, with lower clay contents (26% and 17%). The above remarks also apply for other tests at 0 kPa and 600 kPa confinement conditions.

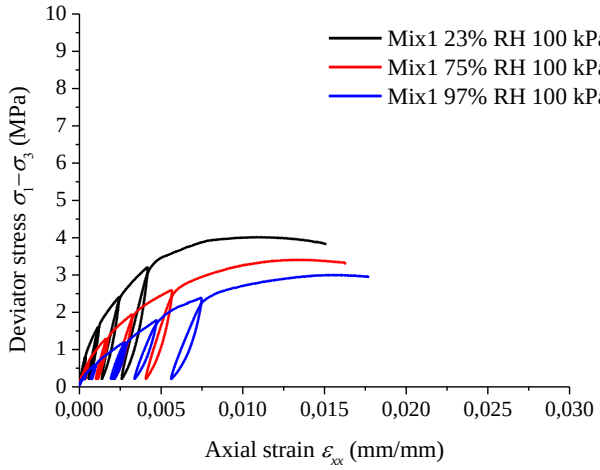

(a) Mix1

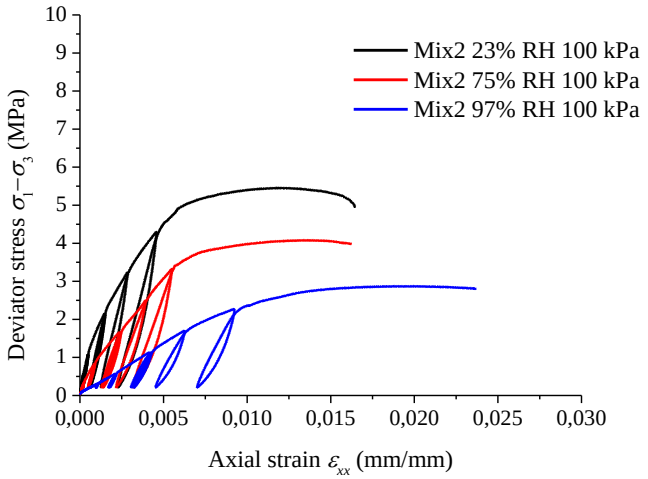

(b) Mix2

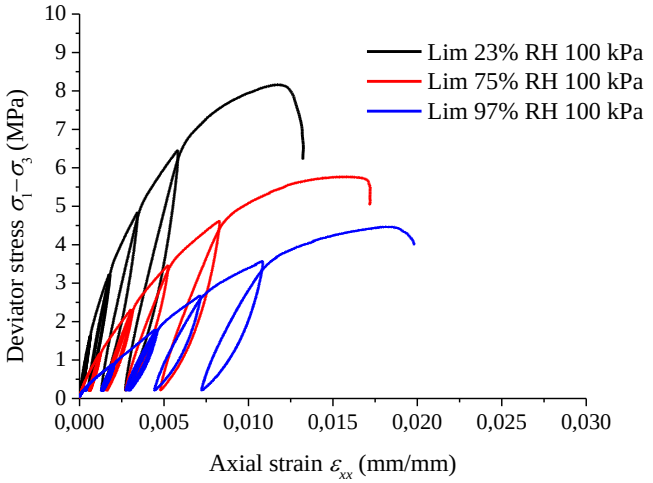

(c) Lim

Figure 4.8 Stress–strain behavior at given relative humidity and 100 kPa confining pressure for Mix1, Mix2 and Lim

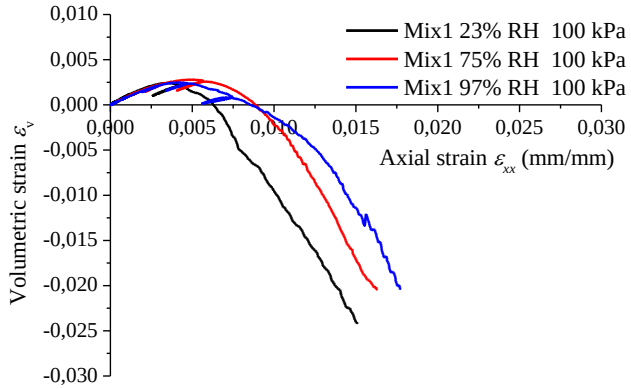

(a) Mix1

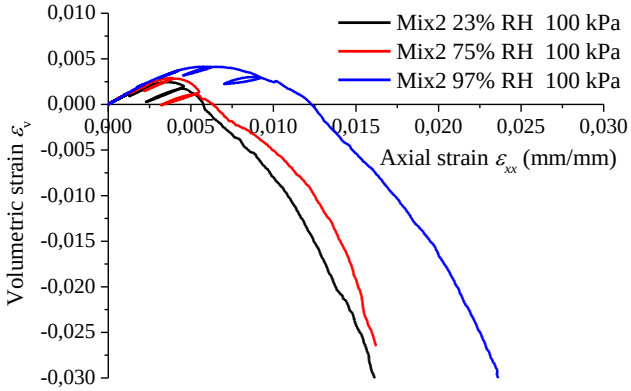

(b) Mix2

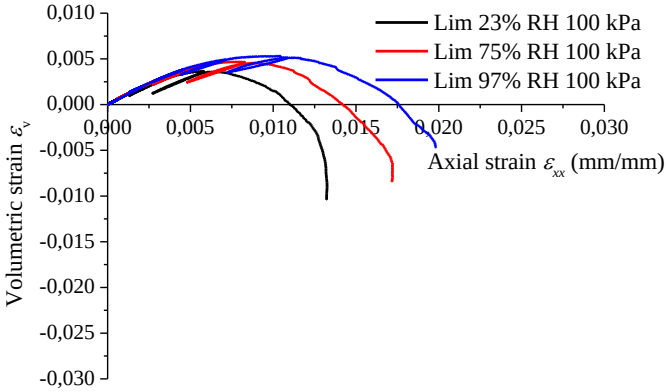

(c) Lim

Figure 4.9 Volumetric evolution versus axial strain at given relative humidity and 100 kPa confining pressure for Mix1, Mix2 and Lim

The volumetric variation is shown in Figure 4.9. It is observed that for all the test conditions investigated, the samples exhibit an initial phase of contraction, followed by a second dilatant phase. In addition, the contractive volume change, being in all cases smaller than 0.5%, seems not very sensitive to variations of relative humidity. On the other hand, the transition point separating the contractant and dilatant behaviors does depend on relative humidity. For example, at 23% RH, this transition point appears after the cycle of 80% of f_c, while at 97% RH, this transition occurs around 60% of f_c. Moreover, Lim presents a comparatively larger contraction and a smaller dilation; whereas the opposite is observed for Mix1 and Mix2. One possible explanation of this observation could be the difference in their particle size distributions.

The higher percentage of fines (clay and silt) in Lim is possibly the cause of a larger initial contraction, which delays the occurrence of the dilatant phase hence reduces its amplitude. By comparison, the higher percentage of sand, in a well compacted state (optimum Proctor), in Mix1 and Mix2 (both more than 40%) probably reduces the initial volume contraction. Note that specimens used in this research are well compacted (with high dry density 1.95 g/cm^3); with the soil particles relatively interlocked and possess little freedom of movement. When subject to shear stress, sliding can only occur when neighboring particles "climb" over each other, which therefore induces a dilative volume change. All the tendencies mentioned above are also observed at both 0 kPa and 600 kPa confining pressures.

Failure strength, Young's modulus E and residual strain

Figure 4.10 illustrates the variations of failure strength with relative humidity for the three different soils under three confining pressures (0 kPa, 100 kPa and 600 kPa). As stated in the stress-strain behavior, an increase of relative humidity induces a significant reduction of failure strength f_c for all the 3 soils tested, with different amplitudes for each. Take the case of 100 kPa confining pressure for example. For Mix1 with 17% clay content, when relative humidity increases from 23% to 97 %, the shear strength f_c decreases from 4.01 MPa to 2.99 MPa, hence a 25% reduction. Comparatively, for Lim with a higher clay content (35%), the corresponding reduction from 8.12 MPa to 4.47 MP amounts to 45%, which is substantially higher. Therefore, the sensitivity of shear strength relative to changes of RH depends on clay content. Moreover, the shear strength f_c itself is also influenced by the clay content. This last issue will be further discussed in the following sections. Last but not least, a rise of confining pressure also induces strength increase, which is consistent with previous findings reported by other researchers.

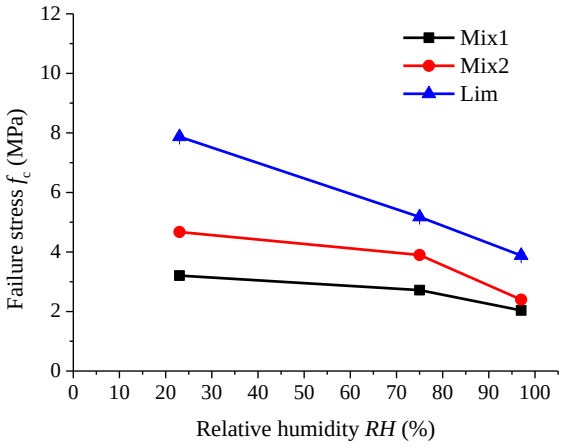

(a) 0 kPa

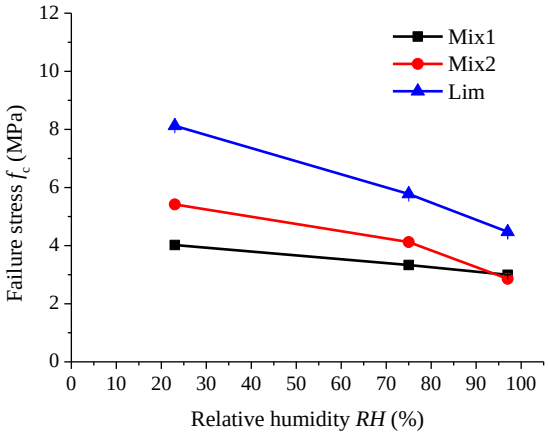

(b) 100 kPa

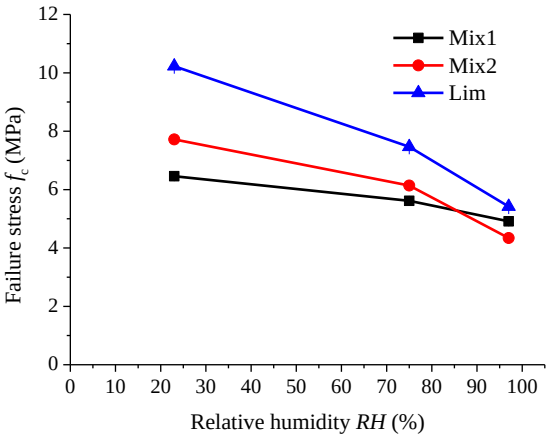

(c) 600 kPa

Figure 4.10 Failure strength of Mix1, Mix2 and Lim as a function of relative humidity under different confinement conditions

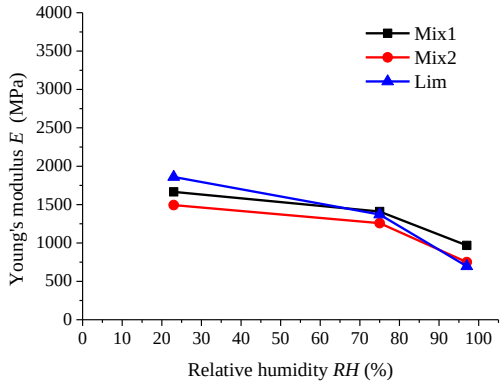

(a) 0 kPa

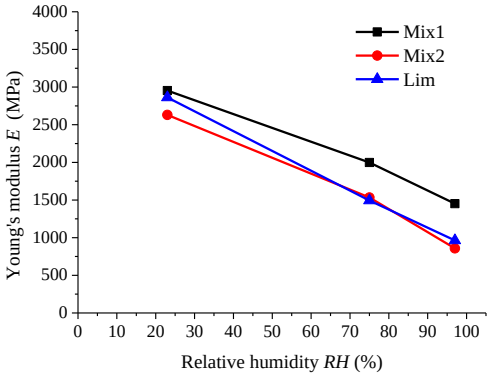

(b) 100 kPa

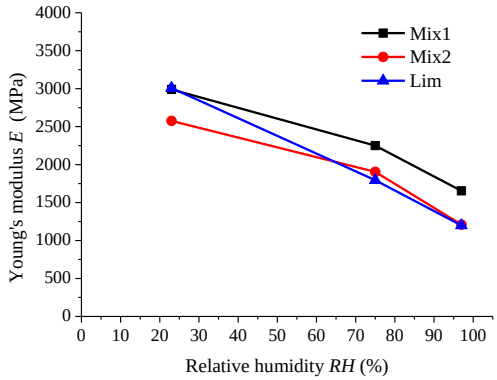

(c) 600 kPa

Figure 4.11 Evolution of Young's modulus E through "20% of f_c" cycle for Mix1, Mix2 and Lim under different confinement conditions

Figure 4.11 shows the evolution of Young's modulus with relative humidity. To be precise, the Young's modulus in this figure refers to the value deduced from measurements during the unloading-reloading cycle at 20% f_c. Consistently with the case of shear strength, Young's modulus E also decreases drastically with the rise of relative humidity. For example, when RH increases from 23% to 97%, Young's modulus E would exhibit a 50% degradation or more. Contrary to the case of shear strength however, the degradations are of similar amplitudes of for all the three soils, especially for the case of 100 kPa confining pressure.

Like Young's modulus E, the residual strain ε_{res} is also computed from unloading-reloading cycles at 20% f_c. Figure 4.12 reports its value versus relative humidity. Similarly to stress-strain behavior, there is a significant increase of residual strain ε_{res} with the rise of relative humidity. It is interesting to note that ε_{res} increases only slightly from 23% to 75% RH, but much more significantly from 75% to 97% RH. This possibly indicates the existence of a threshold value

for the moisture content in terms of deformability. This issue will be further investigated in future work by performing experiments at other values of RH.

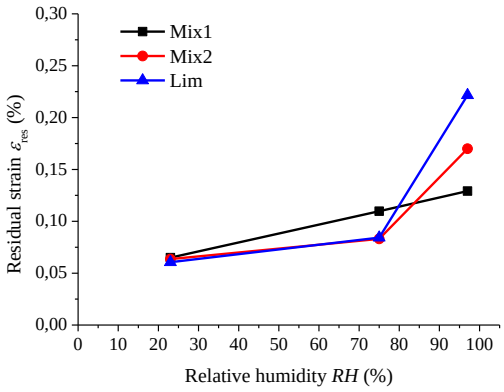

(a) 0 kPa

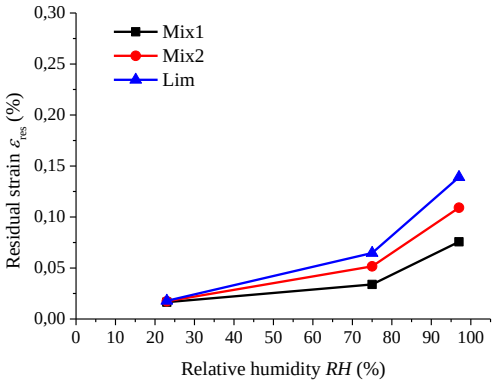

(b) 100 kPa

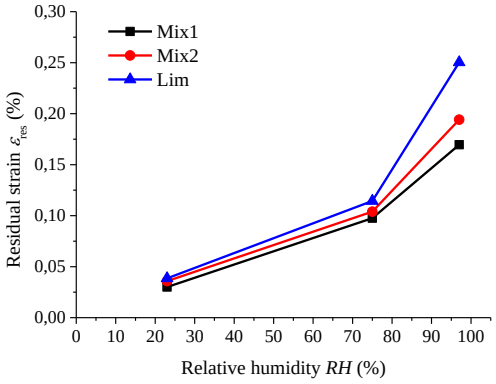

(c) 600 kPa

Figure 4.12 Evolution of residual strain ε_{res} through "20% of f_c" loading-unloading cycle for Mix1, Mix2, Lim under different confinement condition

4.3.3 Influence of clay content on loading-unloading shear behaviour

Failure strength and Young's modulus *E*

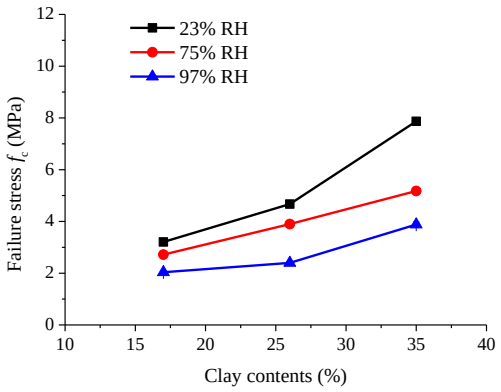

(a) 0 kPa

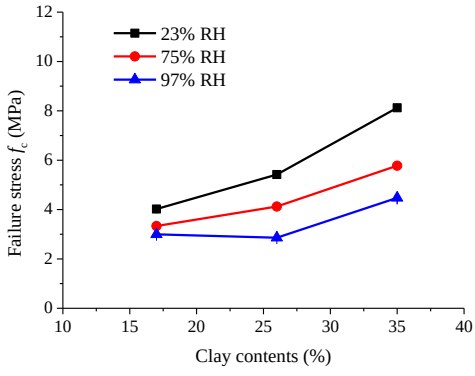

(b) 100 kPa

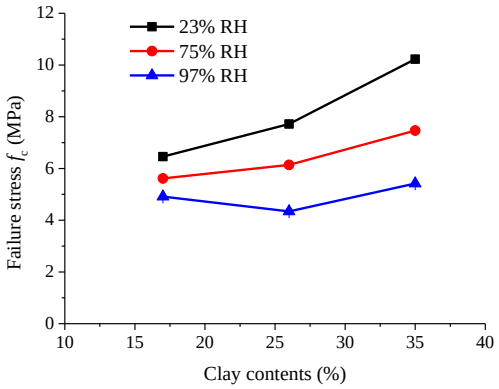

(c) 600 kPa

Figure 4.13 Failure strength as a function of clay content under different confinement conditions and relative humidity

As previously shown in Figure 4.10, both the magnitude of f_c and its sensitivity relative to changes in RH depend on clay content. This dependency is discussed more precisely here by plotting the evolution of failure strength directly versus clay content in Figure 4.13. This is done for each confining pressure and relative humidity. It can be seen that failure strength f_c globally increases with the rise of clay content. However, the amplitude of this increase appears to be affected by relative humidity. For example, at 100 kPa confining pressure and 97% RH, as clay content increases from 17% to 35%, failure strength f_c rises from 2.99 MPa to 4.47 MPa, hence an amplification of 50%. Comparatively, for the same confining pressure but at 23% RH, the corresponding increase from 4.02 MPa to 8.12 MPa corresponds to a much larger amplification of 102%. A similar trend is also observed for 0 kPa and 600 kPa confinement condition. At a high RH of 97%, hydraulic degradation on f_c dominates, and an increase of clay content does not necessarily lead to strength increase or when that is the case, the amplitude tends to be much less significant. These tendencies are consistent with the fact that clay content and RH act as two independent factors. Clay bridges bind adjacent sand particles together and a minimum amount of clay is needed to provide an adequate number of bridges so as to effectively "constraint" the skeleton of sand particles. On the other hand, the clay bridges themselves need to possess an adequate strength which is controlled by suction via the RH. This is why the benefit of increasing clay content tends to insignificant at very high RH.

Figure 4.14 shows the evolution of Young's modulus E with clay content, deduced from unloading-reloading cycle at "20% fc". Contrary to shear strength, there is no consistent relationship between Young's modulus and clay content. In any case, the variation of E induced by clay content is no more than 20% for all cases. Hence, considering the precision of

experimental measurements, it could be regarded that Young's modulus E is not sensitive to clay content. Note that this finding is consistent with the research on clay plasters (Taylor et al. 2006).

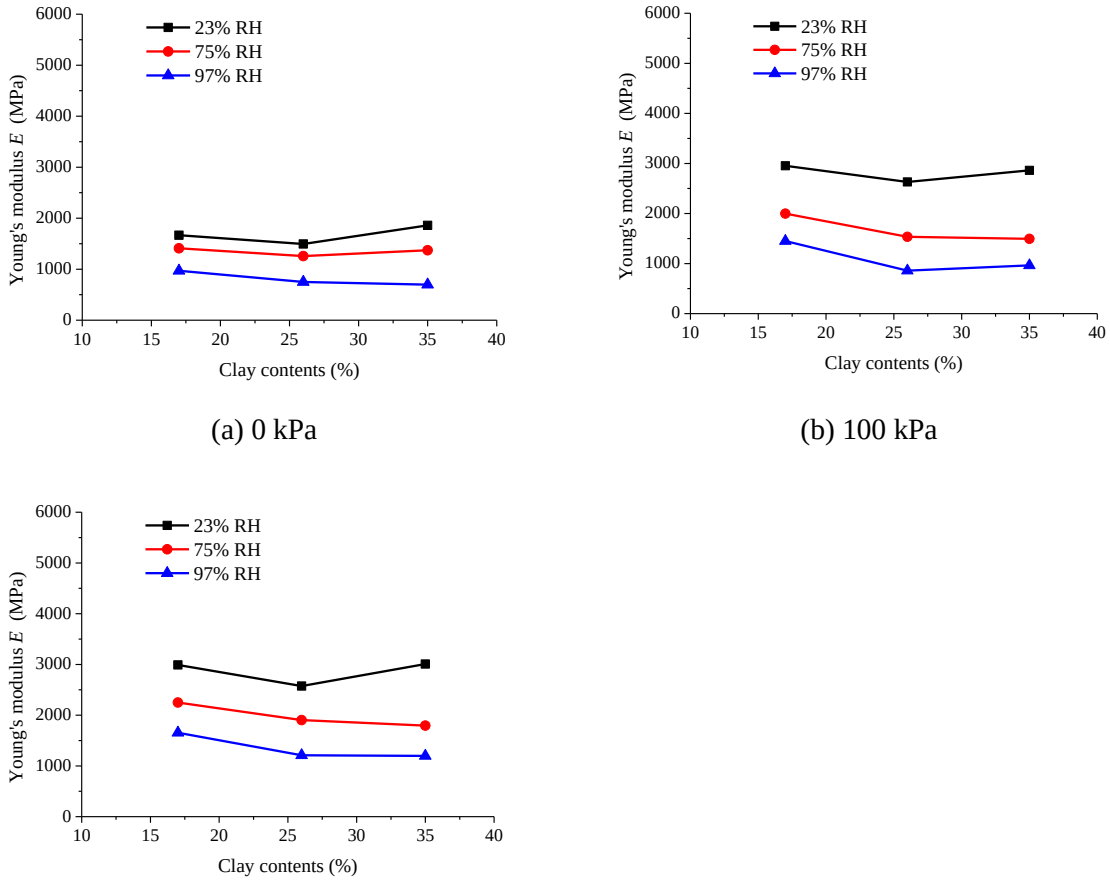

(a) 0 kPa

(b) 100 kPa

(c) 600 kPa

Figure 4.14 Young's modulus E as a function of clay content through "20% of f_c" cycle under different confinement conditions and relative humidity

Residual strain ε_{res}

Figure 4.15 shows the variations of Residual strain ε_{res} with clay content. Overall, ε_{res} is relatively insensitive to clay content at low RH (23%), increases slightly with the rise of clay content at the intermediate RH of 75%, except for 0 kPa confining pressure, due to experimental dispersion. It is interesting to note that at the high RH of 97%, the residual strain ε_{res} increases sensibly with clay content for all confinement conditions. This is probably because at high water content, the clay fraction becomes quite deformable hence the strong impact of clay content on deformability.

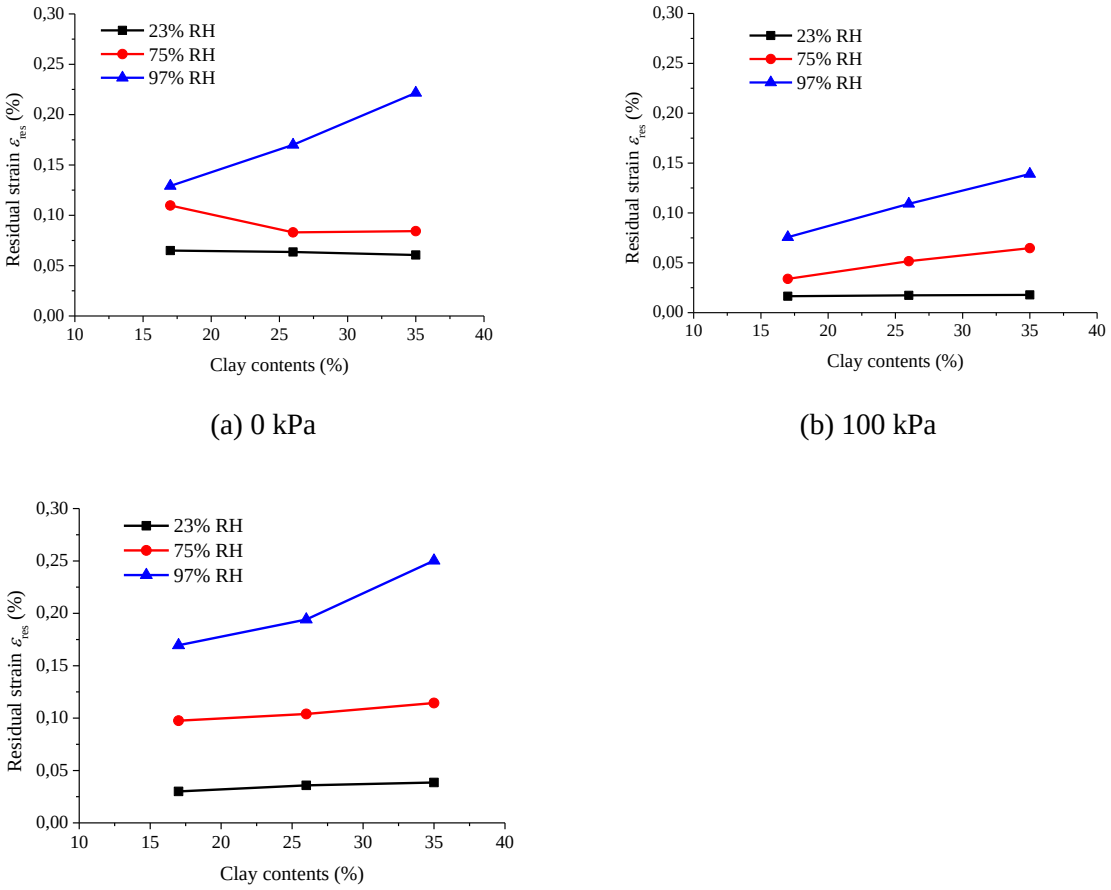

(a) 0 kPa

(b) 100 kPa

(c) 600 kPa

Figure 4.15 Residual strain ε_{res} as a function of clay content through "20% of f_c" cycle under different confinement conditions and relative humidity

4.3.4 Influence of stress level on the mechanical behavior

Results of evolution of Young's modulus *E* and residual strain versus stress level are shown in Figure 4.16. At the same stress level, Young's modulus *E* decreases with the rise of relative humidity while residual strain increase with the rise of relative humidity. This mentioned tendency is supportable for all the applied stress level (20%, 40%, 60% and finally 80% of f_c).

At constant relative humidity and confining pressure, a progressive degradation of Young's modulus *E* is observed with increasing applied stress. In addition, an obvious increase of residual strain is also observed from lower stress level to higher stress level in Figure 4.16. A similar tendency is also found for other experimental cases.

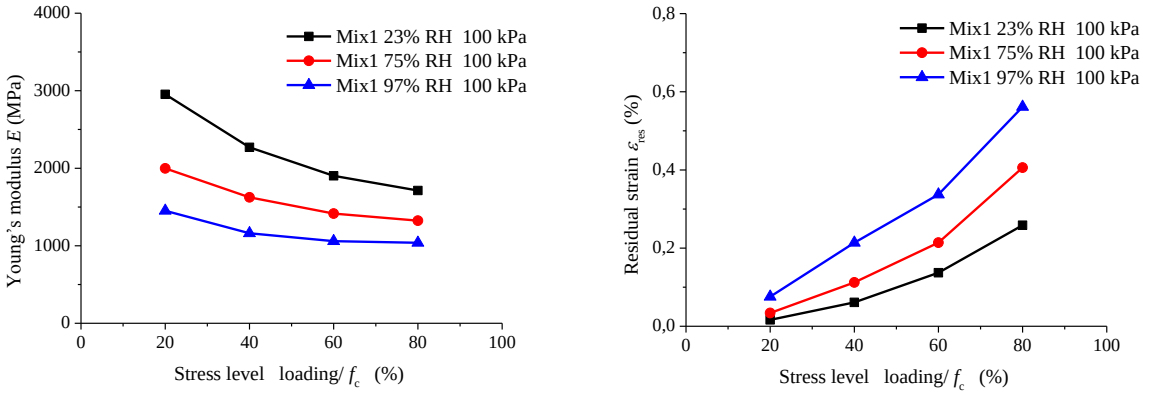

(a) Young's modulus E (b) residual strain

Figure 4.16 Evolution of Young's modulus E and residual strain versus stress level at different relative humidity and 100 kPa confining pressure for Mix1

4.4 Discussion

4.4.1 Generalized effective stress approach

By now, there are two main approaches to determine the shear strength of unsaturated soils: the independent state variables approach (Fredlund et al. 1978), and the effective stress approach (Bishop 1959). In comparison with independent state variables approach, the advantage of the effective stress approach is that the variation of shear strength with changes of total stress, pore water pressure and pore air pressure is linked to a single stress variable. As a result, this single stress variable enables a conversion of multiphase porous medium into mechanically equivalent single-phase continuum. However, a major difficulty of the effective stress approach lies on the determination of effective stress parameter χ.

As stated previously, one of the main objectives of the present study is to explore the possibility of obtaining a unified failure condition for samples subjected to different suctions and mechanical stresses using the existing tools of unsaturated soil mechanics. To this end, the experimental data is reinterpreted in the space of effective stresses in the sense of Bishop, defined via a particular choice of the parameter χ:

$$\sigma'_{ij} = (\sigma_{ij} - u_a\delta_{ij}) + \chi s\delta_{ij} \tag{4-3}$$

Under the condition of triaxial tests, the mean stress p, the mean effective stress p' and the deviatoric stress q are defined as follows:

$$p = \frac{1}{3}(\sigma_1 + 2\sigma_3) \tag{4-4}$$

$$p' = \frac{1}{3}(\sigma_1' + 2\,\sigma_3') = p + \chi s; \qquad q = \sigma_1 - \sigma_3 \tag{4-5}$$

4.4.2 Determination of the effective stress parameter χ

It is well known that the effective stress parameter χ strongly depends on the volumetric change in the soil. In this research, the classic Eq. (4-6), identifying the effective stress parameter with degree of saturation S_r (a volumetric parameter) was firstly applied on the experimental data.

$$\chi = S_r \tag{4-6}$$

Figure 4.17 presents two different plots of failure stress states for Lim soil, one in the (p-q) plane and the other in the (p'-q) plane, with p' and p linked by Eq. (4-6). Values of saturation degree S_r used are respectively 0.22, 0.43 and 0.66 for s=201MPa, s=39MPa and s=4MPa. The plot in the (p-q) plane shows a linear relationship at all three confining pressures (0 kPa, 100 kPa and 600 kPa) and for all suctions. However, the translation from p to p' using Eq. (4-6) does not lead to a unique failure line. Hence, the χ-function defined by Eq. (4-6) is not a good candidate and other functional forms were therefore explored.

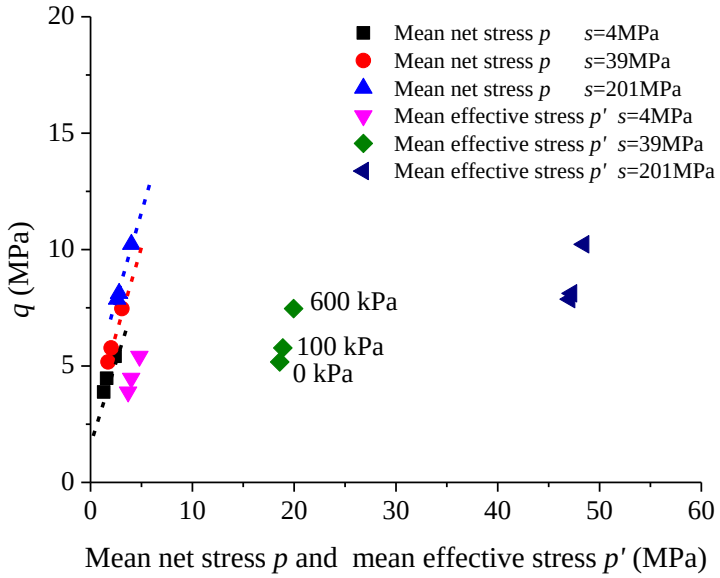

Figure 4.17 Translation from mean stress (p-q) plane to effective stress (p'-q) plane for Lim using Eq. (4-6)

The functional form (4-7) below firstly proposed by Khalili and Khabbaz (2002) has been reported to resulting in a unique failure envelope and was therefore investigated:

$$\chi = \begin{cases} \left(\frac{s_e}{s}\right)^{\alpha} & \text{if } s > s_e \\ 1 & \text{if } s \le s_e \end{cases} \tag{4-7}$$

where α is a positive coefficient and s_e represents the air-entry suction which ideally should be determined independently from water retention measurements. Due to the lack of experimental data in our case, these two parameters were determined together by a trial and error process, as described in detail in the following:

Failure points at a given suction are firstly plotted in the plane of mean net stress versus shear stress (p-q) where it is observed that they fall approximately on a straight line and that failure lines for different suctions are approximately parallel to each other hence of the same slope. The experimental data is then transformed from (p-q) to (p'-q) plane using Eq. (4-5) and (4-7). Since the deviatoric stress q is unaffected and the translation $s\chi(s)$ only depends on suction, this transformation therefore translates failure lines at a given suction horizontally as a rigid body. Invoking the classic result in unsaturated soil mechanics (Geiser et al. 2006; Nuth and Laloui 2008) that, for adequate functional forms of $\chi(s)$, the above transformation brings failure points for different suctions to a unique failure line crossing the origin, and on account of the observation in (p-q) plane, the target (i.e. the unified failure line) of the transformation is known. The required horizontal translation $s\chi(s)$ for each suction level in order for them to converge to the unified failure line can be determined graphically as shown in Figure 4.20, leading to the determination of $\chi(s)$for each particular suction. The functional form $\chi = (\frac{s_e}{s})^{\alpha}$ implies $\ln(\chi) = \alpha \ln(s_e) - \alpha\ln(s)$. Plotting $\ln(\chi)$vs $\ln(s)$ gives a straight line of slope α (as shown in Figure 4.18). A unique optimum value of $\alpha = 0.85$ was found for the three compacted soils used in this study, similar to the results reported by Khalili and Khabbaz (2002). Once α is determined graphically from the slope, we can then determine the value of s_e from the intercept.

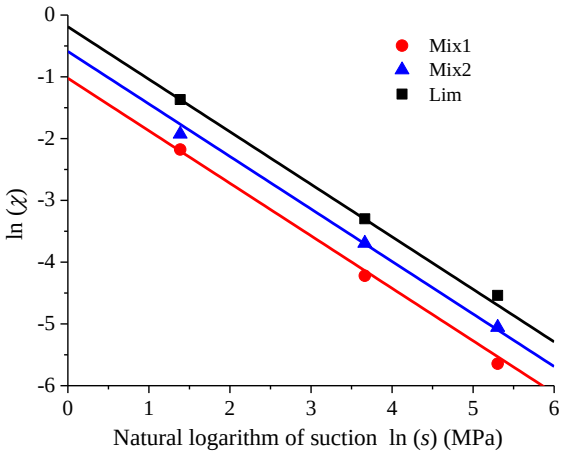

Figure 4.18 Relationships between $\ln(\chi)$ and $\ln(s)$for three types of soil

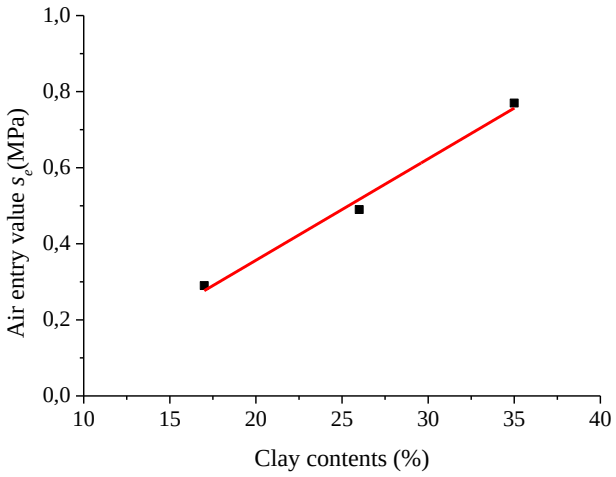

Figure 4.19 Variation of air-entry suction with changing clay content

Table 4.2 Coefficient values in χ-s function for three soils

	Clay mass content (%)	Coefficient α	Air-entry suction S_e (MPa)
Mix1	17	0.85	0.29
Mix2	26	0.85	0.49
Lim	35	0.85	0.77

For the air-entry suction determined and shown in Figure 4.19, it increases with increasing clay content, and a relatively good correlative linear fitting is observed for all the three types of soil. This observation is consistent with classic results like that of (Yang et al. 2004): a fine-grained soil had a comparatively high air-entry suction compared with a coarse-grained soil.

Figure 4.20 shows the translation from total stress interpretation plot to the new Bishop effective stress plot using Eq. (4-7) and parameters in Table 4.2. It can be seen that failure states plotted in the (p'-q) plane lie approximately on a single line crossing the origin, regardless of the matric suction and confining pressure. Moreover, it is interesting to notice that, the slope M of this failure state line varies slightly with changes of soil type (here related to clay content). For example, when clay content increases from 17% to 35%, M decreases from 1.85 to 1.65. In other words, higher is the proportion of sand added to the original Lim-soil, higher is the resulting friction angle. This is consistent with the classic observation that sands have higher friction angles than clays. In addition, the increase in effective stress $p' - p = s\chi(s)$, which reflects indirectly the increase in shear strength, increases clearly with increasing clay content. This indicates clearly that the sensitivity of shear strength relative to changes of RH depends on clay content.

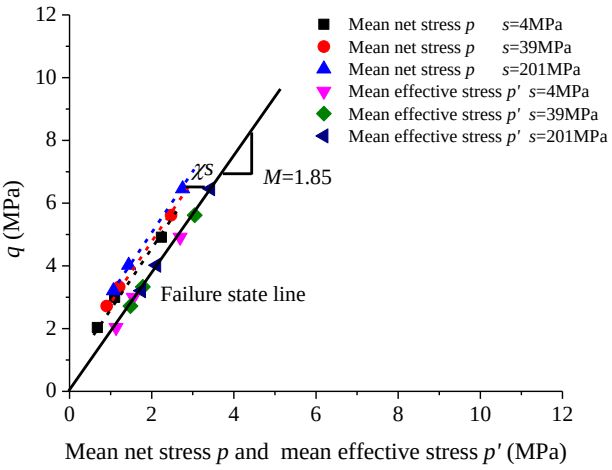

(a) Mix1

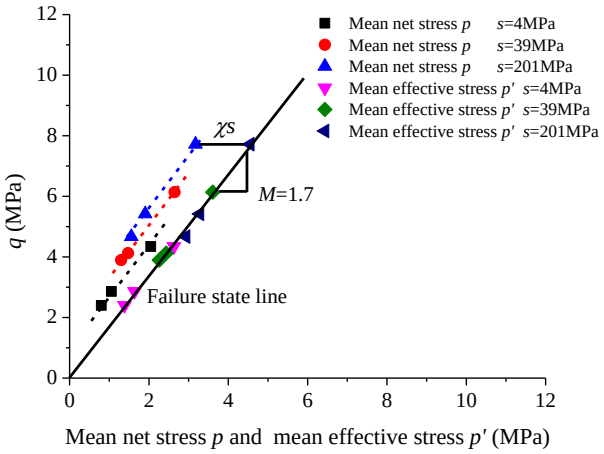

(b) Mix2

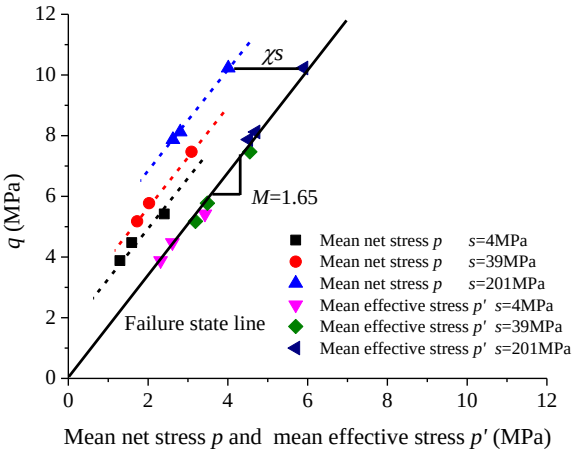

(c) Lim

Figure 4.20 (p-q) plane and (p'-q) plane under different suctions and confining pressures using Eq. (4-7) for three soils

4.5 Conclusion

Loading-unloading shear behavior of three types of earth with different clay contents was investigated at different relative humidities and different confining pressures. This study shows that the mechanical characteristics of earthen materials have a strong dependence on the ambient relative humidity at which the samples are conditioned, as well as on the clay content:

- Both the maximum deviator stress f_c and Young's modulus E measured from a loading-unloading cycle decrease with the increase of relative humidity. The amplitude of this reduction depends on the clay content.
- An increase of relative humidity leads to more ductile behavior, while a lower relative humidity induces brittleness. This tendency is sharper at high clay content. In parallel, there is an obvious increase of residual strain ε_{res} with the rise of relative humidity at the same stress level.
- The shear strength f_c increases with the rise of clay content (within the range of values investigated) at constant RH and confining pressure. Due to the softening action of water on clays, the amplitude of this amplification decreases with increasing relative humidity.
- Young's modulus E is relatively insensitive to changes in clay content considering that the variation of E is less than 20% for all cases.
- Residual strain ε_{res} increases slightly with the rise of clay content at 23% and 75% RH, but an important rise of ε_{res} occurs when RH increases to 97%.
- Increasing the applied stress induces a degradation of secant Young's modulus and an accumulation of residual strain.
- By considering the effective stress parameter χ as a function of suction s, a unified functional form $\chi(s)$ was found for all three soils with a unique value α=0.85, such that failure states of all samples plotted in the (p'-q) plane were observed to lie approximately on a unique failure state line crossing the origin, regardless of the matric suction and confining pressure.

Chapter 5
A poro-elastoplastic damageable constitutive model for compacted earth

5.1 Introduction

Results of our experimental investigation reported in Chapter 4 indicate that the basic mechanical behaviour of unsaturated earthen materials is characterized by irreversible plastic straining and stiffness degradation. The first behaviour is commonly modelled using classic elastoplasticity theory, despite its unrealistically prediction of a stiffness-discontinuity on the stress-strain curve at yield. To improve this, it is proposed to adopt the approach of Bounding Surface Plasticity (BSP). The stiffness degradation due to microcracks has not been considered in the literature on earthen materials. To address this second issue, it is proposed to follow the approach of continuum damage mechanics.

In this chapter, a new poro-elastoplastoplastic damageable constitutive model for earthen materials is presented for unsaturated earthen materials. It is based on the BSP theory and the effective stress concept. It adopts a non-associative flow rule and a simple radial mapping rule, and takes into account an isotropic damage. Plastic straining and damage evolution occur as two coupled processes. Both processes are affected by suction and this influence is accounted for in the new constitutive model. Finally, the performance of this model is investigated by comparing its predictions to the results from triaxial tests results on compacted earth samples at different hydraulic conditions and confining pressures.

5.2 A poro-elastoplastoplastic damageable constitutive model

The poroplastic mechanism in this new model follows the same approach as the CASMNS model developed by Lai et al. (2016) for unsaturated soils. The formulation is based on the concepts of effective stress and bounding surface plasticity theory. To accurately simulate volume changes (e.g. transition from compressibility to dilatancy), a state-dependent non-associative flow rule is used, by adopting the plastic potential of (H.-S. Yu 2007). The starting point is the definition of an effective stress to account for effects of partial saturation.

5.2.1 Partial saturation and effective stress

There are two main classical modelling approaches on partially saturated soils. All of them need two independent stress variables. The classic BBM model is based on net stress and suction whereas a few others use an effective stress and suction (Pereira et al. 2005; A R Russell and Khalili 2006; H. S. Yu and Khong 2003). Some recently appeared models proposed to use the degree of saturation instead of suction as a generalised stress variable (Zhang and Ikariya 2011;

Zhou et al. 2016; Zhou et al. 2018). This new approach seems to be promising, but the feedback is still limited. In this paper, we follow the approach based on an effective stress and suction.

At partially saturated states, the effective stress tensor σ'_{ij} can be expressed as (Bishop 1959):

$$\sigma'_{ij} = (\sigma_{ij} - u_a\delta_{ij}) + \chi s\delta_{ij} \tag{5-1}$$

where σ_{ij} is the total stress tensor, u_a is the pore air pressure, s is the difference between pore air and pore water pressure $(u_a - u_w)$, referred as matric suction, δ_{ij} is the second order identity tensor, and χ is defined as the effective stress parameter and generally is state dependent. Consistently with previous chapters, a prime (') above a stress variable will denote the effective stress counterpart. In many practical cases, air pressure can be identified as the atmospheric pressure, taken as the reference datum for stresses and fluid pressures, hence, Eq. (5-1) can be simplified to:

$$\sigma'_{ij} = \sigma_{ij} + \chi s\delta_{ij} \tag{5-2}$$

In this study, only the configuration of conventional triaxial tests is of concern, exhibiting cylindrical symmetry, hence axial and radial directions are always the directions of principal stresses and strains. Let σ_1 denotes the total axial stress, $\sigma_2 = \sigma_3$ the total radial stress, ε_1 the axial strain and $\varepsilon_2 = \varepsilon_3$ the radial strain. This cylindrical symmetry allows to work with bi-vectors instead of 3-vectors; however, the various transformations and stiffness matrices lose their symmetry. recall that the total stress (p, q) and the effective stress variables(p', q') are related by:

$$p' = p + \chi s; \qquad q' = q, \tag{5-3}$$

hence, we only need to refer to q in future.

Several definitions for χ have been proposed in the existing literature: some researchers identified the effective stress parameter χ with degree of saturation S_r (Gerard et al. 2015; Jennings and Burland 1962; Zhou et al. 2018); while others argued that χ should be a function of suction (Aitchison 1985);. In this study, the functional form below firstly proposed by (Khalili and Khabbaz 1998) has been adopted:

$$\chi = \begin{cases} (\frac{s_e}{s})^{\alpha} & \text{if } s > s_e \\ 1 & \text{if } s \leq s_e \end{cases} \tag{5-4}$$

where α is a material constant and s_e represents the air-entry suction which can be determined from water retention measurements.

It is a classic result that when the failure stress states are plotted in the stress space (p', q), with an adequately chosen function χ to be applied in the translation Eq. (5-3), they lie approximately on a unique line. Khalili and Khabbaz (1998) showed that this result is obtained for a large class of unsaturated soils for the functional form Eq. (5-4) with $\alpha = 0.55$. Based on our experimental results in chapter 4, the particular value $\alpha = 0.85$ appears to lead to the same result for the three different compacted earths studied, as recalled here-below in Figure 5.1 for the case of Lim. This value of α was adopted in the subsequant numerical studies.

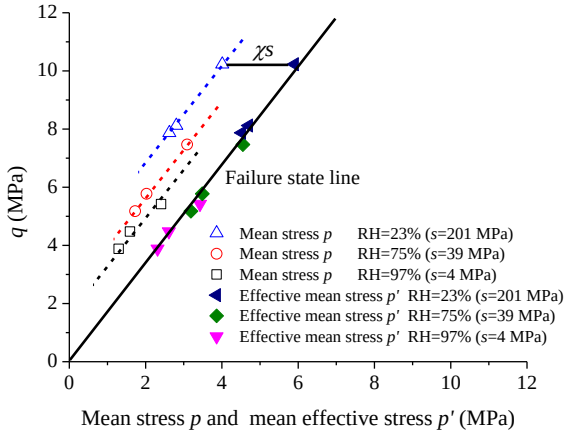

Figure 5.1 Failure states for Lim at different suctions and confining pressures before and after the translation using Eq. (5-3) and Eq. (5-4), demonstrating the unique failure line in the (p'-q) plane

For future manipulations, it is useful to introduce the following concise vectorial notations to denote axial/radial (i.e. principal) components and mean/deviatoric components:

$$\boldsymbol{\sigma}' = \begin{bmatrix} p' \\ q \end{bmatrix} \; ; \; \boldsymbol{\Sigma}' = \begin{bmatrix} \sigma_1' \\ \sigma_3' \end{bmatrix} \; ; \; \boldsymbol{\varepsilon} = \begin{bmatrix} \varepsilon_v \\ \varepsilon_q \end{bmatrix} \; ; \; \boldsymbol{E} = \begin{bmatrix} \varepsilon_1 \\ \varepsilon_3 \end{bmatrix} \tag{5-5}$$

where ε_v is the volumetric strain and ε_q is the deviatoric strain.

The mean/deviatoric effective stresses are linked to their axial/radial counterparts by the following relations (which evidently also holds for total stresses):

$$\boldsymbol{\sigma}' = \mathbb{A}\,\boldsymbol{\Sigma}'; \qquad \mathbb{A} = \begin{bmatrix} \frac{1}{3} & \frac{2}{3} \\ 1 & -1 \end{bmatrix} \tag{5-6}$$

The following equation holds for the conjugate strain components:

$$\boldsymbol{\varepsilon} = \mathbb{B}\,\boldsymbol{E}; \qquad \mathbb{B} = \begin{bmatrix} 1 & 2 \\ \frac{2}{3} & -\frac{2}{3} \end{bmatrix} \tag{5-7}$$

Within the framework of elastoplasticity, strains are supposed to be decomposable as the sum of an elastic (superscripts e) and a plastic component (superscripts p):

$$\boldsymbol{\varepsilon} = \boldsymbol{\varepsilon^e} + \boldsymbol{\varepsilon^p} \;;\; \boldsymbol{\varepsilon^e} = \begin{bmatrix} \varepsilon_v^e \\ \varepsilon_q^e \end{bmatrix} \;;\; \boldsymbol{\varepsilon^p} = \begin{bmatrix} \varepsilon_v^p \\ \varepsilon_q^p \end{bmatrix} \;;\; \boldsymbol{E} = \boldsymbol{E}^e + \boldsymbol{E}^p \tag{5-8}$$

For the damage mechanism, a damage variable D is introduced as an internal variable to simulate the effects of microcracks. For the sake of simplicity, only isotropic damage is considered here and $D \in (0,1)$ is a scalar variable.

5.2.2 General concept of Bounding Surface Plasticity

The concept of Bounding Surface Plasticity (BSP), also known as two-surface plasticity, was first originated by (Mroz 1967) and (Dafalias and Herrmann 1986; Dafalias 1986), and applied by Bardet (1986) and (H. S. Yu and Khong 2003) to soils. Russell and Khalili (2004) appear to be the first who applied the BSP theory to model unsaturated soils.

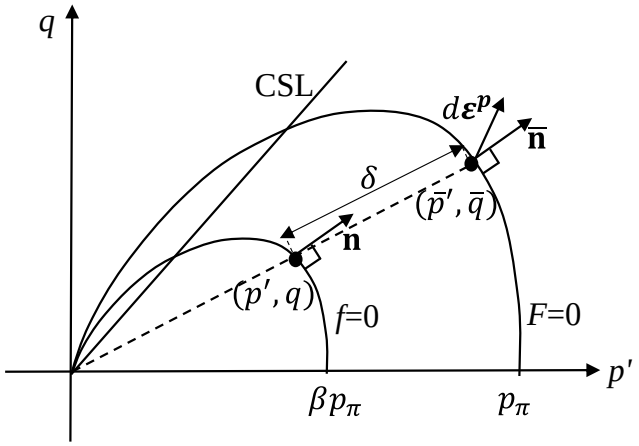

Figure 5.2 Bounding surface, Loading surface, and the radial mapping method

The major advantage of Bounding Surface Plasticity (BSP) theory is the ability to reproduce a progressive appearance of irreversible strains hence a smooth stress–strain behaviour at increasing loads, thereby avoiding an abrupt change predicted by classical elastoplastic models when yielding occurs. For this purpose, two surfaces are introduced generally: a Loading Surface (LS) $f = 0$ containing the current stress point $\boldsymbol{\sigma'}$ and a bounding surface (BS) $F = 0$. As loading increases so that the current stress point advances in the direction of the BS, inducing additional plastic strains, the BS itself evolves through a hardening mechanism that depends on the accumulated plastic strains. The central idea of BSP is that the plastic strain rate, which governs the rate of hardening hence the movement of the BS, depends on the distance separating the current and image stress point and the BS. The plastic strain rate is designed to be small at large distances from the BS and increases when approaching the latter. In order to define this "distance", it is necessary to define an image stress point $\bar{\boldsymbol{\sigma}}'$ on the BS. The "distance" in

question will then be the one separating $\boldsymbol{\sigma}'$and $\bar{\boldsymbol{\sigma}}'$**.** Among those mapping rules (giving $\bar{\boldsymbol{\sigma}}'$ as a function of $\boldsymbol{\sigma}'$), one frequently used is called "radial mapping" introduced by Dafalias due to its simplicity (Dafalias 1986). It consists of extrapolating the position vector linking the origin to the current stress $\boldsymbol{\sigma}'$ until it intersects the image stress $\bar{\boldsymbol{\sigma}}'$ on the Bounding Surface as illustrated in Figure 5.2.

5.2.3 Plastic and non-plastic mecanisms considering damage variable D.

Elastic mechanism accounting for damage

It is assumed that the loading surface always lies inside the bounding surface and that there is no "elastic domain" such that strain increments contain generally an elastic and a plastic component. To simplify, an isotropic elastic mechanism is adopted, commonly used in other constitutive models (Morvan et al. 2010; Russell and Khalili 2006; Wong et al. 2010):

$$d\boldsymbol{\varepsilon}^{\boldsymbol{e}} = \mathbb{C}^{e} d\boldsymbol{\sigma}' \tag{5-9}$$

$\mathbb{C}^{\boldsymbol{e}}$ is the elastic compliance matrix which is usually expressed in terms of the bulk and shear moduli *K* and *G*. To account for the effects of damage on the stress-dependent elastic properties, the following expressions are adopted based on the previous results of (T. A. Bui et al. 2016; Chiarelli et al. 2003; Mazars 1986):

$$\mathbb{C}^{\boldsymbol{e}} = \begin{bmatrix} \dfrac{1}{K(1-D)} & 0 \\ 0 & \dfrac{1}{3G(1-D)} \end{bmatrix} \quad ; \quad K = \frac{1+e_0}{\kappa}\, p' \quad ; \quad G = \frac{3(1-\nu)}{2(1+\nu)} K \tag{5-10}$$

where *D* is the isotropic damage variable, ν the Poisson ratio, κ a material constant, and e_0 the initial void ratio.

Bounding surface, loading surface and hardening mechanism

In this model, a whale-head shaped bounding surface (BS) is adopted. It writes:

$$F(\bar{p}', \bar{q}, p_\pi) = \left(\frac{\bar{q}}{M\bar{p}'}\right)^n + \frac{1}{\ln r} \ln\left(\frac{\bar{p}'}{p_\pi}\right) = 0 \tag{5-11}$$

In the above equation, *M* represents the slope of critical state line (CSL) in $p' - q$ plane, while n and r are two other model constants. The first constant n specifies the shape of the bounding surface and the second constant r is a space ratio used to control the intersection point of the CSL with the BS.Their influence on the bounding surface is shown in Figure 5.3.

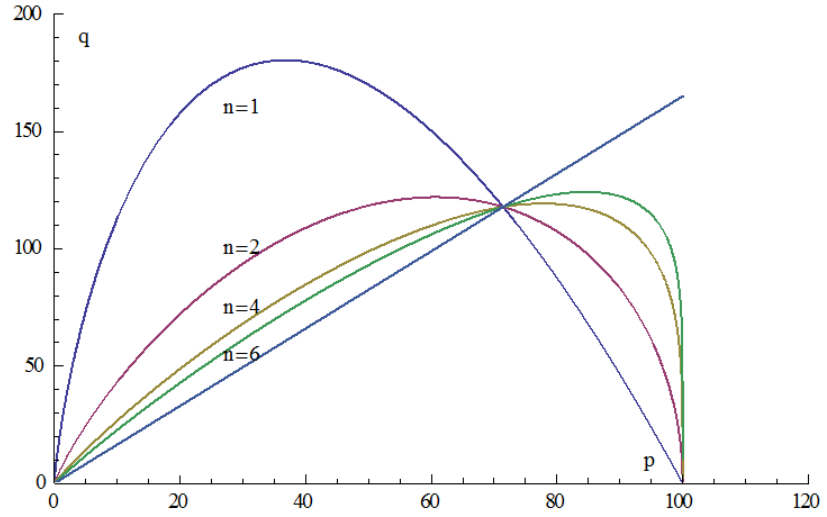

(a)

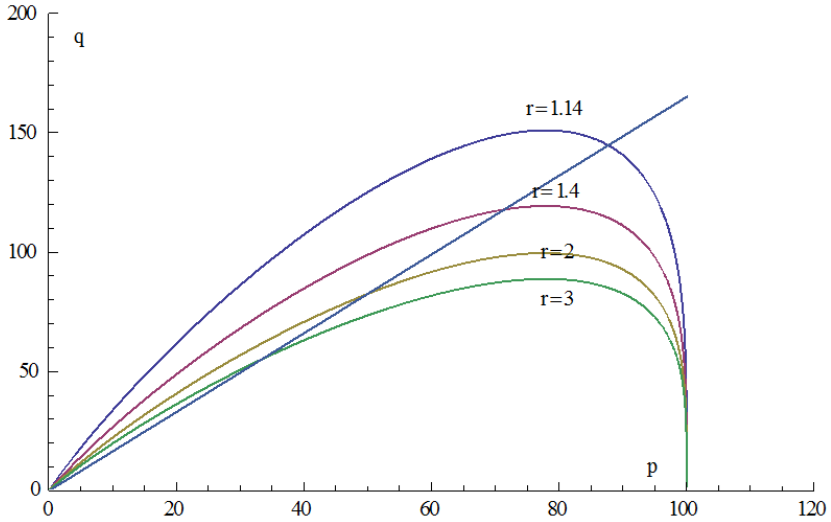

(b)

Figure 5.3 Bounding surface on the response of parameter: (a) n and (b) *r*

p_π is a variable analogue to the preconsolidation pressure in the classic Cam Clay model that determines the current size and position of the Bounding Surface. For simplicity, the Loading Surface (LS) is defined simply by homotheticity relative to the BS:

$$f(p', q, p_\pi) = \left(\frac{q}{Mp'}\right)^n + \frac{1}{\ln r}\ln\left(\frac{p'}{\beta p_\pi}\right) = 0 \tag{5-12}$$

After some simple manipulations, we obtain:

$$q = \beta\bar{q};\quad p' = \beta\bar{p}';\qquad \beta = \frac{p'}{p_\pi}\, r^{(\frac{\eta}{M})^n};\ \ \eta = \frac{q}{p'} = \frac{\bar{q}}{\bar{p}'} \tag{5-13}$$

where β is the scale factor between the BS and the LS, $\beta \in (0,1)$, and η is the stress ratio.

An isotropic hardening mechanism based on the Cam Clay model is applied here. In the presence of suction and damage effects, the preconsolidation pressure, noted p_π , is assumed to take the following form, inspired from previous work (Pereira et al. 2005; Shao et al. 2006):

$$p_\pi(\varepsilon_v^p, s, D) = (1 - D)(1 + k_1 \times l(s))p_0(\varepsilon_v^p) \tag{5-14}$$

In the above relation, $(1 - D)$ represents a softening effect due to damage, whereas the other factor $(1 + k_1 \times l(s))$ accounts for suction-hardening, k_1 being a model constant and the function $l(s)$ is defined in Eq. (5-17) here-below. At positive suction, the pre-consolidation pressure at full saturation p_0 is supposed to vary with the plastic volumetric strain according to the following relation:

$$dp_0 = \frac{1 + e_0}{\lambda(s) - \kappa} p_0 \, d\varepsilon_v^p \tag{5-15}$$

The suction-dependent coefficient of virgin (i.e. elastoplastic) compressibility $\lambda(s)$ is assumed to take the following form:

$$\lambda(s) = \lambda_0 - k_2 \times l(s) \tag{5-16}$$

Here, λ_0 is the limiting value of $\lambda(s)$ at full saturation, and κ is the elastic coefficient of compressibility, assumed suction-independent. The function $l(s)$ plays an important role here and must be chosen properly, ensuring continuity at full saturation. The following form for $l(s)$ is adopted in this work:

$$l(s) = \begin{cases} \dfrac{s}{s_e}\chi - 1 & if\ s > s_e \\ 0 & if\ s \le s_e \end{cases} \tag{5-17}$$

where the suction-dependent effective stress parameter χ is defined in Eq. (5-4).

Plastic potential and non-associative flow rule

The dilatancy, defined as the ratio between the plastic volumetric strain increment and the equivalent plastic deviatoric strain increment, has an important influence on the soil behaviour. This state-dependent parameter can be incorporated in the definition of the plastic potential. In the present model, the following stress-dependent relation proposed by Yu is adopted (H.-S. Yu 2007):

$$\frac{d\varepsilon_v^p}{d\varepsilon_q^p} = \frac{M^n - \eta^n}{m\eta^{n-1}} \tag{5-18}$$

In the above equation, *m* is another model constant which governs the plastic potential. This equation implies the dilatancy depends only on the stress ratio and becomes zero at the critical

stress ratio $\eta = M$. A plastic flow rule which satisfies the above dilatance ratio can be written as:

$$d\boldsymbol{\varepsilon}^p \overset{\text{def}}{=} \begin{pmatrix} d\varepsilon_v^p \\ d\varepsilon_q^p \end{pmatrix} = d\lambda\, \boldsymbol{m} = d\lambda \begin{pmatrix} m_p \\ m_q \end{pmatrix} \tag{5-19}$$

where $\boldsymbol{m}$ is a unit vector with components obtained from Eq. (5-18):

$$m_p = \frac{M^n - \eta^n}{\sqrt{(M^n - \eta^n)^2 + (m\eta^{n-1})^2}} \;;\; m_q = \frac{m\eta^{n-1}}{\sqrt{(M^n - \eta^n)^2 + (m\eta^{n-1})^2}} \;; \tag{5-20}$$

and $d\lambda$ is the plastic multiplier to be determined from the consistency condition (see (5.24)).

In this study, plastic flow is coupled with damage evolution under a general loading condition. Therefore, the plastic strain rate and damage evolution rate have to be determined simultaneously. The consistency condition on the bounding surface requires:

$$dF = \frac{\partial F}{\partial \bar{p}'} d\bar{p}' + \frac{\partial F}{\partial \bar{q}} d\bar{q} + \frac{\partial F}{\partial \varepsilon_v^p} d\varepsilon_v^p + \frac{1}{\sigma_0}\frac{\partial F}{\partial D}(\sigma_0 dD) + \frac{\partial F}{\partial s} ds = 0 \tag{5-21}$$

The reference stress $\sigma_0 = 1$ MPa has been added to make the dimension of different terms homogeneous. The plastic volumetric strain rate have already been defined in Eq. (5-19) and the damage evolution rate dD will be defined in Eq. (5-34). The above equation can be recast into a slightly more compact form by normalising the pseudo-gradient of the BS. The following notation is introduced:

$$\widetilde{\nabla} F = \left(\frac{\partial F}{\partial \bar{p}'}, \frac{\partial F}{\partial \bar{q}}, \frac{\partial F}{\partial s}, \frac{1}{\sigma_0}\frac{\partial F}{\partial D}\right)^T \;;\; \overline{\mathbf{n}} = (\overline{\mathrm{n}}_p, \overline{\mathrm{n}}_q, \overline{\mathrm{n}}_s, \overline{\mathrm{n}}_D)^T = \frac{\widetilde{\nabla} F}{\left\|\widetilde{\nabla} F\right\|} \tag{5-22}$$

where $\widetilde{\nabla}$ is a pseudo-gradient operator and $\|.\|$ represents the classic Euclidean norm of a vector. Similarly, the pseudo-gradient and the associated unit vector for the LS can be defined:

$$\widetilde{\nabla} f = \left(\frac{\partial f}{\partial p'}, \frac{\partial f}{\partial \mathrm{q}}, \frac{\partial f}{\partial s}, \frac{1}{\sigma_0}\frac{\partial f}{\partial D}\right)^T \;;\; \mathbf{n} = (\mathrm{n}_p, \mathrm{n}_q, \mathrm{n}_s, \mathrm{n}_D)^T = \frac{\widetilde{\nabla} f}{\left\|\widetilde{\nabla} f\right\|} \tag{5-23}$$

The classic assumption that stress increments at the current stress point and at the image stress point give the same plastic multiplier allows to write (Dafalias 1986):

$$d\lambda = \frac{\mathrm{n}_p dp' + \mathrm{n}_q dq + \mathrm{n}_D \sigma_0 dD + \mathrm{n}_s dS}{H} = \frac{\overline{\mathrm{n}}_p d\bar{p}' + \overline{\mathrm{n}}_q d\bar{q} + \overline{\mathrm{n}}_D \sigma_0 dD + \overline{\mathrm{n}}_s ds}{H_b} \tag{5-24}$$

where H is plastic modulus on the loading surface, and H_b the plastic modulus on the bounding surface.

When the current stress point is on the BS, hence coinciding with its image stress point, the combination of the Eqs. (5-19), (5-21),(5-22) and (5-24) leads to the following expression of the plastic modulus:

$$H_b = -\frac{1}{\left\|\widetilde{\nabla}F\right\|}\frac{\partial F}{\partial \varepsilon_v^p}m_p = -\frac{1}{\left\|\widetilde{\nabla}F\right\|}\frac{\partial F}{\partial p_\pi}\frac{\partial p_\pi}{\partial p_0}\frac{\partial p_0}{\partial \varepsilon_v^p}m_p \tag{5-25}$$

At this point, we will introduce the simplifying assumption that suction will remain constant, $ds = 0$, which corresponds to the experimental conditions. Combining Eqs. (5-11), (5-14),(5-15) and (5-20) with (5-25), the hardening modulus at the image point can be further developed to:

$$H_b = \frac{(1+e_0)m_p}{(\lambda(s)-\kappa)\,ln\,r}\left[\left(\frac{1}{\bar{p}'\,ln\,r} - \left(\frac{\eta}{M}\right)^n\frac{n}{\bar{p}'}\right)^2 + \left(\left(\frac{\eta}{M}\right)^{n-1}\frac{n}{M\bar{p}'}\right)^2 + \left(\frac{k_1(1+\alpha)\chi}{s_e\left(1+k_1 l(s)\right)ln\,r}\right)^2 + \left(\frac{1}{(1-D)\sigma_0\,ln\,r}\right)^2\right]^{-\frac{1}{2}} \tag{5-26}$$

In the more general case when current stress point lies strictly inside the bounding surface, the plastic modulus H is taken as the sum of H_b and another term, denoted by H_δ. This additive term depends in some way on the distance δ between $\boldsymbol{\sigma}'$and $\bar{\boldsymbol{\sigma}}'$. In this present model, H_δ is postulated to be a function of the scale factor β defined in Eq. (5-13), inspired from the previous work of (Bardet 1986; Morvan et al. 2010). The final form of the plastic modulus H is written as follows:

$$H = H_b + H_\delta; \qquad H_\delta = \frac{1+e_0}{(\lambda(s)-\kappa)}\frac{1-\beta}{\beta}\frac{h}{\left\|\widetilde{\nabla}F\right\|} \tag{5-27}$$

in which h is a material constant. Note that the above expression of the plastic modulus satisfies the following two conditions:

$$H = \begin{cases} H_b & \text{when } \beta = 1 \\ +\infty & \text{when } \beta = 0 \end{cases} \tag{5-28}$$

corresponding respectively to the two limiting cases when the current stress lies on the BS and when it is far from the BS.

5.2.4 Damage mechanism

Similar to the case of plasticity, damage kinetics is controlled by a pseudo-potential of dissipation. It is often described by a scalar-valued damage criterion function which depends on the damage variable D and/or the conjugate damage force Y_D. Although the latter can be

derived directly from the framework of thermodynamics, this usually leads to overly complex expressions. An alternative simpler family of damage evolution laws, which has been successfully applied to concrete and rocks under compressive deviatoric stresses is based on the tensile part of principal strains. Following the approach of Mazars (1986), the tensile part of the principal strain, noted ε_i^+, is defined by:

$$\varepsilon_i^+ = \begin{cases} 0 & \text{if } \varepsilon_i \geq 0 \\ -\varepsilon_i & \text{if } \varepsilon_i < 0 \end{cases} \tag{5-29}$$

Note that the above definition is consistent with the sign convention of positive compressive strains. Moreover, in conventional triaxial compression tests, the axial compressive strain ε_1 is positive while the radial tensile strain ε_3 is negative.

The damage force Y_D is assumed to depend on the tensile parts of principal strains defined above and a simple damage criterion is proposed in the following form(Chiarelli et al.2003; Zhang et al. 2013):

$$f_D(Y_D, D, s) = Y_D - r(D, s) \leq 0 \tag{5-30}$$

$$Y_D = \sqrt{\sum_i (\varepsilon_i^+)^2}\,; \quad r(D, s) = r_0 + r_1(s)D; \quad r_1(s) = k_3\chi(s) \tag{5-31}$$

The function $r(D, s)$ represents the damage threshold which depends on the current values of damage and suction. More specifically, r_0 defines the initial damage threshold and $r_1(s)D$ accounts for the drift due to damage evolution and suction, with the parameters k_3 controlling the suction-dependent sensitivity. The damage evolution rate is determined through the classic "flow" rule:

$$dD = d\lambda_D \frac{\partial f_D}{\partial Y_D} \tag{5-32}$$

in which the damage multiplier $d\lambda_D$ should be determined from the consistency condition of damage criterion, fulfilling the Kuhn–Tucker condition:

$$f_D(Y_D, D, s) = 0; \quad df_D \geq 0; \quad f_D(Y_D, D, s)df_D = 0 \tag{5-33}$$

Specifically, in the case of conventional triaxial tests at constant suction $ds = 0$, the damage evolution rate can be deduced as the following expression:

$$dD = -\sqrt{2}\,\frac{d\varepsilon_3}{r_1(s)} \tag{5-34}$$

5.2.5 Elastoplastic Compliance matrix accounting for damage

For the particular case of constant suction (the only case considered in this chapter) $ds = 0$, the plastic strain rate in Eq. (5-19), on account of Eq. (5-24), can be rewritten in matrix form:

$$d\boldsymbol{\varepsilon}^p - \frac{n_D}{H}\sigma_0 dD\ \boldsymbol{m} = \mathbb{C}^p d\boldsymbol{\sigma}'\ ;\ \mathbb{C}^p = \frac{1}{H}\begin{bmatrix} m_p n_p & m_p n_q \\ m_q n_p & m_q n_q \end{bmatrix} \tag{5-35}$$

where $\mathbb{C}^p$ is the plastic compliance matrix. Summation of Eq. (5-9) and Eq. (5-35) leads us to:

$$d\boldsymbol{\varepsilon} - \frac{n_D}{H}\sigma_0 dD\ \boldsymbol{m} = (\mathbb{C}^e + \mathbb{C}^p)\ d\boldsymbol{\sigma}' \tag{5-36}$$

Taking into account the damage evolution rate dD deduced from Eq. (5-34) and combining with Eqs. (5-6) and (5-7), the following relationship between principle strain and stress increments is obtained after some simple manipulations:

$$d\boldsymbol{E} = \mathbb{C}^{epD} d\boldsymbol{\Sigma} \tag{5-37}$$

with:

$$\mathbb{C}^{epD} = \mathbb{Q}^{-1}(\mathbb{C}^e + \mathbb{C}^p)\,\mathbb{A} \quad ; \quad \mathbb{Q} = \begin{bmatrix} 1 & 2 + \frac{1}{H}\frac{\sqrt{2}\mathrm{n}_D\sigma_0\mathrm{m}_p}{r_1(s)} \\ \frac{2}{3} & -(\frac{2}{3} - \frac{1}{H}\frac{\sqrt{2}\mathrm{n}_D\sigma_0\mathrm{m}_q}{r_1(s)}) \end{bmatrix} \tag{5-38}$$

where $\mathbb{C}^{epD}$ represents the elastoplastic compliance matrix accounting for damage. The above equations define completely the relation between strain and stress increments.

5.3 Model validation against experimental data and discussion

5.3.1 Determination of model parameters

The proposed bounding surface plastic damage model requires 14 parameters for its complete definition. They characterize particular aspects of material behaviour: (1) ν and κ to describe the elastic behaviour. (2) Seven constants on the plastic behaviour: λ_0 and Γ define the position of critical state line (CSL) in the $e - \ln p'$ plane while M defines the slope of CSL in $p' - q$ plane; n and r specify the shape of bounding surface; h controls the hardening modulus; and m controls the stress-dilatancy. (3) Another four model parameters are needed to account for suction effects: s_e and α define the effective stress used in this model, k_1 and k_2 account for suction effects on hardening and volumetric deformability respectively. (4) Finally, the constant k_3 controls damage evolution.

The above model parameters can be determined from a few classic tests in the laboratory. ν is the Poisson's ratio and can be determined through "20% of f_c" cycle. κ can be obtained from isotropic consolidation tests from 100 kPa to 600 kPa confining pressure. $\lambda_0$is based on the slope of failure state line on $e - \ln p'$plane. Γ and M associated with the definition of critical state line can be deduced using triaxial tests at different controlled suctions. The parameter k_2 defining the reduction of volumetric deformability $\lambda(s)$ with suction can be assessed by carrying out triaxial tests at different controlled suctions. s_e is identified as air-entry suction determined from the classical water retention curve and a unique value $\alpha = 0.85$ was adopted for the three different soils as mentioned in the section 5.2. The remaining parameters: h, m, n, r, k_1 and k_3 have to be determined by trial and error using experimental results.

5.3.2 Model implementation

Table 5.1 Model parameters adopted in simulation for Lim and Mix1

Parameter symbols	Role or/andPhysical meanings	Lim	Mix1
ν	Poisson's ratio	0.05	0.05
κ	Slope of unloading line in the e -lnp' space	0.005	0.002
λ_0	Volumetric compressibility constant	0.025	0.024
e_0	Initial void ratio	0.37	0.37
M	Critical state line in q-p' plane	1.65	1.85
n	Constant specify the shape of bouning surface	4	3.5
r	Space ratio	1.4	1.4
h	Constant to calibrate the hardening modulus	1.6	1.6
m	Constant to define plastic potential	1.8	2.2
s_e (MPa)	Air-entry suction	0.77	0.29
α	Constant to define effective stress parameter	0.85	0.85
k_1	Constant to control suction effects on the hardening parameter	0.039	0.015
k_2	Constant to control suction effects on volumetric compressibility	0.005	0.005
k_3	Constant to describes the damage evolution	0.05	0.08

To implement the constitutive model proposed in this paper, a simple computer program was developed under Matlab environment. The performance of this model was investigated by comparing the numerical simulation with a series of triaxial tests results for earthen materials (Lim and Mix1), at different hydraulic conditions (23%, 75%, and 97% relative humidity) and

two confining pressure conditions (100 kPa and 600 kPa). The parameters used for the study are presented in Table 5.1.

5.3.3 Stress-strain behaviour and volumetric evolution

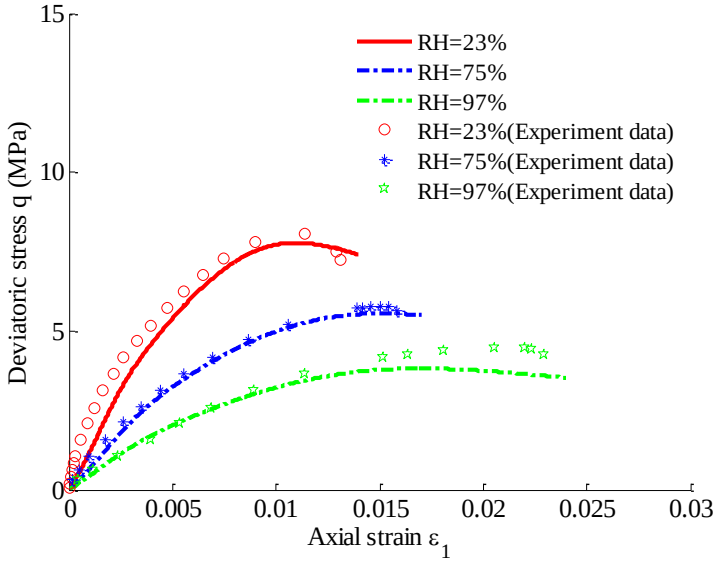

(a)

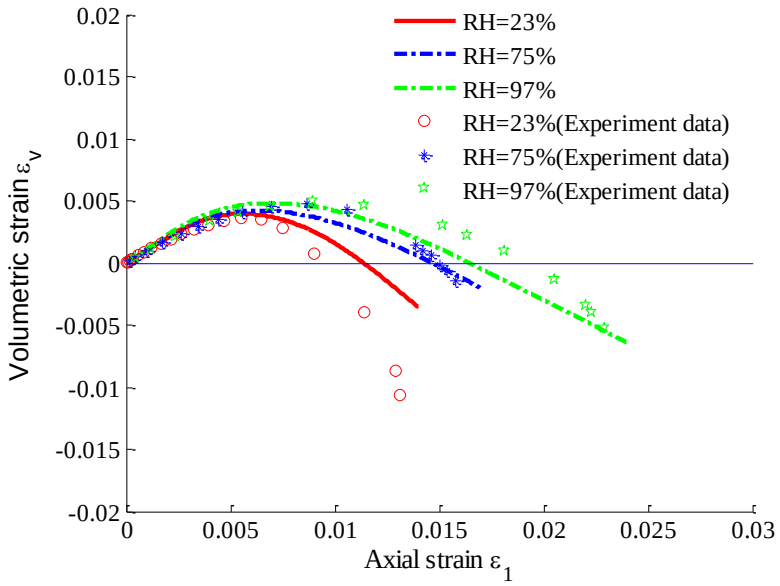

(b)

Figure 5.4 Triaxial compression tests on Lim at three different hydraulic states at 100 kPa confining pressure: (a) q-ε_1 plot and (b) ε_v-ε_1 plot.

Figure 5.4 presents the results of triaxial compression tests and model simulations on Lim at three different hydraulic states (RH=23%, RH=75% and RH=97%), at 100 kPa confining pressure. The comparison shows a good agreement between experiments and simulations in q-ε_1 plane. From Figure 5.3(a), it can be seen the constitutive model is able to describe correctly

the basic features of the unsaturated earthen materials behaviour: plastic and suction induced hardenings. Most notably, the smooth stress-strain behaviour (always observed in experiments) and transitions from pre-peak hardening to post-peak softening were also well simulated.

As shown in Figure 5.4 (b), the volumetric strain versus axial strain ε_v-ε_1 as predicted by this model is also in good agreement with the experimental data. This confirms that the model can indeed reproduce the complex volumetric behaviour: transition from contraction to dilation state. The model also captures the reduced dilation induced by the increasing relative humidity (suction decreasing). At lower hydraulic state RH=23%, some deviations are observed both in stress strain curve and volumetric evolution, especially for the post-peaking stage. One of these explanations is that these excursions could be attributed to some form of localization appearing in the failure of rather brittle materials, which is difficult to simulate through a purely simple modelling approach. Note that this kind of deviation is also faced with in previous modelling work(T. A. Bui et al. 2016; Shao et al. 2006).

Figure 5.5(a and b) shows the results of triaxial compression tests and model simulations of Lim at 600 kPa confining pressure. In q-ε_1 plane, the results predicted by the model are quite in consistent with the experimental data. In ε_v-ε_1 plot, it is seen the dilatancy reproduced by the model is overestimated compared with the test results especially for the RH=23% case. To improve the model's performance, a suction-dependency plastic potential is considered to use in the future work. By making a comparison between Figure 5.4 and Figure 5.5, it is worth noting that the model also captures the increased deviator stress and overall reduced dilation with an increase in confining pressure. As confining pressure increases, it is conjectured particle crushing begins to dominate plastic deformation, resulting in a reducing tendency for a peak in the shear resistance and for a volumetric expansion.

Triaxial compression tests on Mix1 at three different hydraulic states (RH=23%, RH=75% and RH=97%) and at 100 kPa and 600 kPa confining pressure were conducted in the laboratory. A good agreement is obtained between numerical simulation and experimental data as illustrated in Figure 5.6 and Figure 5.7

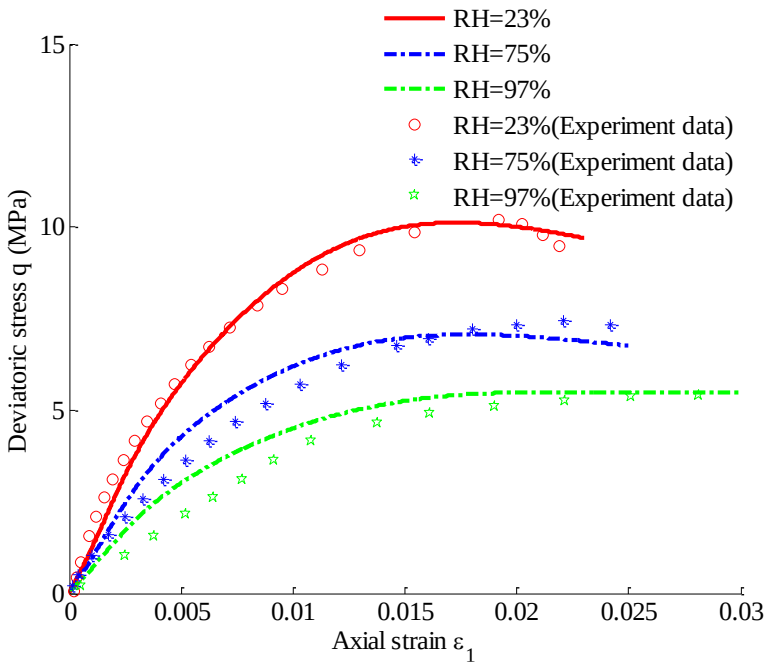

a

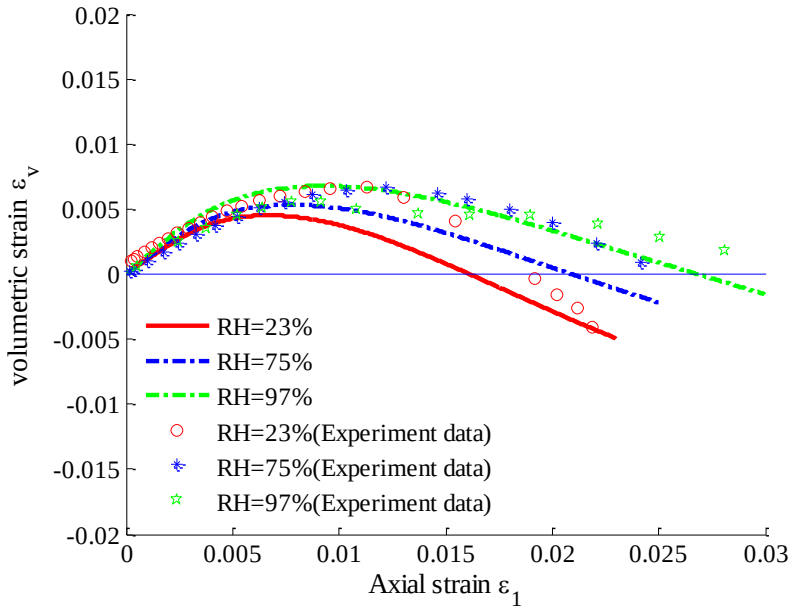

b

Figure 5.5 Triaxial compression tests on Lim at three different hydraulic states at 600 kPa confining pressure: (a) q-ε_1 plot and (b) ε_v-ε_1 plot.

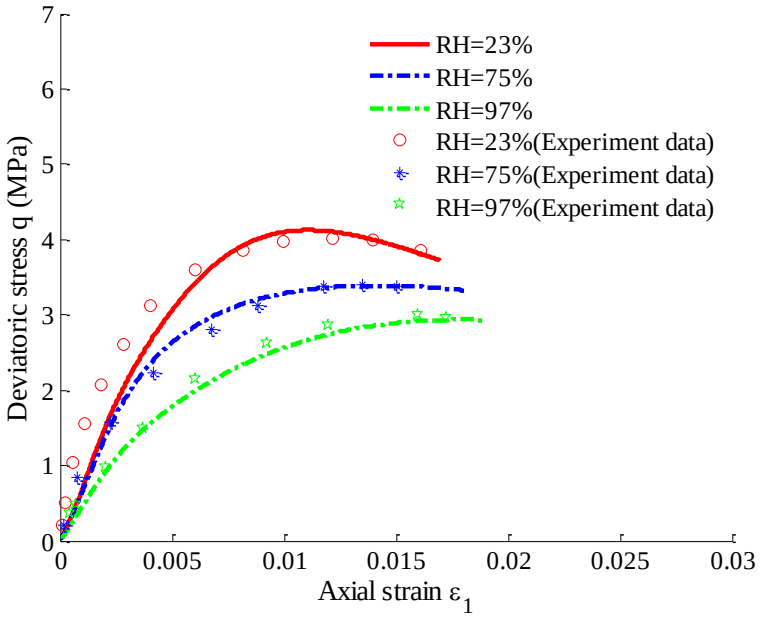

a

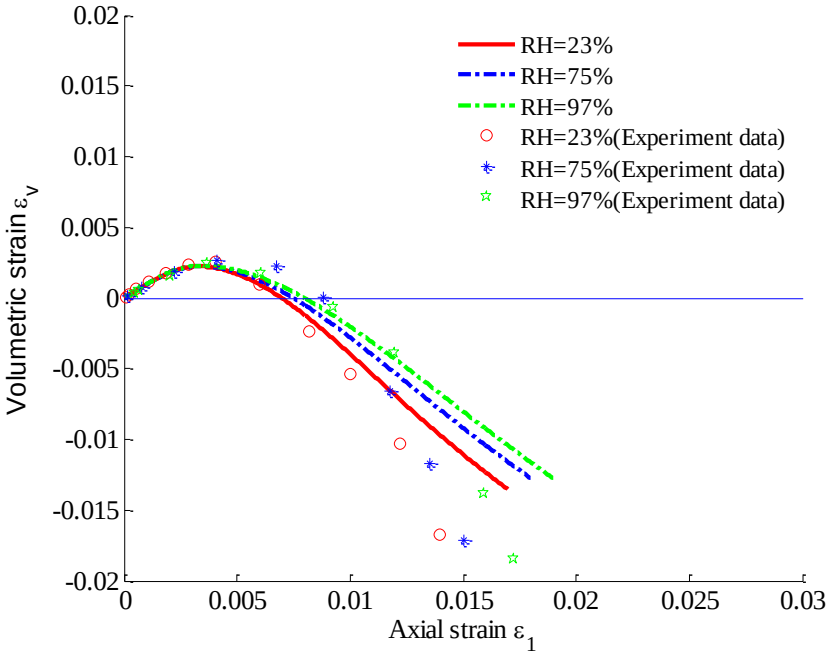

b

Figure 5.6 Triaxial compression tests on Mix1 at three different hydraulic states at 100 kPa confining pressure: (a) q-ε_1 plot and (b) ε_v-ε_1 plot.

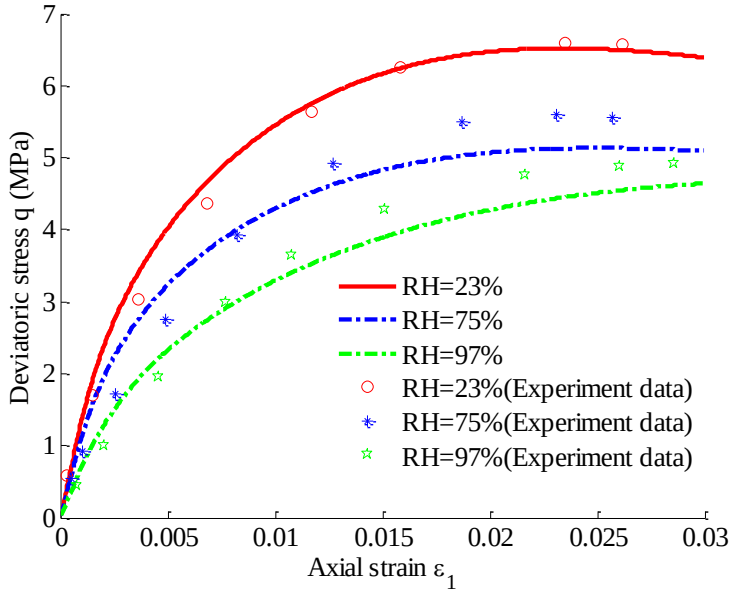

a

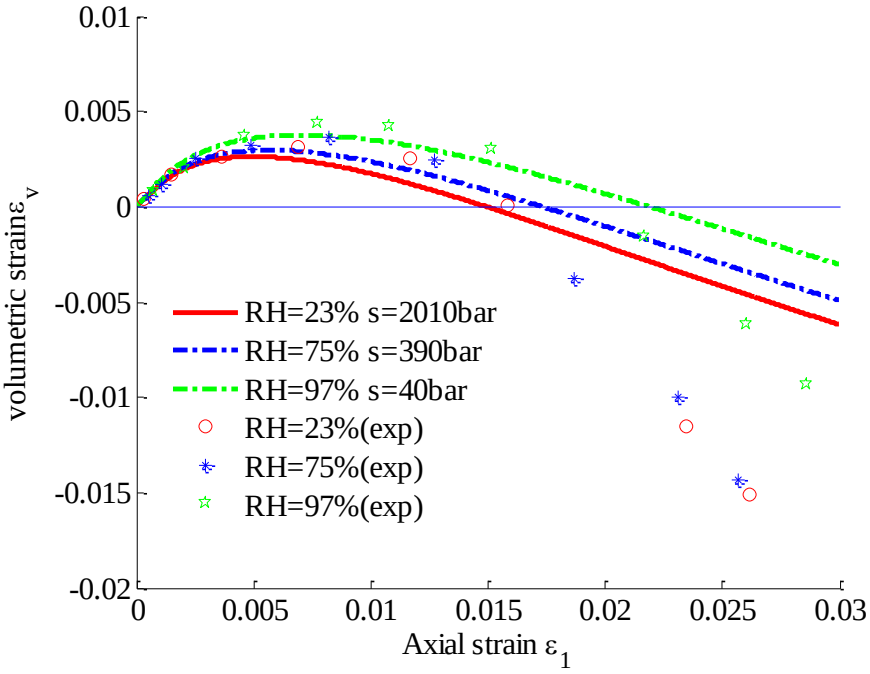

b

Figure 5.7 Triaxial compression tests on Mix1 at three different hydraulic states at 600 kPa confining pressure: (a) q-ε_1 plot and (b) ε_v-ε_1 plot.

5.3.4 Degradation of elastic property

Figure 5.8 presents evolutions of Young's modulus versus radial strain during triaxial tests on Mix1 at confining pressure of 100 kPa and two relative humidity conditions (RH=75% and RH=97%). There is an acceptable agreement between numerical predictions and experimental data, indicating the developed model qualitatively describes the general trend observed in test data: elastic modulus decreases with the damage induced by the radial strain. Considering there is only an additive parameter k_3 to describe the damage evolution rate, the simulation results is acceptable.

In addition, it is worth noticing the degradation rate of Young's modulus at RH=75% (higher suction, lower water content) is higher than that at RH=97% (lower suction, higher water content), which is conform to the physical intuition that higher water content should result in higher ductility.

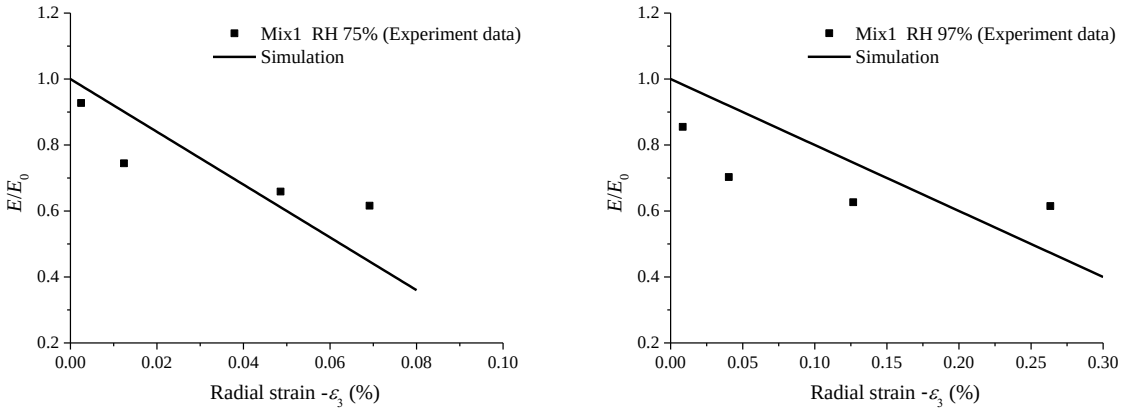

a b

Figure 5.8 Evolutions of Young's modulus versus radial strain during triaxial tests on Mix1 at confining pressure of 100 kPa. (a) RH=75% (b) RH=97%

Finally, in order to illustrate the effects of damage on the stress-strain behaviour, numerical simulations with different values of k_3 are presented for Mix1 at 75% RH and 100 kPa confining pressure (Figure 5.9). With decreasing of k_3, the damage evolution rate becomes higher. From the simulation results, it could be observed that the response of compacted eartnen materials becomes more and more brittle when the effect of damage on plastic flow is stronger.

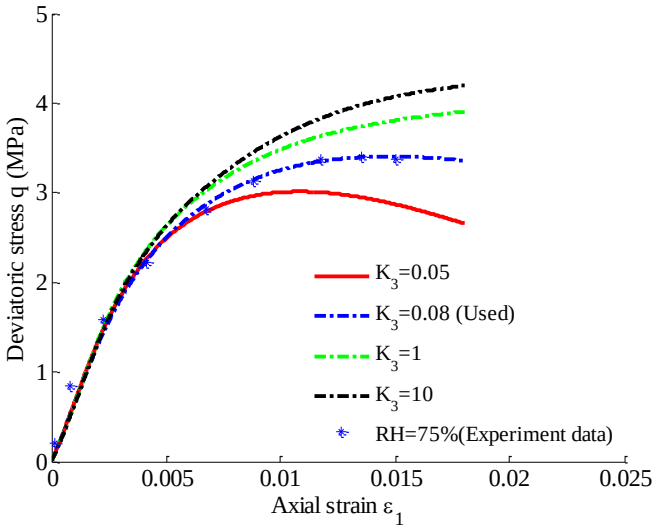

Figure 5.9 Influence of k_3 on the stress-strain behaviour for Mix1 at 75% RH and 100 kPa confining pressure

5.4 Conclusion

A new constitutive model for unsaturated earthen materials is proposed accounting simultaneously for the impact of suction and confining pressure on mechanical properties. This model is formulated using the concept of effective stress and Bounding Surface Plasticity (BSP) theory under a critical state framework. It adopts an whale-head shaped loading and bounding surfaces, a simple radial mapping rule, a non-associative flow rule which generally gives a better description on volumetric behaviour, and suction-dependent hardening controlled by plastic volumetric strains. At the present stage of development, only isotropic damage is considered. Damage evolution rate is assumed to be driven by tensile strain and restrained by suction. Plastic flow and damage evolution occur as coupled processes.

The model has been used to simulate the triaxial compression tests subjected to different relative humidities and confining pressures. Good agreement is generally obtained between model predictions and experimental data. Of fundamental importance in practice, this model only requires 14 independent soil parameters for its definition and makes it ideally suited for engineering applications. Despite the minimal number of parameters, the model is able to reproduce the essential trends in the behaviour of partially saturated earthen materials: suction-induced hardening and stiffening, smooth stress-strain behaviour, post-peak softening as well as contractancy-dilatancy transition. Furthermore, the present model qualitatively describes a degradation of elastic properties observed in experimental data.

Chapter 6
Conclusion and perspective

6.1 General conclusion

A deep understanding of the hydromechanical behaviour of compacted earth is essential in order to pursue studies that permit the protection of the earth heritage and on the other hand for the conception of future modern sustainable constructions. Compacted earth is regarded as a granular mixture in which the clay fraction plays the essential role of binder, but which exhibits a strong interaction with water. During their service period, compacted earths can be subject to large changes in relative humidity. Those perpetual changes of environmental conditions induce continuous changes of water content of the earth that impact significantly its mechanical performances.

The present work is aimed at studying the mechanical behavior of compacted earth with respect to relative humidity and clay content. It begins with an identification of four local earth materials, three kinds of specific laboratory tests (suction test; shrinkage test and sorption-desorption test) were carried out on these raw earth materials, in order to provide a preliminary insight on the effect of clay content and water content; a comprehensive parameter experimental study were further conducted through triaxial tests with loading-unloading cycles, thereby deepening the understanding the impact of clay content and relative humidity (independence and interaction) on the mechanical performance of compacted earth; finally, based on the experimental results, a new constitutive model, specially to simulate the mechanical behaviour, was proposed for compacted earth. Accordingly, the main contributions of this thesis can be summarized from the following three points:

6.1.1 Local raw earth materials

A series of tests on physical properties were firstly carried out in laboratory on four crude earth materials (refered to as STR, CRA, STA and Lim) coming from four different sites. Results indicate all these earths have a dispersion in particle size distribution curves, they contain fine gravel and sand with a fraction of cohesive soils (silt and clay) acting as a binder between the coarse grains. To be precise, clay content in STA and Lim are double than that in STR and CRA. Correspondingly, the plastic index I_p is found to be affected by the clay content.

The detailed specimen fabrication procedure adopted using a homemade double static compaction mould is described and compared with the traditional Proctor test. A series of iso-energy curves are observed for the static compaction. In addition, all the optimum points approximately lie on a constant saturation degree line regardless of the compaction method

(static compaction, Proctor test and CEB fabrication) and compaction energy. This observation should be quite useful in verifying the optimum state used for specimen fabrication.

Suction was measured by a simple filter paper method. Materials with a high clay content tend to possess a higher suction. Besides, matric suction increases with decreasing water content and all suction values approximately lie on the same variation tendency line regardless of various compaction methods and compaction energy during sample fabrication. Meanwhile, sorption-desorption tests were conducted through desiccator method and DVS method respectively. Results from these two methods are quite consistent. Lim has the highest hygroscopic ability to absorb and store moisture from the surrounding air among three types of earth, due to its relatively higher clay content (35%).

6.1.2 Systematic parametric study with respect to clay content and relative humidity

The impact of clay and moisture contents on the shear behavior of compacted earth was investigated taking into account loading-unloading cycles. Fine sand was added into a raw earth named Lim, thereby obtaining three different soils with clay contents respectively of 35%, 26% (named Mix2) and 17% (named Mix1). A series of triaxial tests were conducted on samples previously equilibrated at three different values of relative humidity, 23%, 75% and 97% respectively. The confining pressures are 0, 100, and 600kPa. The evolution of failure strength f_c, Young's modulus E and residual strain ε_{res} with clay content and RH was investigated, the last two parameters being measured during loading-unloading cycles. Results show that the mechanical characteristics of earthen materials have a strong dependence on the ambient relative humidity at which the samples are conditioned, as well as on the clay content:

- Both the maximum deviator stress f_c and Young's modulus E measured from a loading-unloading cycle decrease with the increase of relative humidity. The amplitude of this reduction depends on the clay content.
- An increase of relative humidity leads to more ductile behavior, while a lower relative humidity induces brittleness. This tendency is sharper at high clay content. In parallel, there is an obvious increase of residual strain ε_{res} with the rise of relative humidity at the same stress level.
- The shear strength f_c increases with the rise of clay content (within the range of values investigated) at constant RH and confining pressure. Due to the softening action of water on clays, the amplitude of this strength amplification decreases with increasing relative humidity.

- Young's modulus E is relatively insensitive to changes in clay content considering that the variation of E is less than 20% for all cases.
- Residual strain ε_{res} increases slightly with the rise of clay content at 23% and 75% RH, but an important rise of ε_{res} occurs when RH increases to 97%.
- Increasing the applied stress induces a degradation of secant Young's modulus and an accumulation of residual strain.
- By considering the effective stress parameter χ as a function of suction s, a unified functional form $\chi(s)$ was found for all three soils with a unique value α=0.85such that failure states of all samples lie approximately on a unique failure state line crossing origin plotted in the (p'-q) plane, regardless of the matric suction and confining pressure.

6.1.3 Constitutive modelling

Based on the degradation of secant Young's modulus and the unique failure state, a new constitutive model for compacted earth materials is proposed accounting simultaneously for the impact of suction and confining pressure on mechanical properties. This model is formulated using the concept of effective stress and Bounding Surface Plasticity (BSP) theory under a critical state framework. It adopts whale-head shaped loading and bounding surfaces, a simple radial mapping rule, a non-associative flow rule which generally gives a better description on volumetric behaviour, and suction-dependent hardening controlled by plastic volumetric strains. At the present stage of development, only isotropic damage is considered. Damage evolution rate is assumed to be driven by tensile strain and restrained by suction. Plastic flow and damage evolution occur as coupled processes.

The model has been used to simulate the triaxial compression tests subjected to different relative humidities and confining pressures. Good agreement is generally obtained between model predictions and experimental data. Of fundamental importance in practice, this model only requires 14 independent soil parameters for its definition and makes it ideally suited for engineering applications. Despite the minimal number of parameters, the model is able to reproduce the essential trends in the behaviour of partially saturated earthen materials: suction-induced hardening and stiffening, smooth stress-strain behaviour, post-peak softening as well as contractancy-dilatancy transition. Furthermore, the present model qualitatively describes a degradation of elastic properties observed in experimental data.

6.2 Perspectives

Some potential developments of the present work are summarised as follows:

- MIP (Mercury Intrusion Porosimetry) tests or SEM (scanning electronic microscopy) are suggested to be done in future work, in order to obtain information on the microstructural mechanisms in view of achieving a better understanding of how the clay fraction influences the overall mechanical properties.
- A larger experimental range of the relative humidity and clay content should be investigated thereby checking whether there is a threshold in terms of their influence on the mechanical behaviour.
- Activity of clay fraction should also be another indispensable factor, considering its impact on the microstructures and mechanical behaviour.
- In order to make a full life cycle assessment for earth structures, the more complex stress path should be carried out in triaxial or oedometric tests. It is thought to largely reveal the normal working condition of earth construction, and to provide meaningful prediction for the mechanical behaviour.
- As for the constitutive modelling, a suction-dependency plastic potential and a more complicated damage evolution law is considered to use, in order to improve the model precision. Besides, the model in its current form is intended for monotonic loading, an extension of this model to cyclic loading will be the subject of future work.

Appendix

Stress-strain curves and volumetric evolution at 0kPa and 600kPa confining pressure

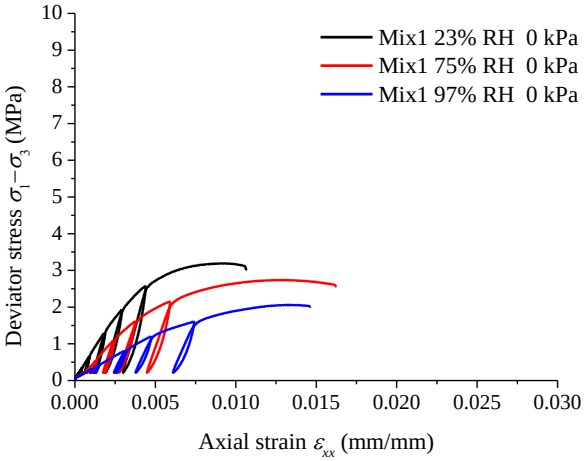

(a) Mix1

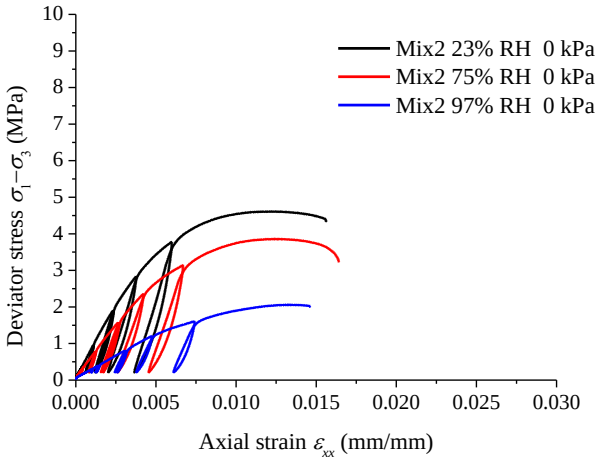

(b) Mix2

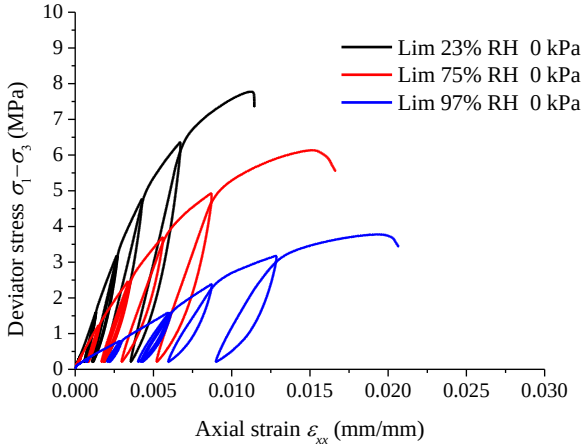

(c) Lim

Figure A.1 Stress–strain behavior at given relative humidity and 0 kPa confining pressure for Mix1, Mix2 and Lim

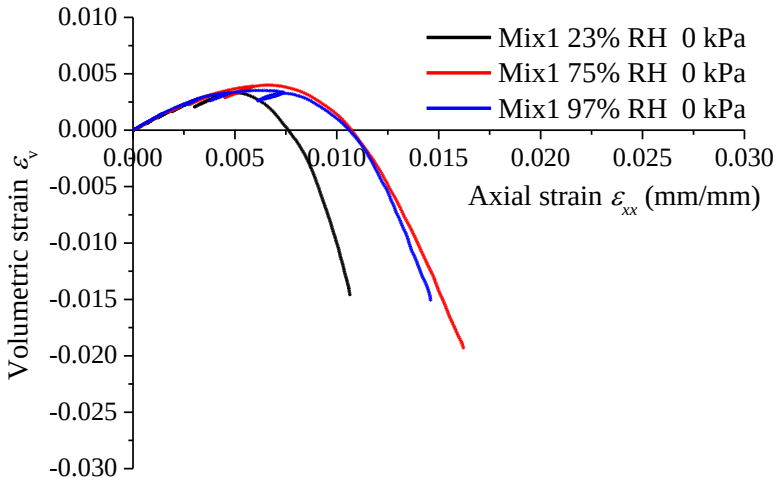

(a) Mix1

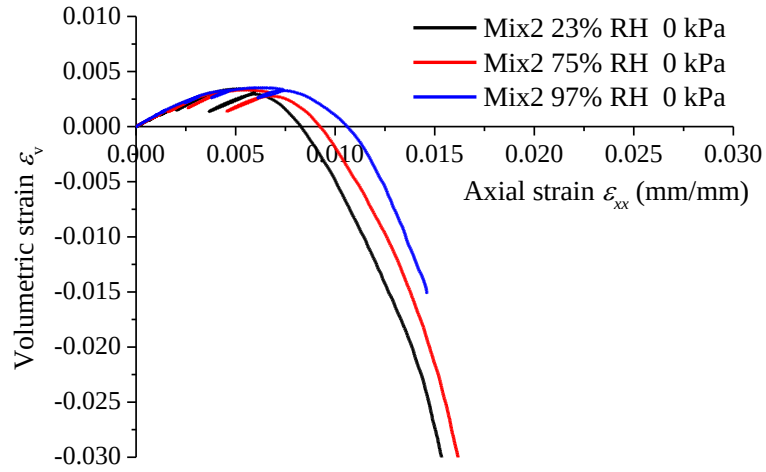

(b) Mix2

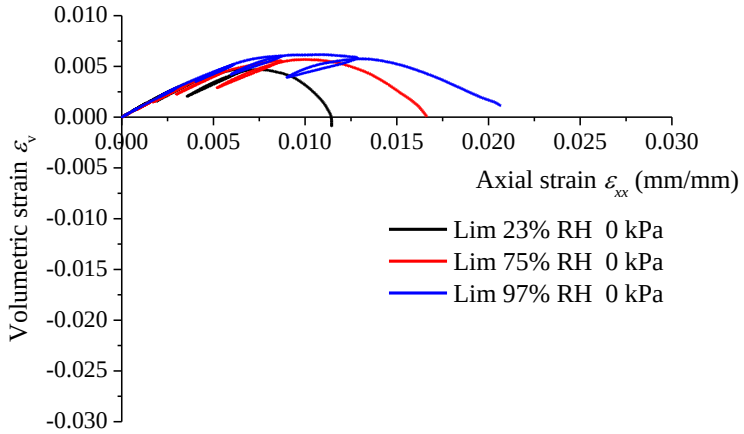

(c) Lim

Figure A.2 Volumetric evolution versus axial strain at given relative humidity and 0 kPa confining pressure for Mix1, Mix2 and Lim

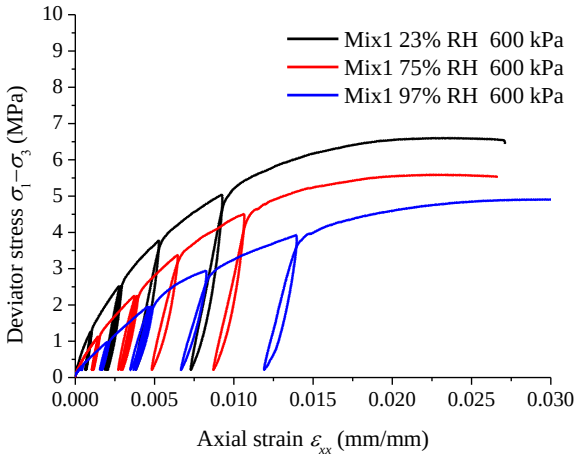

(a) Mix1

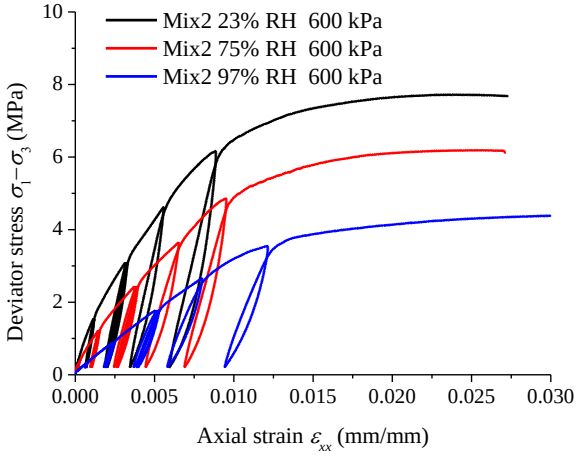

(b) Mix2

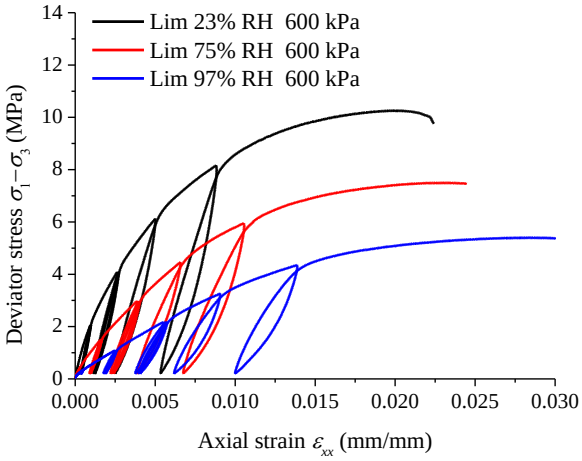

(c) Lim

Figure A.3 Stress–strain behavior at given relative humidity and 600 kPa confining pressure for Mix1, Mix2 and Lim

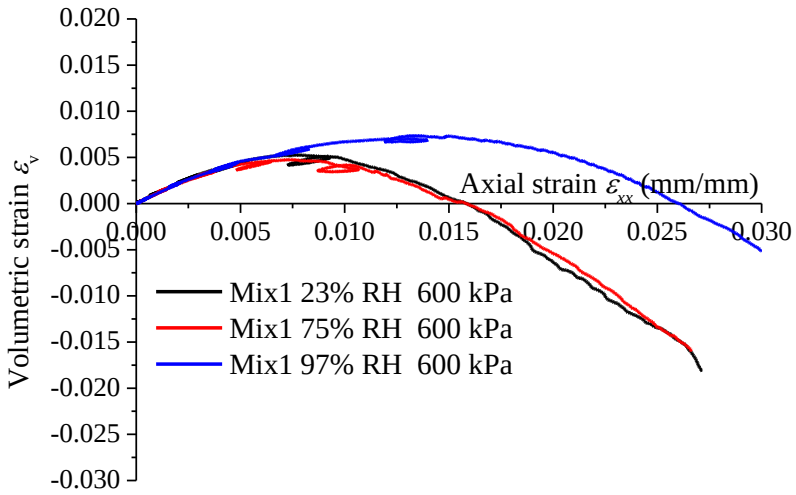

(a) Mix1

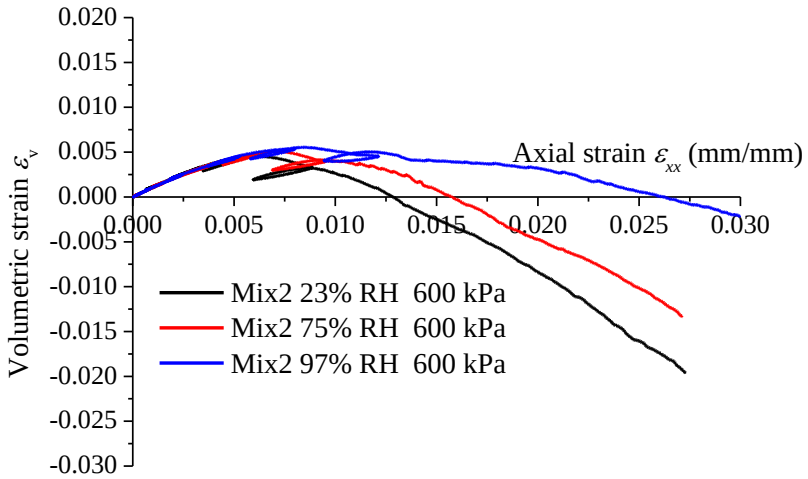

(b) Mix2

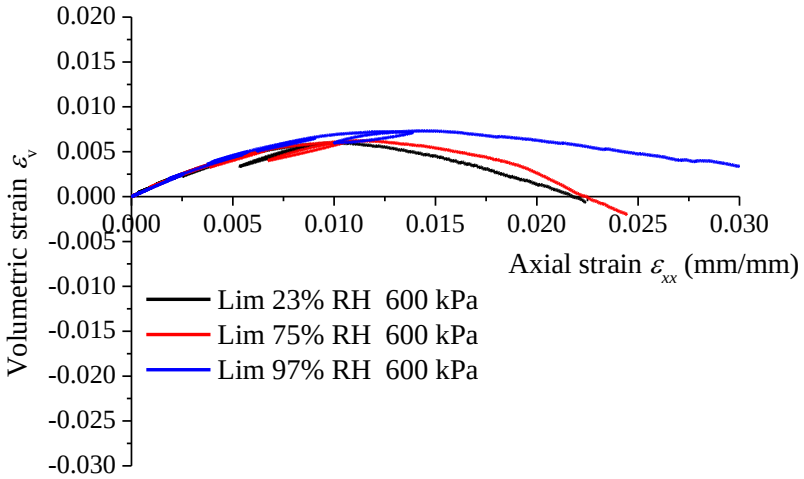

(c) Lim

Figure A.4 Volumetric evolution versus axial strain at given relative humidity and 600 kPa confining pressure for Mix1, Mix2 and Lim

References

ADEME. 2015. “Déchets Edition 2015.” *Techanical report*.

AFNOR. 2001. “Compressed Earth Blocks for Walls and Partitions : Definitions - Specifications - Test Methods - Delivery Acceptance Conditions.”

Aitchison, G D. 1985. “Relationships of Moisture Stress and Effective Stress Functions in Unsaturated Soils.” *Golden Jubilee of the International Society for Soil Mechanics and Foundation Engineering: Commemorative Volume*: 20.

Ashour, Taha, and Wei Wu. 2010. “An Experimental Study on Shrinkage of Earth Plaster with Natural Fibres for Straw Bale Buildings.” *International Journal of Sustainable Engineering* 3(4): 299–304.

ASTM D5298-03. 2003. “Standard Test Method for Measurement of Soil Potential (Suction) Using Filter Paper.”

Attom, Mousa F. 1997. “The Effect of Compactive Energy Level on Some Soil Properties.” *Applied Clay Science* 12(1-2): 61–72. http://linkinghub.elsevier.com/retrieve/pii/S0169131796000373.

Bardet, J P. 1986. “Bounding Surface Plasticity Model for Sands.” *Journal of engineering mechanics* 112(11): 1198–1217.

Bishop, Alan W. 1959. “The Principle of Effective Stress.” *Teknisk ukeblad* 39: 859–63.

Bruno, Agostino Walter. 2016. “Hygro-Mechanical Characterisation of Hypercompacted Earth for Building Construction.” PhD thesis Université de Pau et des Pays de l’Adour.

Bruno, Agostino Walter, Domenico Gallipoli, Céline Perlot, and Joao Mendes. 2017. “Mechanical Behaviour of Hypercompacted Earth for Building Construction.” *Materials and Structures/Materiaux et Constructions* 50(2).

Bui, Q. B., S. Hans, J. C. Morel, and A. P. Do. 2011. “First Exploratory Study on Dynamic Characteristics of Rammed Earth Buildings.” *Engineering Structures* 33(12): 3690–95.

Bui, Quoc Bao, and Jean Claude Morel. 2009. “Assessing the Anisotropy of Rammed Earth.” *Construction and Building Materials* 23(9): 3005–11.

Bui, Quoc Bao, Jean Claude Morel, Stéphane Hans, and Nicolas Meunier. 2009.

"Compression Behaviour of Non-Industrial Materials in Civil Engineering by Three Scale Experiments: The Case of Rammed Earth." *Materials and Structures* 42(8): 1101–16.

Bui, Quoc-Bao. 2008. "Stabilité Des Structures En Pisé : Durabilité, Caractéristiques Mécaniques." PhD thesis Institut National des Sciences appliquées, Lyon.

Bui, Quoc-Bao, Jean Claude Morel, Stéphane Hans, and Peter Walker. 2014a. "Effect of Moisture Content on the Mechanical Characteristics of Rammed Earth." *Construction and Building Materials* 54: 163–69.

Bui, Quoc-Bao, Jean-Claude Morel, Stéphane Hans, and Nicolas Meunier. 2008. "Compression Behaviour of Non-Industrial Materials in Civil Engineering by Three Scale Experiments: The Case of Rammed Earth." *Materials and Structures* 42(8): 1101–16. http://www.springerlink.com/index/10.1617/s11527-008-9446-y.

Bui, Quoc-Bao, Jean-Claude Morel, Stéphane Hans, and Peter Walker. 2014b. "Effect of Moisture Content on the Mechanical Characteristics of Rammed Earth." *Construction and Building materials* 54: 163–69.

Bui, T. T., Q. B. Bui, A. Limam, and S. Maximilien. 2014. "Failure of Rammed Earth Walls: From Observations to Quantifications." *Construction and Building Materials* 51: 295–302.

Bui, Tuan Anh et al. 2016. "A Coupled Poroplastic Damage Model Accounting for Cracking Effects on Both Hydraulic and Mechanical Properties of Unsaturated Media." *International Journal for Numerical and Analytical Methods in Geomechanics* 40(5): 625–50.

Chabriac, Pierre-antoine. 2014. "Mesure Du Comportement Hygrothermique Du Pisé." ENTPE.

Champire, Florian. 2017. "Étude Expérimentale Du Comportement Hydro-Mécanique de La Terre Crue Compactée Pour La Construction." PhD thesis ENTPE.

Champiré, Florian et al. 2016. "Impact of Relative Humidity on the Mechanical Behavior of Compacted Earth as a Building Material." *Construction and Building Materials* 110: 70–78.

Chiappone, Antonella, Stefania Marello, Claudio Scavia, and Massimo Setti. 2004. "Clay

Mineral Characterization through the Methylene Blue Test: Comparison with Other Experimental Techniques and Applications of the Method." *Canadian Geotechnical Journal* 41(6): 1168–78. http://www.nrcresearchpress.com/doi/abs/10.1139/t04-060.

Chiarelli, Anne-Sophie, Jian-Fu Shao, and N Hoteit. 2003. "Modeling of Elastoplastic Damage Behavior of a Claystone." *International Journal of plasticity* 19(1): 23–45.

Ciancio, Daniela, and Joshua Gibbings. 2012. "Experimental Investigation on the Compressive Strength of Cored and Molded Cement-Stabilized Rammed Earth Samples." *Construction and Building Materials* 28(1): 294–304.

Collectif FFB. 2012. "Règles Professionnelles Pour La Mise En Oeuvre Des Enduits Sur Supports Composés de Terre Crue." Recherche et développement métier.

Collet, Florence, L. Serres, J. Miriel, and M. Bart. 2006. "Study of Thermal Behaviour of Clay Wall Facing South." *Building and Environment* 41(3): 307–15.

Dafalias, Yannis F. 1986. "Bounding Surface Plasticity. I: Mathematical Foundation and Hypoplasticity." *Journal of Engineering Mechanics* 112(9): 966–87.

Dafalias, Yannis F, and Leonard R Herrmann. 1986. "Bounding Surface Plasticity. II: Application to Isotropic Cohesive Soils." *Journal of Engineering Mechanics* 112(12): 1263–91.

Dao, Vinh T N, Peter H Morris, and Peter F Dux. 2011. "Plastic Shrinkage Cracking of Concrete-Roles of Osmotic Suction." *Magazine of Concrete Research* 63(10): 743–50.

Delage, Pierre, and Yu-Jun Cui. 2008. "An Evaluation of the Osmotic Method of Controlling Suction." *Geomechanics and Geoengineering: An International Journal* 3(1): 1–11.

Delinière, R, J E Aubert, F Rojat, and M Gasc-Barbier. 2014. "Physical, Mineralogical and Mechanical Characterization of Ready-Mixed Clay Plaster." *Building and Environment* 80: 11–17.

Dragon, A, and Z Mroz. 1979. "A Continuum Model for Plastic-Brittle Behaviour of Rock and Concrete." *International Journal of Engineering Science* 17(2): 121–37.

Emiroğlu, Mehmet, Ahmet Yalama, and Yasemin Erdoğdu. 2015. "Performance of Ready-Mixed Clay Plasters Produced with Different Clay/sand Ratios." *Applied Clay Science* 115: 221–29.

Fabbri, Antonin, Fionn McGregor, Ines Costa, and Paulina Faria. 2017. “Effect of Temperature on the Sorption Curves of Earthen Materials.” *Materials and Structures* 50(6): 253.

Fodde, Enrico. 2009. “Traditional Earthen Building Techniques in Central Asia.” *International Journal of Architectural Heritage* 3(2): 145–68.

Forster, Alan M., Gabriela M. Medero, Tom Morton, and Jim Buckman. 2008. “Traditional Cob Wall: Response to Flooding.” *Structural Survey* 26(4): 302–21. http://www.emeraldinsight.com/doi/10.1108/02630800810906557.

Fredlund, D G, N Ro Morgenstern, and R A Widger. 1978. “The Shear Strength of Unsaturated Soils.” *Canadian geotechnical journal* 15(3): 313–21.

Fredlund, D G, and H Rahardjo. 1993. “Soil Mechanics for Unsaturated Soils.” *Stress The International Journal on the Biology of Stress*: 517. http://books.google.com/books?hl=en&lr=&id=ltVtPOGuJJwC&oi=fnd&pg=PA1&dq=Soil+Mechanics+for+Unsaturated+Soils&ots=XIsVieTOHf&sig=7le-tXP6NbjK3xG0WUbc8JpXhJY.

French Standard NF P 94-051. 1993. “Soil: Investigation and Testing – Determination of Atterberg’s Limits– Liquid Limit Test Using Cassagrande Apparatus and Plastic Limit Test on Rolled Thread.” *AFNOR*.

French Standard NF P 94-056. 1996. “Soil: Investigation and Testing – Grain Size Analysis – Dry Sieving Method after Washing.” *AFNOR*.

French Standard NF P 94-057. 1992. “Soil: Investigation and Testing – Grain Size Analysis – Hydrometer Method.” *AFNOR*.

French Standard NF P 94-068. 1998. “Soil: Investigation and Testing – Measuring of the Methylene Blue Adsorption Capacity of a Rocky Soil – Determination of the Methylene Blue of a Soil by Means of Stain Test.” *AFNOR*.

French Standard NF P 94-093. 1999. “Soil: Investigation and Testing – Determination of the Compaction Reference Values of a Soil Type – Standard Proctor Test and Modified Proctor Test.” *AFNOR*.

Gajo, A., and D. Muir Wood. 2001. “A New Approach to Anisotropic, Bounding Surface Plasticity: General Formulation and Simulations of Natural and Reconstituted Clay

Behaviour.” *International Journal for Numerical and Analytical Methods in Geomechanics* 25(3): 207–41.

Geiser, F, L Laloui, and L Vulliet. 2006. “Elasto-Plasticity of Unsaturated Soils : Laboratory Test Results on a Remoulded Silt.” *Soils and Foundations* 46(5): 545–56.

Gens, Antonio, and Sebastià Olivella. 2001. “THM Phenomena in Saturated and Unsaturated Porous Media: Fundamentals and Formulation.” *Revue française de génie civil* 5(6): 693–717.

Gerard, Pierre, Mohamed Mahdad, Alexandre Robert McCormack, and Bertrand François. 2015. “A Unified Failure Criterion for Unstabilized Rammed Earth Materials upon Varying Relative Humidity Conditions.” *Construction and Building Materials* 95: 437–47.

Hall, Matthew, and Youcef Djerbib. 2004. “Rammed Earth Sample Production: Context, Recommendations and Consistency.” *Construction and Building Materials* 18(4): 281–86.

Hall, Matthew R., Rick Lindsay, and Meror Krayenhoff. 2012. “Overview of Modern Earth Building.” In *Modern Earth Buildings: Materials, Engineering, Constructions and Applications*, , 3–16.

Hamard, Erwan et al. 2013. “A Procedure to Assess the Suitability of Plaster to Protect Vernacular Earthen Architecture.” *Journal of Cultural Heritage* 14(2): 109–15.

Hamard, Erwan. 2017. “Rediscovering of Vernacular Adaptive Construction Strategies for Sustainable Modern Building - Application to Cob and Rammed Earth.” ENTPE.

Hayakawa, K, and S Murakami. 1997. “Thermodynamical Modeling of Elastic-Plastic Damage and Experimental Validation of Damage Potential.” *International Journal of damage mechanics* 6(4): 333–63.

Helson, Olivier et al. 2017. “Physical and Mechanical Properties of Soilcrete Mixtures: Soil Clay Content and Formulation Parameters.” *Construction and Building Materials* 131: 775–83.

Hendrickson, Chris, and Arpad Horvath. 2000. “Resource Use and Environmental Emissions of U.S. Construction Sectors.” *Journal of Construction Engineering and Management* 126(1): 38–44. http://ascelibrary.org/doi/10.1061/%28ASCE%290733-

9364%282000%29126%3A1%2838%29.

Hu, Pan, Qing Yang, and Pei-yong Li. 2010. “Direct and Indirect Measurement of Soil Suction in the Laboratory.” *Electronic Journal of Geotechnical Engineering (EJGE)* 15: 1–13. http://ejge.com/2010/Ppr10.009/Ppr10.009.pdf.

ISO 12571. 2000. “Hygrothermal Performance of Building Materials and Products – Determination of Hygroscopic Sorption Properties.”

Jaquin, P A, C E Augarde, D Gallipoli, and D G Toll. 2009. “The Strength of Unstabilised Rammed Earth Materials.” *Géotechnique.* 59(5): 487–90.

Jennings, J E B, and J B Burland. 1962. “Limitations to the Use of Effective Stresses in Partly Saturated Soils.” *Géotechnique* 12(2): 125–44.

Jiménez Delgado, M. Carmen, and Ignacio Cañas Guerrero. 2007. “The Selection of Soils for Unstabilised Earth Building: A Normative Review.” *Construction and Building Materials* 21(2): 237–51.

Ju, J W. 1989. “On Energy-Based Coupled Elastoplastic Damage Theories: Constitutive Modeling and Computational Aspects.” *International Journal of Solids and structures* 25(7): 803–33.

Kan, Mojtaba E, and Hossein A Taiebat. 2014. “A Bounding Surface Plasticity Model for Highly Crushable Granular Materials.” *Soils and Foundations* 54(6): 1188–1201.

Kenai, S., R. Bahar, and M. Benazzoug. 2006. “Experimental Analysis of the Effect of Some Compaction Methods on Mechanical Properties and Durability of Cement Stabilized Soil.” In *Journal of Materials Science*, , 6956–64.

Khalili, N, and M H Khabbaz. 1998. “A Unique Relationship of Chi for the Determination of the Shear Strength of Unsaturated Soils.” *Geotechnique* 48(5).

Kim, Ukgie, Dongwook Kim, and Li Zhuang. 2016. “Influence of Fines Content on the Undrained Cyclic Shear Strength of Sand–clay Mixtures.” *Soil Dynamics and Earthquake Engineering* 83: 124–34.

Koliji, Azad. 2008. “Mechanical Behaviour of Unsaturated Aggregated Soils.”

Kouakou, C H, and Jean-Claude Morel. 2009. “Strength and Elasto-Plastic Properties of Non-Industrial Building Materials Manufactured with Clay as a Natural Binder.” *Applied*

Clay Science 44(1-2): 27–34.

Kouakou, C. H., and J. C. Morel. 2009. “Strength and Elasto-Plastic Properties of Non-Industrial Building Materials Manufactured with Clay as a Natural Binder.” *Applied Clay Science* 44(1-2): 27–34.

Labat, Matthieu, Camille Magniont, Nicolaas Oudhof, and Jean Emmanuel Aubert. 2016. “From the Experimental Characterization of the Hygrothermal Properties of Straw-Clay Mixtures to the Numerical Assessment of Their Buffering Potential.” *Building and Environment* 97: 69–81.

Lai, Ba Tien, Henry Wong, Antonin Fabbri, and Denis Branque. 2016. “A New Constitutive Model of Unsaturated Soils Using Bounding Surface Plasticity (BSP) and a Non-Associative Flow Rule.” *Innovative Infrastructure Solutions* 1(1): 3.

Laloui, Lyesse. 2013. Mechanics of Unsaturated Geomaterials *Mechanics of Unsaturated Geomaterials*.

Lautrin, Danielle. 1989. “Essai au bleu de methylene-utilisation pratique des parametres derives de l’essai au bleu de methylene dans les projets de génie civil.” *Bulletin de liaison des Laboratoires des Ponts et Chaussées* (160).

Lei, Xiaoqin. 2015. “Theoretical Modelling of Coupled Chemo-Hydro-Mechanical Behaviour of Unsaturated Expansive Clays.” INSA Lyon.

Lemaitre, Jean. 2012. *A Course on Damage Mechanics*. Springer Science & Business Media.

Lilley, D.M., and J Robinson. 1995. “Ultimate Strength of Rammed Earth Walls with Openings.” *Proceedings of the ICE - Structures and Buildings London*: 278–87.

Liu, J. et al. 2005. “The Regeneration Research and Practice of the Yaodong (cave) Dwellings in the Loess Plateau of China.” In *22nd International Conference, PLEA 2005: Passive and Low Energy Architecture - Environmental Sustainability: The Challenge of Awareness in Developing Societies, Proceedings*,.

Lu, Ning, and William J Likos. 2004. *Unsaturated Soil Mechanics*. Wiley.

Maniatidis, Vasilios, and Peter Walker. 2003. “A Review of Rammed Earth Construction.” *Developing rammed earth for UK housing* (May): 109. http://staff.bath.ac.uk/abspw/rammedearth/review.pdf.

Mazars, Jacky. 1986. “A Description of Micro-and Macroscale Damage of Concrete Structures.” *Engineering Fracture Mechanics* 25(5-6): 729–37.

Mesbah, A, J C Morel, and M Olivier. 1999. “Clayey Soil Behaviour under Static Compaction Test.” *Materials and structures* 32(223): 687–94.

Miccoli, Lorenzo et al. 2014. “Static Behaviour of Rammed Earth: Experimental Testing and Finite Element Modelling.” *Materials and Structures* 48(10): 3443–56.

Miccoli, Lorenzo, Anastasios Drougkas, and Urs Müller. 2016. “In-Plane Behaviour of Rammed Earth under Cyclic Loading: Experimental Testing and Finite Element Modelling.” *Engineering Structures* 125: 144–52.

Miccoli, Lorenzo, Angelo Garofano, Patrick Fontana, and Urs Müller. 2015. “Experimental Testing and Finite Element Modelling of Earth Block Masonry.” *Engineering Structures* 104: 80–94.

Minke, Gernot. 2009. “Building with Earth.” *Mother Earth News*: 123.

Morel, J. C., A. Mesbah, M. Oggero, and P. Walker. 2001. “Building Houses with Local Materials: Means to Drastically Reduce the Environmental Impact of Construction.” *Building and Environment* 36(10): 1119–26.

Morel, J. C., Abalo Pkla, and Peter Walker. 2007. “Compressive Strength Testing of Compressed Earth Blocks.” *Construction and Building Materials* 21(2): 303–9.

Morel, Jean-Claude, Abalo Pkla, Peter Walker, and Peter Walker. 2007. “Compressive Strength Testing of Compressed Earth Blocks.” *Construction and Building Materials* 21(2): 303–9.

Morvan, M, H Wong, and D Branque. 2010. “An Unsaturated Soil Model with Minimal Number of Parameters Based on Bounding Surface Plasticity.” *International Journal for Numerical and Analytical Methods in Geomechanics* 34(14): 1512–37.

Mroz, Zi. 1967. “On the Description of Anisotropic Workhardening.” *Journal of the Mechanics and Physics of Solids* 15(3): 163–75.

Nabouch, Ranime EL. 2016. “Mechanical Behavior of Rammed Earth Walls under Pushover Tests.” PhD thesis Université Grenoble Alpes.

Narayanaswamy, Abhilash Holur. 2017. “Mechanical Testing Procedure for Local Building

Materials: Rammed Earth and Laterite Building Stones." PhD thesis ENTPE.

Nikooee, Ehsan, Ghassem Habibagahi, S. Majid Hassanizadeh, and Arsalan Ghahramani. 2012. "Effective Stress in Unsaturated Soils: A Thermodynamic Approach Based on the Interfacial Energy and Hydromechanical Coupling." *Transport in Porous Media* 96(2): 369–96.

Niroumand, Hamed, M.F.M. Zain, and Maslina Jamil. 2013. "Various Types of Earth Buildings." *Procedia - Social and Behavioral Sciences* 89: 226–30. http://linkinghub.elsevier.com/retrieve/pii/S1877042813029704.

Nuth, Mathieu, and Lyesse Laloui. 2008. "Effective Stress Concept in Unsaturated Soils: Clarification and Validation of a Unified Framework." *International Journal for Numerical and Analytical Methods in Geomechanics* 32(7): 771–801.

Olivier, Myriam. 1994. "Le Matériau Terre : Compactage, Comportement, Application Aux Structures En Blocs de Terre." INSA Lyon.

Olivier, Myriam, and Ali Mesbah. 1986. "Le Matériau Terre: Essai de Compactage Statique Pour La Fabrication de Briques de Terre Compressées." *Bull Liaison Labo P et*: 146.

Patil, Ujwalkumar D, Anand J Puppala, Laureano R Hoyos, and Aravind Pedarla. 2017. "Modeling Critical-State Shear Strength Behavior of Compacted Silty Sand via Suction-Controlled Triaxial Testing." *Engineering Geology* 231: 21–33.

Peng, X., and R. Horn. 2005. "Modeling Soil Shrinkage Curve across a Wide Range of Soil Types." *Soil Science Society of America Journal* 69(3): 584. https://www.soils.org/publications/sssaj/abstracts/69/3/0584.

Pereira, Jean-Michel, Henry Wong, Philippe Dubujet, and Patrick Dangla. 2005. "Adaptation of Existing Behaviour Models to Unsaturated States: Application to CJS Model." *International Journal for Numerical and Analytical Methods in Geomechanics* 29(11): 1127–55.

Piattoni, Quintilio, Enrico Quagliarini, and Stefano Lenci. 2011. "Experimental Analysis and Modelling of the Mechanical Behaviour of Earthen Bricks." *Construction and Building Materials* 25(4): 2067–75.

Pignal, Bruno. 2005. "Terre Crue - Techniques de Construction et de Restauration." *Eyrolles*.

Pusch, Roland, and Raymond N Yong. 2014. *Microstructure of Smectite Clays and Engineering Performance*. CRC Press.

Reeves George M, Sims Ian, Cripps J. C. 2006. Geological Society engineering geology special publication. Special Edition *Clay Materials Used in Construction*. http://books.google.co.uk/books?id=iDqaIaLe6lkC&dq=mercia+mudstone+properties&source=gbs_navlinks_s.

Rowe, R. Kerry (Ed.). 2012. *Geotechnical and Geoenvironmental Engineering Handbook*. Springer Science & Business Media.

Russell, A R, and N Khalili. 2006. "A Unified Bounding Surface Plasticity Model for Unsaturated Soils." *International Journal for Numerical and Analytical Methods in Geomechanics* 30(3): 181–212.

Russell, Adrian R, and Nasser Khalili. 2004. "A Bounding Surface Plasticity Model for Sands Exhibiting Particle Crushing." *Canadian Geotechnical Journal* 41(6): 1179–92.

Sameh, Sherin H. 2014. "Promoting Earth Architecture as a Sustainable Construction Technique in Egypt." *Journal of Cleaner Production* 65: 362–73.

Schroeder, Horst. 2012. "Modern Earth Building Codes, Standards and Normative Development." In *Modern Earth Buildings: Materials, Engineering, Constructions and Applications*, , 72–109.

Shao, Jian-Fu, Yun Jia, Djimedo Kondo, and Anne-Sophie Chiarelli. 2006. "A Coupled Elastoplastic Damage Model for Semi-Brittle Materials and Extension to Unsaturated Conditions." *Mechanics of materials* 38(3): 218–32.

Sharma, Vandna, Bhanu M. Marwaha, and Hemant K. Vinayak. 2016. "Enhancing Durability of Adobe by Natural Reinforcement for Propagating Sustainable Mud Housing." *International Journal of Sustainable Built Environment* 5(1): 141–55.

Sheng, Daichao. 2011. "Review of Fundamental Principles in Modelling Unsaturated Soil Behaviour." *Computers and Geotechnics* 38(6): 757–76.

Soudani, Lucie Caroline Laurence. 2017. "Modelling and Experimental Validation of the Hygrothermal Performances of Earth as a Building Material." ENTPE.

Soudani, Lucile et al. 2016. "Assessment of the Validity of Some Common Assumptions in

Hygrothermal Modeling of Earth Based Materials." *Energy and Buildings* 116: 498–511.

Soudani, Lucile et al. 2017. "Energy Evaluation of Rammed Earth Walls Using Long Term in-Situ Measurements." *Solar Energy* 141: 70–80. http://linkinghub.elsevier.com/retrieve/pii/S0038092X16305187.

Taylor, Brendon, Stephen Vardy, and Colin MacDougall. 2006. "Compressive Strength Testing of Earthen Plasters for Straw Bale Wall Application." In *Advances in Engineering Structures, Mechanics & Construction*, Springer, 175–83.

Tennakoon, Nayoma, Buddhima Indraratna, Sanjay Nimbalkar, and Scott W Sloan. 2015. "Application of Bounding Surface Plasticity Concept for Clay-Fouled Ballast under Drained Loading." *Computers and Geotechnics* 70: 96–105.

Venkatarama Reddy, B. V., and P. Prasanna Kumar. 2010. "Embodied Energy in Cement Stabilised Rammed Earth Walls." *Energy and Buildings* 42(3): 380–85.

Venkatarama-Reddy, B V, and K S Jagadish. 1993. "The Static Compaction of Soils." *Geotechnique* 43(2).

Vermeer, Pieter A, and R De Borst. 1984. "Non-Associated Plasticity for Soils, Concrete and Rock." *HERON, 29 (3), 1984*.

Villar, María Victoria. 2004. "Thermo-Hydro-Mechanical Characteristics and Processes in the Clay Barrier of a High Level Radioactive Waste Reposi Tory. State of the Art Report." *Informes Tecnicos Ciemat* 1044.

Walker, P, and T Stace. 1997. "Properties of Some Cement Stabilised Compressed Earth Blocks and Mortars." *Materials and Structures/Materiaux et Constructions* 30(203): 545–51. http://www.scopus.com/inward/record.url?eid=2-s2.0-0031277379&partnerID=40&md5=3f44d4e43881c020ca9cc35d2c5498c3.

Walker, Peter, Rowland Keable, Joe Martin, and Vasilios Maniatidis. 2005. "Rammed Earth: Design and Construction Guidelines."

Wong, H, M Morvan, and D Branque. 2010. "A 13-Parameter Model for Unsaturated Soil Based on Bounding Surface Plasticity." *Journal of Rock Mechanics and Geotechnical Engineering* 2(2): 135–42.

Xu, Longfei et al. 2017. "Hydro-Mechanical Triaxial Behaviour of Compacted Earth at

Different Temperatures." In *Poromechanics VI*, , 164–71.

Xu, Yongfu et al. 2014. "Role of Osmotic Suction in Volume Change of Clays in Salt Solution." *Applied Clay Science* 101: 354–61.

Yang, Hong, Harianto Rahardjo, Eng-Choon Leong, and Delwyn G Fredlund. 2004. "Factors Affecting Drying and Wetting Soil-Water Characteristic Curves of Sandy Soils." *Canadian Geotechnical Journal* 41(5): 908–20.

Yu, H S, and C D Khong. 2003. "Bounding Surface Formulation of a Unified Critical State Model for Clay and Sand." In *3rd International Symposium on Deformation Characteristics of Geomaterials*, , 1111–18.

Yu, Hai-Sui. 2007. 13 *Plasticity and Geotechnics*. Springer Science & Business Media.

Zhang, Fan, Yun Jia, H B Bian, and Gilles Duveau. 2013. "Modeling the Influence of Water Content on the Mechanical Behavior of Callovo–Oxfordian Argillite." *Physics and Chemistry of the Earth, Parts A/B/C* 65: 79–89.

Zhang, Feng, and Tomoyuki Ikariya. 2011. "A New Model for Unsaturated Soil Using Skeleton Stress and Degree of Saturation as State Variables." *Soils and Foundations* 51(1): 67–81.

Zhang, Wohua, and Yuanqiang Cai. 2010. *Continuum Damage Mechanics and Numerical Applications*. Springer Science & Business Media.

Zhou, Annan, Ruiqiu Huang, and Daichao Sheng. 2016. "Capillary Water Retention Curve and Shear Strength of Unsaturated Soils." *Canadian Geotechnical Journal* 53(6): 974–87.

Zhou, Annan, Shengshen Wu, Jie Li, and Daichao Sheng. 2018. "Including Degree of Capillary Saturation into Constitutive Modelling of Unsaturated Soils." *Computers and Geotechnics* 95: 82–98.

Zhu, X, J Liu, L Yang, and R Hu. 2014. "Energy Performance of a New Yaodong Dwelling, in the Loess Plateau of China." *Energy and Buildings* 70: 159–66. http://www.scopus.com/inward/record.url?eid=2-s2.0-84890812017&partnerID=40&md5=1afdf548d977255d7477fad577df2ac6.